IMPACT

A new ground-based imaging DOAS instrument: Development, participation at the CINDI-2 campaign and first data analysis

Masterthesis

University of Bremen
Department 01: Physics and Electrical Engineering
Institute of Environmental Physics (IUP)

Submitted from: Mareike Ostendorf
Matriculation number: 2724801
E-mail: ‹mareike.ostendorf@uni-bremen.de›

Submitted on: 29. May 2017

Supervising tutors: Dr. Anja Schönhardt
Dr. Enno Peters

Referees: 1. Prof. Dr. Mihalis Vrekoussis
2. Prof. Dr. John P. Burrows

Erklärungen

Name	Matrikel-Nummer

Urheberrechtliche Erklärung

Erklärung gem. §10 (10) Allgemeiner Teil der MPO vom 27.10.2010
Hiermit versichere ich, dass ich meine Masterarbeit ohne fremde Hilfe angefertigt habe, und dass ich keine anderen als die angegebenen Quellen und Hilfsmittel benutzt habe. Alle Stellen, die wörtlich oder sinngemäß aus Veröffentlichungen entnommen sind, habe ich unter Angabe der Quellen als solche kenntlich gemacht. Die Masterarbeit darf nach Abgabe nicht mehr verändert werden.

Datum	Unterschrift

Erklärung zur Veröffentlichung von Abschlussarbeiten

Bitte auswählen und ankreuzen:

- ☐ Ich bin damit einverstanden, dass meine Abschlussarbeit im Universitätsarchiv für wissenschaftliche Zwecke von Dritten eingesehen werden darf.
- ☐ Ich bin damit einverstanden, dass meine Abschlussarbeit nach 30 Jahren (gem. §7 Abs.2 BremArchivG) im Universitätsarchiv für wissenschaftliche Zwecke von Dritten eingesehen werden darf.
- ☐ Ich bin nicht damit einverstanden, dass meine Abschlussarbeit im Universitätsarchiv für wissenschaftliche Zwecke von Dritten eingesehen werden darf.

Datum	Unterschrift

Acknowledgement

When I went to Anja Schönhardt and Enno Peters to ask for a topic for my master thesis, I didn't expect this outcome. So thank you and Mihalis Vrekoussis for giving me this opportunity of a set-up of a new instrument and participation in a campaign including the following analysis.

For being the second referee I want to thank John Burrows. Thanks goes also to Andreas Richter for providing fast changes of software to the special needs of the instrument.

Furthermore I want to thank the rest of the DOAS and LAMOS work-group for their support. This included help in the laboratory as well as tips regarding the analysis and programming. The ones, which helped with set-up and care of the instrument during the CINDI-2 campaign I want to name: André Seyler, Andreas Richter, Enno Peters, Folkard Wittrock, Mihalis Vrekoussis, Stefan Schreier and Tim Bösch. Of course special thanks goes to the organizers and participants of the CINDI-2 campaign, making it a very successful campaign.

The support of family and friends helped me a lot to finish this thesis without too much distress, so thank you.

Contents

List of Figures

List of Tables

1. Introduction and motivation

Scientists are full of curiosity and want to gain more knowledge. Atmospheric scientists for example investigate the atmosphere (including weather phenomena), air quality (and its impact), create models to describe the earth climate system and much more. In order to extent our knowledge about the nature, measurements are of great importance.
In 1785 ozone (O_3) was measured for the first time and identified and named 54 years later. It was thereby one of the first atmospheric trace gases being investigated [23]. Since this, numerous measurement techniques evolved. One of it is the passive optical absorption spectroscopy, which can be applied to various forms of measurement instrumentation: satellites [25], airplanes [28] and ground-based instruments [21].
In terms of ground-based differential optical absorption spectroscopy (DOAS), MAX-DOAS (multi axis) instruments were developed to investigate tropospheric trace gases (e.g. nitrogen dioxide, NO_2). The sources of NO_2 are mostly anthropogenic releases (traffic, industry) and it plays a crucial role in the tropospheric chemistry. It effects the oxidation capacity of the atmosphere and is partly responsible for the formation of ozone (summer smog, resp. Los Angeles smog). In addition it contributes to acid rain (see Chapter 2).
However, current MAX-DOAS instruments have some limitations. Even though modern 2D instruments are able to point in any direction, only one measurement in one direction per time can be achieved. Therefore the retrieval of a vertical profile takes time and a complete hemispheric scan is not feasible as it is too time-consuming for the highly varying NO_2.
This leads to the development of a new instrument having imaging abilities fulfilling the following objectives:

- Full hemispheric scan (0° - 360°) with a large vertical field of view (ca. 50°) allowing a profile inversion around the measurement site.
- Use of a fibre bundle (similar to MAX-DOAS) for robustness/flexibility (separate in- and outdoor parts) and overcoming polarization issues.

The main objectives of this thesis are:

- Set-up and characterisation of the IMPACT instrument (novel Imaging MaPper for Atmospheric observaTions) in the laboratory.
- Adjustment of the optical components (in the laboratory as well as in the field).
- Participation at the CINDI-2 campaign in Cabauw, the Netherlands.
  The campaign is the successor of the first CINDI (Cabauw Intercomparison campaign for Nitrogen Dioxide Measuring Instruments) campaign.
  Due to little previously possible test measurements, some improvements were done on site in the beginning of the campaign. Then IMPACT took part in the official intercomparison of slant columns (SCs) of NO_2 and tetraoxygen (O_4).
- Analysis of the results from the campaign.
  A detailed comparison of SC NO_2 of IMPACT with the Bremen MAX-DOAS instrument was done.
  In order to take advantage of the imaging properties, full hemispheric scans were performed in Cabauw, which were investigated for variability of NO_2, especially in the lower elevation angles.

The outline of this thesis is as follows: First, the vertical structure and composition of the Earth's atmosphere with focus on nitrogen oxides is introduced in Section 2. Section 3 describes the solar radiation and the important atmospheric interaction (absorption and scattering) and Section 4 introduces the differential optical absorption spectroscopy (DOAS) technique. Section 5 focuses on the experimental set-up of the instrument. The adjustment of the optical components are explained in Section 6, while Section 7 describes the overall characterisation of the instrument. The instrument's performance during CINDI-2 including its imaging characteristics are the topic of Section 8. Section 9 then presents the results including the comparison with the Bremen MAX-DOAS and the hemispheric scans. Finally, Section 10 summarizes the results and gives an outlook for future tasks and activities.

2. Earth's atmosphere

The first theoretical section describes the Earth's atmosphere with its vertical structure and the chemical composition at ground level. As the new imaging DOAS instrument IMPACT measures nitrogen dioxide (NO_2), the nitrogen oxides in the troposphere are focused on.

2.1. Vertical structure

The Earth atmosphere is a thin gaseous envelope and can be parted in layers (bottom to top): troposphere, tropopause, stratosphere, stratopause, mesosphere, mesopause and thermosphere. Characteristic for each layer is its temperature gradient.

As IMPACT is a ground-based passive instrument, the measured sunlight needs to pass all layers. The troposphere is the most important in this case, because 85%-90% of the total mass of all gases in the atmosphere is located in the troposphere. Within this layer fast vertical transport phenomena of energy and mass occur.

Another important layer for the passive measurement method is the stratosphere, which starts at roughly 10-20 km altitude depending on latitude. 90% of the atmospheric ozone is located here. This ozone layer causes absorption of UV-light and is therefore critical for life on Earth [6].

2.2. Chemical composition in the troposphere

The atmosphere consists of many different gases. Permanent gases (i.e. chemically inert) in the troposphere are nitrogen (78%), oxygen (21%) and water vapour (1-3%). Trace gases are of special importance although their abundance is comparably small and can vary strongly in time and space. Many trace gases are radicals and therefore very reactive, leading to relatively short lifetimes (few seconds to years). With their high reactivity and the resulting various reactions, the trace gases greatly influence the composition of the atmosphere [26]. Some trace gases have even a direct influence on humans and animals, e.g. air pollutants [13].

The composition of the atmosphere is illustrated in Figure 2.1. The plot highlights the small percentage trace gases contribute to the entire atmosphere. The NO_X which is of interest for the following measurements has a mixing ratios of only 100ppt (parts per trillion) in the clean troposphere [5].

Due to the strong spatial variation, the concentration of NO_2 is strongly depended on the region. Therefore the concentrations differ for urban and rural areas.

For cities like Bremen the concentration is around 20-25 $\mu g/m^3$ as annual mean. Since 2010, an EU directive fixes the annual limit value to 40 $\mu g/m^3$ [11]. This value limit is sometimes exceeded: e.g. in Berlin for some of the main streets [30].

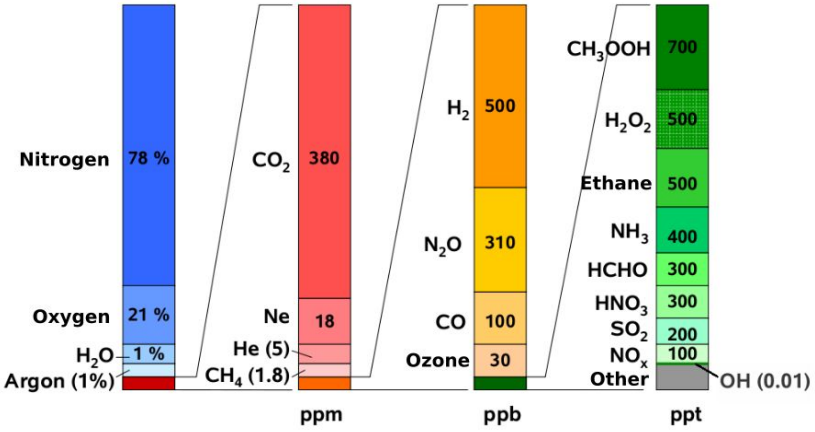

Figure 2.1: Composition of the atmosphere in the troposphere) [5].

2.3. Nitrogen oxides in the troposphere

The nitrogen oxides like nitrous oxide N_2O, nitrogen dioxide NO_2, nitric oxide NO, nitric acid HNO_3 as well as ammonia NH_3 are chemically reactive and important for environmental problems.

Some of these problems are i.e. the development of acid rain (HNO_3), photochemical smog (NO_X) and tropospheric aerosols and also the destruction of the stratospheric ozone layer (N_2O).

The active nitrogen oxides NO_X are nitric oxide NO and nitrogen dioxide NO_2. These molecules are in a dynamical equilibrium and convert rapidly into each other. Therefore it is common to merge both into the group of active nitrogen oxides NO_X [6]:

$$NO + NO_2 \equiv NO_X \tag{1}$$

The active nitrogen oxides are mostly contributing indirectly to environmental problems due to their large reactivity in the tropospheric chemistry. In the troposphere they

act as a catalyst for the production of ozone and determine the concentration of the hydroxyl radical OH. This radical is the most important oxidising agent in the troposphere and has a large impact on the concentration of many gases, which in turn absorb (infra-red) radiation. Thereby active nitrogen oxides have a large indirect influence on the equilibrium of the radiation budget [18].

Sources

Sources are mostly anthropogenic and have increased since the industrial revolution.

Active nitrogen oxides are mainly emitted as NO. The main sources are listed in figure 2.2. Anthropogenic sources as burning of fossil fuels (e.g. by power plants and transportation sector) are the biggest emitters. While planes have a small part in the overall emissions, they are primarily responsible for emissions in the free atmosphere at around 10 km. NO_x emitted at the ground level is mostly converted before reaching this height due to their short lifetime and reactivity.

Natural sources such as microbial activities are responsible for soil emission of NO_X. Lighting is probably the most important natural source in the free troposphere. However, these emissions can not be quantified (so far) without a large error. The values in the figure are estimated.

Anthropogenic sources show errors around ±30%. Natural sources (except lightning) have an uncertainty of a factor of 2 [18].

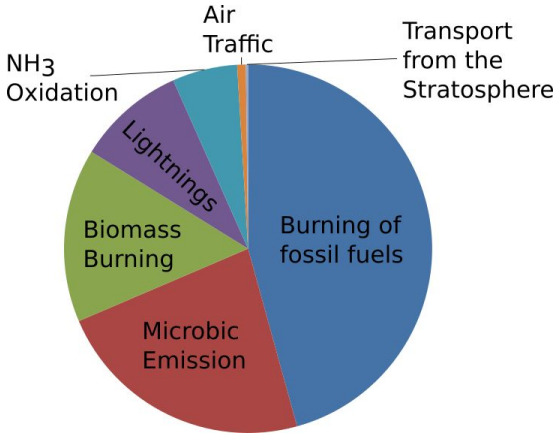

Figure 2.2: Main sources of NO_X in the atmosphere (used values from [18]).

The emitted NO is converted to NO_2 by reaction with ozone. This NO_2 is then photolysed to NO during daytime. The oxygen molecule and the oxygen radical are then reacting to an ozone molecule, resulting in a null cycle [6]:

$$\begin{array}{lllllllll} NO & + & O_3 & & & \longrightarrow & NO_2 & + & O_2 \\ NO_2 & + & h\nu & & & \longrightarrow & NO & + & O \\ O & + & O_2 & + & M & \longrightarrow & O_3 & + & M \end{array}$$

Sinks

The sinks are mostly chemical reactions in the lower atmosphere. Especially the atmospheric oxidation is of importance [18]:

1. During the day: nitrogen dioxide to nitric acid by the hydroxyl radical and a collision target M

$$NO_2 + OH + M \longrightarrow HNO_3 + M$$

2. At night: nitrogen oxide to nitrate by reaction with ozone and also nitrogen dioxide to dinitrogen pentoxide by using nitrate

$$\begin{array}{lllllllll} NO & + & O_3 & & & \longrightarrow & NO_3 & + & O_2 \\ NO_2 & + & NO_3 & + & M & \longrightarrow & N_2O_5 & + & M \end{array}$$

Nitrate and dinitrogen pentoxide N_2O_5 are removed out of the atmosphere by wet deposition.

One additional but weaker sink is the dry deposition of nitrogen dioxide. Part of the NO_X recurs due to photo-dissociation with nitric acid HNO_3 or nitrate NO_3 [32].

3. Radiation

For passive ground-based differential optical absorption spectroscopy (DOAS), the sun is the light source. The radiation emitted by the sun is altered by several atmospheric interactions (absorption and scattering). Absorption by trace gases are exploited by the DOAS-method (explained in Section 4.1).

3.1. Solar spectrum

The sun can be approximated as a black body. The radiation though, which is measured at the ground level, shows differences to a black body radiation according to Planck's law. Figure 3.1 shows the spectrum of a black body, the solar spectra measured at the top of the atmosphere and at ground level. One clear difference from a theoretic black body to the real sun are the outer layers of the sun, which absorb part of the radiation emitted in the inner regions resulting in the so called Fraunhofer lines.

The difference between the spectra before and after passing the Earth's atmosphere is large. A large fraction of the radiation does not reach the ground, due to absorption by molecules (e.g. H_2O, O_3) and scattering effects on particles and molecules within the earth's atmosphere. These effects are briefly explained in the next sections [26].

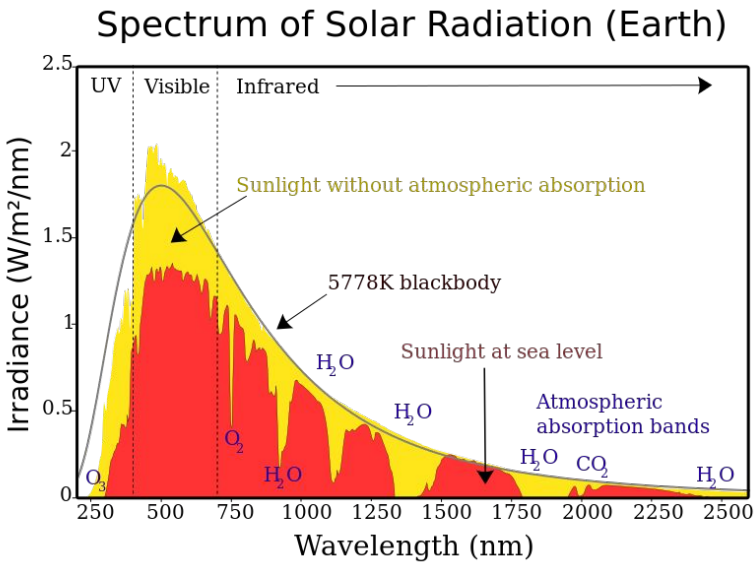

Figure 3.1: Radiation spectra of the sun at top of atmosphere and at ground level and the approximated black body radiation spectrum [33].

3.2. Absorption

In general, photons corresponding to molecular transitions (electric, vibrational, rotaional), i.e. fullfilling $\Delta E = h\nu$, can be absorbed by molecules, which are then excited. As this depends on the inner-molecular structure, every molecule has its own characteristic absorption spectra [26].

Figure 3.2 shows an example absorption spectrum of NO_2 in the wavelength region from 425-490 nm, which is used in the retrieval. The strong absorption bands, clearly visible in the figure, are characteristic for NO_2 and can be distinguished from the absorptions by other trace gases.

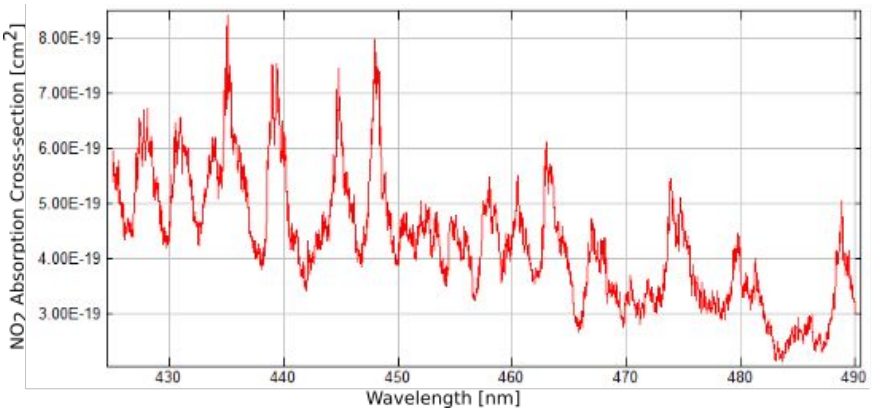

Figure 3.2: Absorption cross-section of nitrogen dioxide (NO_2) [1].

3.3. Scattering effects

Important scattering effects occur at air molecules and aerosols. Scattering can either be elastic or inelastic. Elastic scattering is described by Rayleigh or Mie-scattering. The so called Ring effect is an inelastic scattering effect [24].

Rayleigh- and Mie-scattering

In contrast to absorption processes, Rayleigh and Mie scattering show no strong molecule or wavelength dependence resulting in a continuous spectrum. The scattering effects can be described with following equations:

$$\sigma_{Ray}(\lambda) \sim \lambda^{-4} \tag{2}$$

$$\sigma_{Mie}(\lambda) \sim \lambda^{-\alpha} \tag{3}$$

α is the so called Ångstrøm-exponent. Its value varies typically between 0.5 to 2.5 and is inversely related to the mean aerosol particle radius [23].

The spectral dependence of both effects can be described through polynomials in the DOAS-equation (see Section 4.1).

Crucial for Rayleigh and Mie-scattering is the ratio of wavelength to particle size [26]:

- If the particle is small compared to the wavelength, then Rayleigh-scattering is dominant. For visible light this is true for air molecules as well as for small aerosol particles with a linear dimension smaller than 0.1 μm.
- If the particle is not small compared to the wavelength, then Mie-scattering is dominant. Examples for this case are larger aerosol particles with a size $> 0.1\mu$m, mist as well as cloud and fog particles.
- If the particle is even larger, e.g. rain drops, then geometric scattering is dominant. One visible example of geometric scattering is the formation of rainbows.

Ring effect

The Ring effect is an apparent filling-in of Fraunhofer lines by travelling through the earth's atmosphere and can be explained by inelastic scattering on air molecules. The inelastic scattered photons change their energy and therefore their wavelength. In the atmosphere, most inelastic scattering is by rotational Raman scattering. With the resulting strong wavelength dependence, the ring effect is considered as a type of absorber with an absorption spectrum $\sigma_{Ring}(\lambda)$ in the DOAS-method [24].

4. Differential Optical Absorption Spectroscopy (DOAS)

The Differential Optical Absorption Spectroscopy (DOAS) is a remote sensing technique for atmospheric trace gases. The method can be applied to measurements of light in the UV, visible, and NIR spectral range of i.e. satellite measurements as well as ground-based instruments [23]. The basic principle (absorption spectroscopy) and its modifications for DOAS will be explained in the following sections.

4.1. DOAS method

The main equation used by the DOAS-method is Lambert-Beer's law. This describes the effect of attenuation of intensity through a medium:

$$I(\lambda) = I_0(\lambda) \cdot \exp(-\sigma(\lambda) \cdot \rho \cdot s) \tag{4}$$

Figure 4.1 illustrates the attenuation of light and the resulting exponential function of the Lambert-Beer law [23].

$I_0(\lambda)$ is the incident radiation, which is attenuated by travelling through a homogeneous absorbing medium with concentration ρ after a path length of s. $\sigma(\lambda)$ is the absorption cross-section of the medium and $I(\lambda)$ is the resulting spectrum.

The ratio $D = \ln\left(\frac{I_0(\lambda)}{I(\lambda)}\right)$ is called optical thickness.

In this simplified case, the concentrations can be calculated with knowledge of the absorption spectra.

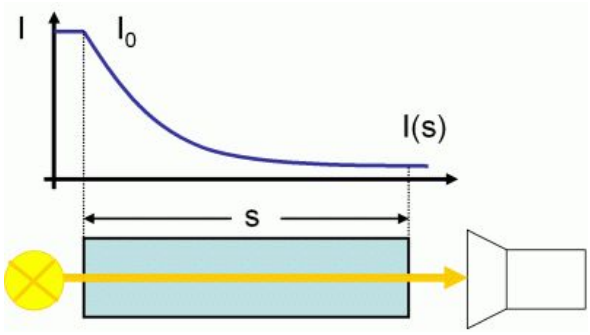

Figure 4.1: Principle of the Lambert-Beer law [17].

For the measurements the equation needs to be adapted. Instead of only one absorber, various absorbers can be present (sum in equation 5). Mie and Rayleigh scattering as well as the Ring effect are taken into account by applying a pseudo cross-section.

As absorber concentrations etc. depend on temperature and thus on altitude, these quantities are no longer constant (as in equation 4), and therefore integrated along the light path.

Finally this leads to following equation:

$$I(\lambda) = I_0(\lambda) \exp\left\{ - \int \Big[\Sigma_j \rho_j(s) \sigma_j(\lambda, s) + \rho_{\mathrm{Ray}}(s) \sigma_{\mathrm{Ray}}(\lambda, s) + \rho_{\mathrm{Mie}}(s) \sigma_{\mathrm{Mie}}(\lambda, s) + \rho_{\mathrm{Ring}}(s) \sigma_{\mathrm{Ring}}(\lambda, s) \Big] ds \right\} \tag{5}$$

As a good approximation the cross-section dependence on s can be neglected. The integral is then only over the concentrations leading to the finally desired quantity, the so-called slant column $\mathrm{SC}_j = \int \rho_j(s) ds$.

$$I(\lambda) = I_0(\lambda) \left\{ -\Sigma_j \sigma_j(\lambda) \mathrm{SC}_j - \rho_{\mathrm{Ray}}(s) \mathrm{SC}_{\mathrm{Ray}}(\lambda, s) - \rho_{\mathrm{Mie}}(s) \mathrm{SC}_{\mathrm{Mie}}(\lambda, s) \right\} \tag{6}$$

Now the simplification of the DOAS-method can be applied. It splits the cross-section of the trace gas j in narrowband structures $\sigma'_j(\lambda)$ and broadband structures $\sigma_{j0}(\lambda)$:

$$\sigma_j(\lambda) = \sigma_{j0}(\lambda) + \sigma'_j(\lambda) \tag{7}$$

By splitting the spectra and taking advantage of the fact, that aerosols, turbulences and instrumental effects as well as scattering show very broad and smooth spectra, the DOAS-method can very well separate between quantities of interest (trace gases) and approximate all other effects by a polynomial [23].

As a result, the differential simplification leads to the DOAS equation:

$$\ln\left(\frac{I_0(\lambda)}{I(\lambda)}\right) = \Sigma_j \sigma'_j(\lambda) \mathrm{SC}_j - \Sigma_p a_p \lambda^p \tag{8}$$

In this equation, the left-hand side consists of measurements only, and with known cross-sections σ'_j the right-hand side is fitted (linear least square fit) yielding the slant columns SC_j as well as polynomial coefficients a_p [24].

4.2. Measurement geometry

IMPACT is a passive ground-based imaging DOAS-instrument based on measurements of scattered light. It works similar to the Bremen MAX-DOAS instruments. In Figure 4.2 the measurement geometry of a MAX-DOAS instrument is illustrated.

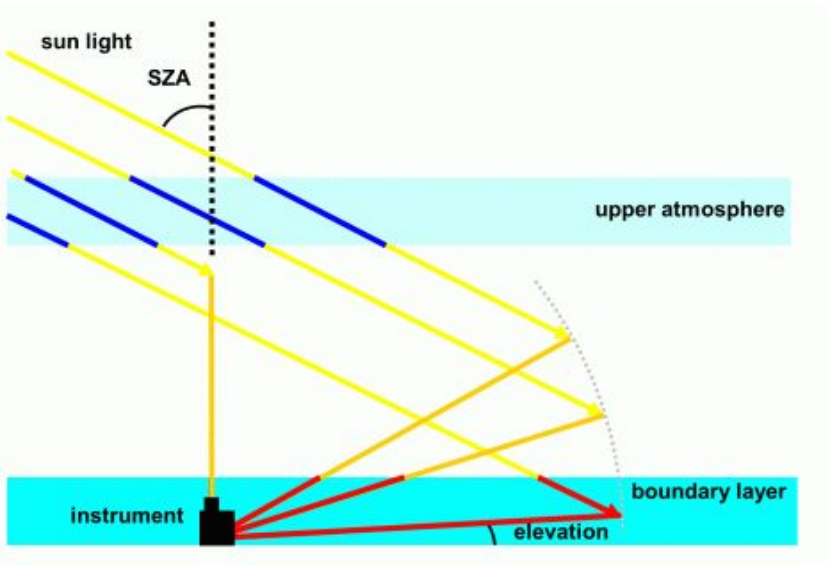

Figure 4.2: Measurement geometry for MAX-DOAS instruments [17].

The light measured by the ground-based instrument travels through the atmosphere. The angle of the incident radiation into the atmosphere is determined by the Solar Zenith Angle (SZA), which is the angle between sun and zenith. The elevation angle describes the angle of the viewing direction above the horizon and determines the measured light path in the lowest atmosphere layer.

For different elevation angles, the light path through the upper atmosphere stays almost constant. The light path trough the boundary layer on the other hand changes a bit: with lower elevation angles, the light path increases. However the length of light path in the boundary layer does not only depend on the viewing geometry. For measurements of scattered light, the mean free path of the photon is an important quantity. The scattering point is illustrated as the grey dotted line in figure 4.2.

As explained in Section 4.1, the concentration of an absorber integrated along the light path is called the slant column. However, as the slant column depends on the light path it also depends on the viewing geometry.

With so called Air Mass Factors (AMF) it is possible to convert the slant columns to the light-path-independent quantity Vertical Column (VC). AMF's are calculated with

radiative transfer models taking into account all scattering and absorption processes in the atmosphere. However this is behind the scope of this thesis and foreseen for a later stage of data analysis.

The disadvantage of MAX-DOAS instruments is that it measures only one elevation angle at a time Therefore scanning the atmosphere in vertical direction takes a lot of time [17].

This limitation is addressed by the IMPACT instrument that can measure 50 elevation angles at the same time. In comparison to the Bremen MAX-DOAS instruments necessary prerequisites are: 1) an especially designed imaging spectrometer and 2) a sorted lightfibre (see Section 5).

4.3. Data analysis

The following programs were used to calculate the slant columns out of the spectra obtained by the measurement software AMAX_OMA:

- NPREPARE
  Sorting of data and calibration by calling either FKALIB or NKALIB
- FKALIB/NKALIB
  Calibration of wavelengths by Fraunhofer-lines (FKALIB)
  or Hg-Cd-lines (NKALIB)
- RESOLUT
  Calculation of the instrument response function
- NLIN_D
  Calculation of the slant columns and residuals using the DOAS equation (equation 8)

For graphical purposes the following programs were used:

- WINSPEC
  Plotting retrieved spectra and images
- SHOW_FIT
  Plotting retrieved slant columns
- MULTSPEC
  Plotting residuals

Figure 4.3 illustrates how the progress from raw data to slant columns usually takes place. The blue boxes are programs used and the black boxes show the used or retrieved data.

AMAX_OMA is the measurement program operating the instrument and taking spectra (raw spectra, dark spectra and calibration lamp line spectra are measured as intensity for each pixel). These spectra are then post-processed with NPREPARE, which subtracts the dark spectra and performs the wavelength calibration by calling one of the subroutines FKALIB or NKALIB.

RESOLUT calculates the instrument response function for every viewing direction (using the Hg-Cd line lamp measurements). These are crucial to convolve the high resolution reference cross-sections to the resolution of the instrument.

The convolution is done by NLIN_D. With the convolved cross-sections the slant columns of the trace gases of interest and the residual are retrieved.

The results are then visually inspected with WINSPEC, SHOW_FIT and MULTSPEC [27].

As this is a new instrument, it first needed to be properly adjusted (see Section 6). Afterwards a first characterisation was done. The characterisation is presented in Section 7.

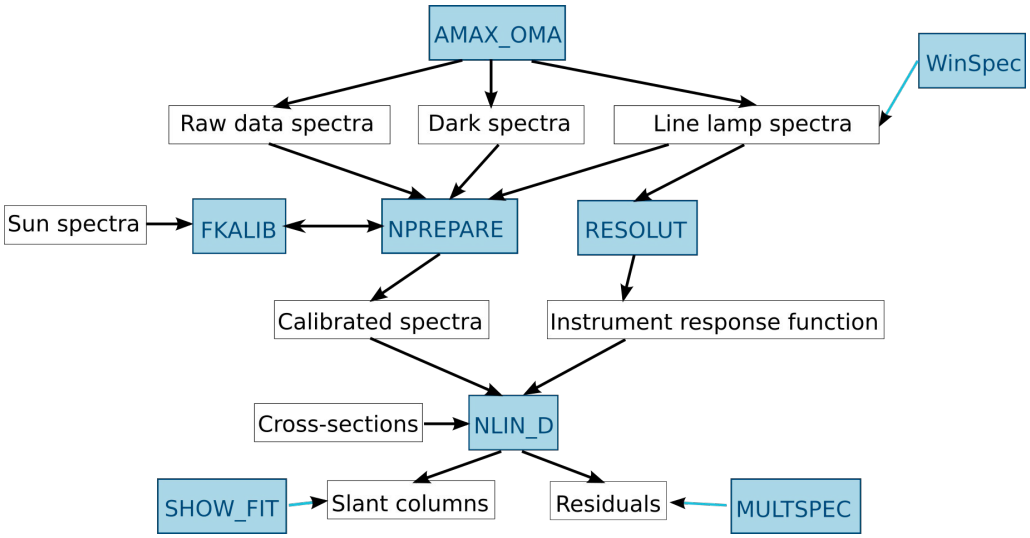

Figure 4.3: Progress from raw data to slant columns [27].

5. Experimental set-up

A DOAS-instrument typically consists of four key components [23] :

1. Receiving optics
2. Connective optics
3. Spectrometer - detector system
4. Computer system for measurement software and data analysis

In particular for IMPACT:

1. The receiving optics is an objective inside a telescope mounted on a pan-tilt head.
2. The objective is connected via a sorted quartz fibre bundle with the spectrometer.
3. The spectrometer - CCD (charge-coupled device) combination is included together with other electronics into a rack. This allows the imaging DOAS instrument to be easily packed and transported and it can therefore be a campaign orientated instrument. The disadvantage however is, that it is quite heavy ($\sim$ 80kg).
4. The measurement software is running on a laptop, which is located on top of the rack during operation.

Each component of the imaging instrument is explained in detail in the following subsections.

5.1. Receiving optics - telescope and pan-tilt-head

The telescope is a new design by E. Peters especially developed for the imaging instrument. It is smaller and more compact than the usual Bremen MAX-DOAS telescope. In Figure 5.1, the inside of the telescope is shown.

On the top left rail right in front of the top window the objective is located. The window is a quadratic quartz glass, which enables the instrument to measure light in the UV wavelength region. The quartz glass is fixed by screws, so it can be easily removed and replaced by e.g. a filter. The quartz glass and its mounting are illustrated in Figure 5.2(a). It is important, that the entrance window is sufficiently large to avoid blocking parts of the large ($\sim 50^\circ$ in the vertical) field of view. For the calibration measurements using a Hg-Cd lamp it is necessary to illuminate the whole field of view,

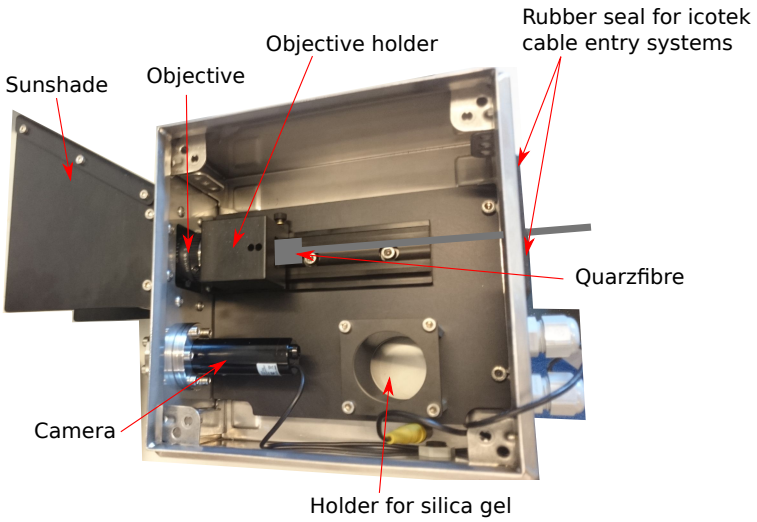

Figure 5.1: Picture of the (open) telescope box.

which wouldn't be possible with an inbuilt lamp. It was therefore decided not to include a Hg-Cd Lamp into the telescope (which is done in the MAX-DOAS telescopes), as it is sufficient to do manual calibration measurements with an external lamp for the campaign based instrument.

The objective holder also connects to the quarzfibre. Because the quarzfibre has to be at the focal point of the objective it is important that the fibre stays in the right position. To avoid having to remove the fibre during installation, a big hole is in the right wall of the telescope to remove the complete objective holder inclusive fixed lightfibre and objective. An icotek cable entry system was used to ensure the waterproofness. In Figure 5.2(b) this system can be seen at top of the telescope. The system consists of two icotek cable entry frames with different cable grommets screwed to each other and onto the telescope from the outside. The inner grommets has a very small tightening zone around the lightfibre to close the gap for waterproofness. The outer cable grommets has a bigger gap where a spring is pushed into. The use of a spring around the quarzfibre is needed for strain relief and bend protection as demonstrated in Figure 5.2(b).

In addition silica gel as a desiccant is used inside the telescope. Silica gel can remove moisture by adsorption onto the surface of its numerous pores.

The last item inside the telescope is the camera on the bottom left corner (Fig. 5.1). This is included in the telescope for scene documentation (e.g. hitting obstacles).

On the outside in front of the objective window a sunshade is attached to protect from direct sun which can cause saturation of the CCD pixels.

In Table 5.1 the specifications of the objective are listed.

(a) Mounting of filter glass at the telescope

(b) Bend protection and strain relief of the light fibre

Figure 5.2: Telescope mounted on the pan-tilt-head.

Objective model	**M0814-MP2**
Mount	C-Mount
Type	2/3 type Megapixel Camera
Focal Length [mm]	8 mm
Max. Aperture Ratio	1:1.4
Operation Range	Iris: F1.4 - F16C Focus: 0.1 m - Inf
Control	Iris: manual Focus: manual
Angle of view	D: 67.1 ° H: 56.3 ° V: 43.7 °
Operating Temperature	-10°C - 50°C

Table 5.1: Specifications of the objective [31].

The telescope is mounted on a pan-tilt-head (Fig. 5.2(a)). The pan-tilt-head (ENEO VPT-501) is a commercial product which is usually used for service of security cameras but has been used for several Bremen MAX-DOAS systems since 2009 [21].

The covered area of the head is $\pm 90°$ in elevation and $\pm 180°$ in azimuthal direction allowing any viewing direction [10].

5.2. Connective optics - quarzfibre

The light collected by the objective is transported via a quarzfibre to the spectrometer. This quarzfibre has 69 NCC (Non Circular Core) fibres which are quadratic with a width of 0.123 mm and an active light area of 0.01 mm^2 [8]. The single fibres are sorted, i. e. they are lined up and on each end of the bundle the fibres have the same position as illustrated in Figure 5.3(a). Therefore the spatial information is preserved.

Two more advantages of using a quarzfibre are:

- Freedom in placement as the receiving optics can be placed outside and the temperature sensitive parts like the spectrometer inside.
- Depolarisation of scattered light which can cause errors/artefacts in the DOAS analysis.

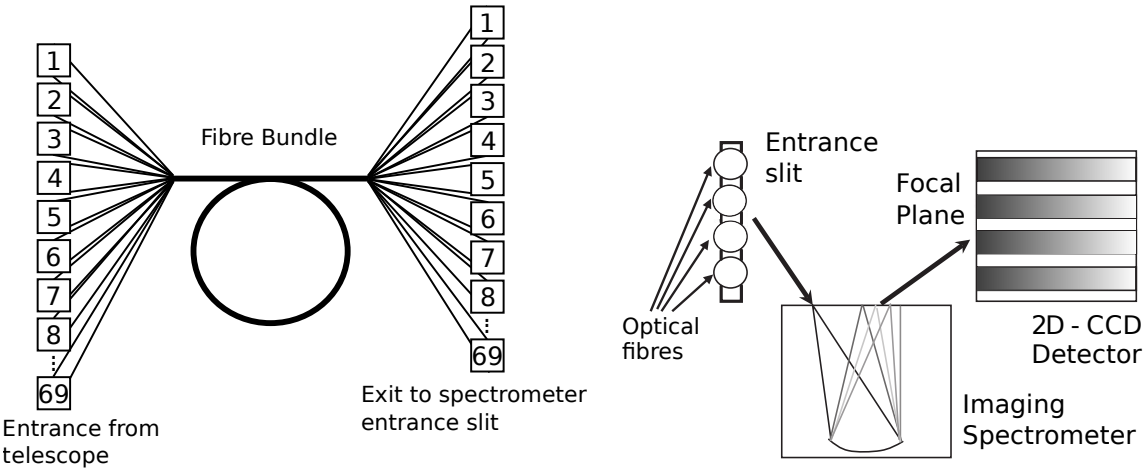

(a) Sketch of the fibre bundle

(b) Principle of imaging spectrometer [23]

Figure 5.3: Preserving of spatial information.

5.3. Rack - spectrometer detector system

In Figure 5.4 the complete rack is shown. It is a 19" QSD-Rack, which allows mounting of 19" cases like the Uninterruptable Power Supply (UPS). On top of it the measurement laptop is located, which runs the measurement software AMAX_ OMA. The laptop is connected via USB to the spectrometer and the CCD inside the rack. Furthermore, it is connected to the ADAM converter, which enables communication between laptop and pan-tilt head. Due to only 4 USB-ports on the laptop, the last one is used for an USB-hub, because at least two more USB-ports are needed: One for the video grabber, which is connected to the video camera installed in the telescope and one for external hard drives for data back-up. Inside the rack on the upper most panel additional electronics are mounted. On the second panel the imaging spectrometer and CCD-detector are located. Under it the temperature controller is located, which should stabilise the spectrometer to a stable temperature. The under most component in the rack is the uninterruptable power supply, which provides stable power in cases of fluctuation of current or power blackout.

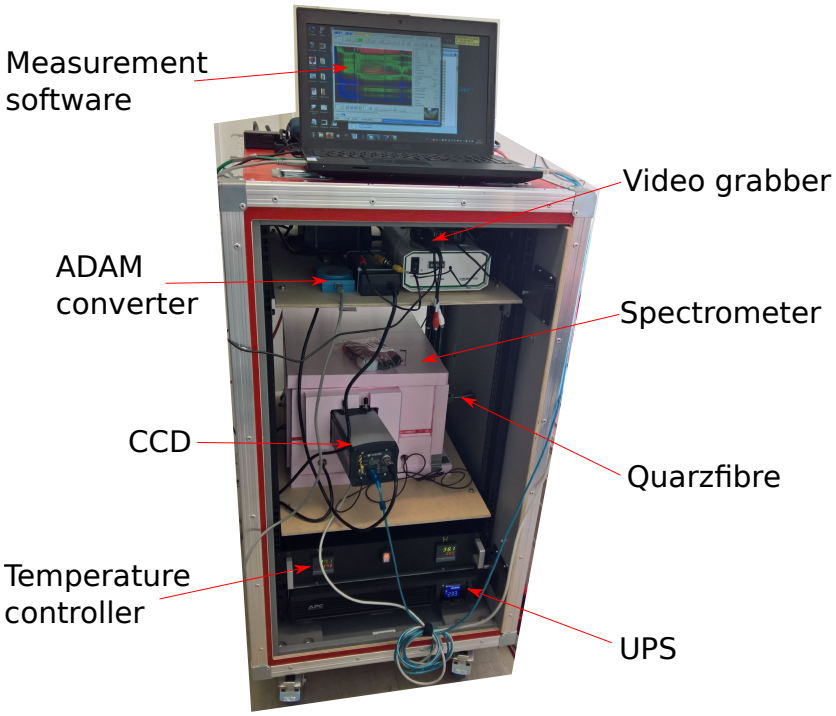

Figure 5.4: Picture of the rack.

5.3.1. Spectrometer

Specifications of the spectrometer

The used spectrometer is an Andor Shamrock SR303i-A and its specifications are listed in Table 5.2. It is built on the design of a Czerny–Turner spectrometer and then set to the needed configuration, which is illustrated in Figure 5.5.

Spectrometer model	**Andor Shamrock SR303i-A**
Focal Length [mm]	303
Aperture	f/4
Wavelength Resolution [nm]	0.1
Wavelength Reproducibility [nm]	0.05
Size [mm]	394 x 238 x 208
Weight [kg]	20
Grating Size	68 x 68
Wavelength Accuracy [nm]	0.04
Wavelength Repeatability [pm]	4

Table 5.2: Spectrometer specifications [3].

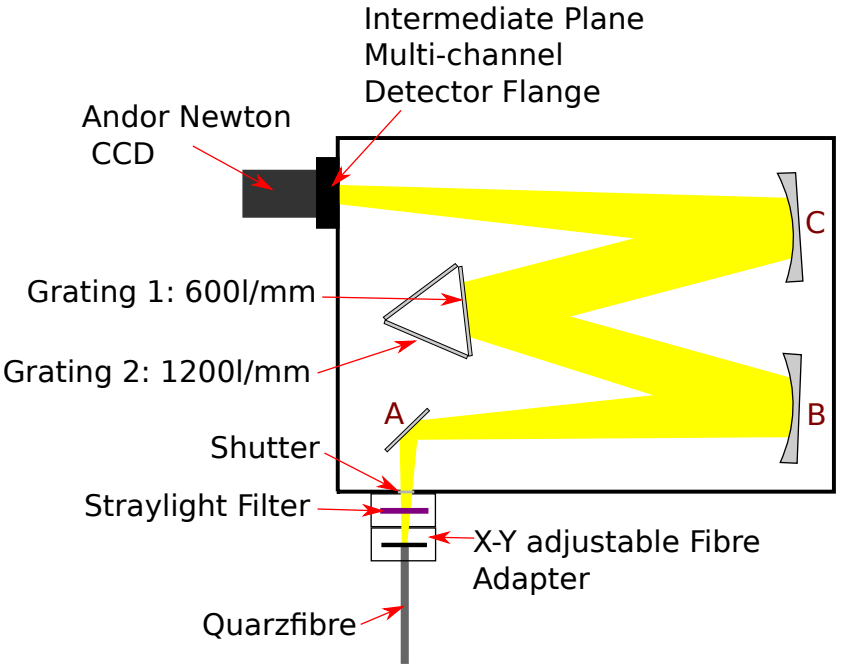

Figure 5.5: Configuration of the adjusted Andor Shamrock SR303i-A spectrometer.

Spectrometer functionality

The lightfibre bundle is connected to the spectrometer entrance (Figure 5.5). As the single NCC fibres have a width of 100 μm they simulate an entrance slit of 100 μm. The first mirror A redirects the beam onto the mirror B which collimates the light onto the diffraction grating. For this the entrance slit (or lightfibre) has to be in the focal plane of the collimating mirror B. The grating is tilted in a way, that the first order of diffraction is identical to the direction of geometric reflectance (blaze angle). The outgoing light is directed onto the focusing mirror C. This mirror focuses the spectrum onto the focal plane of the detector. There are several possibilities to mount the CCD onto the spectrometer: spectroscopy flange, intermediate flange and imaging flange. As indicated by its name, each has a different advantage optimizing either the spectral or the spatial resolution (the intermediate is a compromise).

The different mountings are necessary as the imaging direction is perpendicular to the dispersion direction. In the end the 2D CCD detector records multiple spectra (one per line) which correspond to a point at the entrance of the spectrometer. This means, that in the end each single fibre is mapped onto the focal plane of the CCD chip. This is illustrated in Figure 5.3(b). To be able to preserve the spatial information the spectrometer needs to be specially designed as an imaging spectrometer. The main difference between the imaging spectrometer and a 'normal' spectrometer is the radius of curvature of the mirrors. While the normal spectrometer has mirrors with the same radius of curvature in vertical and horizontal direction, the imaging spectrometer has two different radii. This prevents astigmatism and focuses both spatial and spectral resolution at the same point [19]. As this in only true for the middle of the large CCD detector, the different mountings of the CCD optimize either for the focus of the spectral or the spatial resolution.

In the following paragraphs all parts of the spectrometer and its usage will be described. The CCD and the shutter, as its use is important for the CCD, will be explained in Section 5.3.3.

Grating

The grating has many lines (grooves) which act as coherent sources of light, so that the total reflected light consists of a coherent superposition of the partial contributions from all grooves. This results in constructive and destructive interference. The distance of the grooves d needs to be about the size of the wavelength. Then the light is diffracted in a large range $\Delta r = \frac{\lambda}{d}$ of angles r. Constructive interference occurs, if all partial

waves emitted from different grooves are in phase. When the incident radiation gets to a groove with an angle of α, constructive interference is obtained for the outgoing beam with an angle of β when the path difference Δs between the outgoing beams from adjacent grooves is an integer multiple m of the wavelength λ. m is called diffraction order. By using the geometries illustrated in Figure 5.6(a) this yields to the grating equation [9]:

$$\Delta s = d(\sin(\alpha) - \sin(\beta)) = m\lambda \tag{9}$$

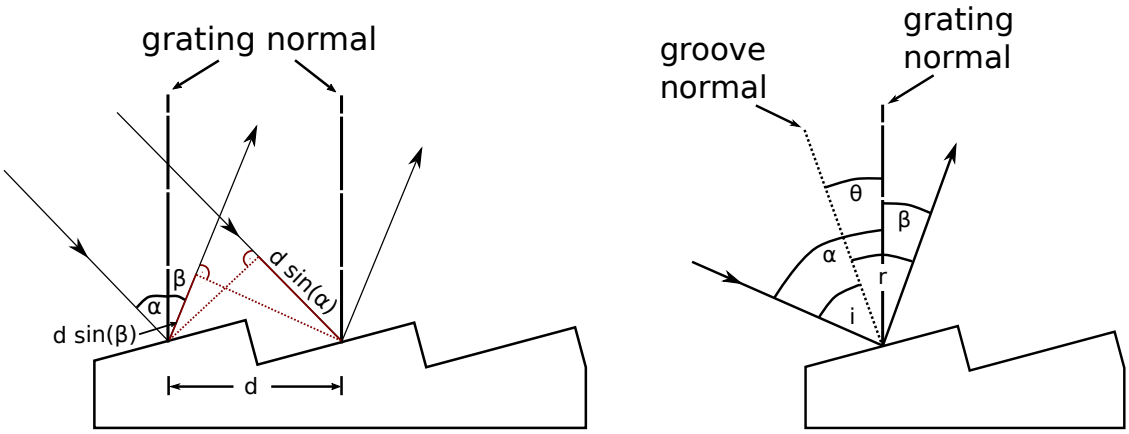

(a) Geometry for constructive interference

(b) Geometry for the blaze angle θ

Figure 5.6: Geometries for the diffraction grating.

The reflectivity of the grating depends on the diffraction angle β and the blaze angle θ which describes the angle between the grooves normal and the grating normal as illustrated in Figure 5.6(b). The reflectivity has its optimum, when the blaze angle is $\theta = \frac{(\alpha-\beta)}{2}$. This can be used to have maximum reflectivity for a special wavelength range [9].

As a conclusion, two properties can be optimised for measurement purposes: number of lines/mm (distance of the grooves d) and blaze angle θ. In the used spectrometer a grating tower holds two gratings, which are listed in Table 5.3. Due to the grating equation the number of lines describes the magnitude of the wavelength splitting, which means that the measurable wavelength range of grating 1 is larger whereby the resolution is better for grating 2. Grating 1 has a range of about 140 nm and grating 2 has a 70 nm range for the used CCD. The blaze angle is equal for both gratings and chosen for optimization of the wavelength range of around 300 nm to optimise the reflectivity for the weaker light from the UV region.

Grating	Grating Code	Number of lines per mm	d [μm]	Blaze angle θ
Grating 1	SR3-GRT-0600-0300	600	~ 1.667	300 nm
Grating 2	SR3-GRT-1200-0300	1200	~ 0.833	300 nm

Table 5.3: Gratings specifications [3].

Entrance slit

The manufacturer built-in entrance slit was removed from the Andor Shamrock spectrometer. This was necessary due to some reflections the entrance slit caused. This can be seen in a measured image of a white lamp shown in Figure 5.7, where on the horizontal axis the spectral information and on the vertical axis the spatial information is plotted. As this could greatly affect the measurement and also can cause early saturation of pixels of the CCD it was decided to remove the slit. This is feasible, because the lightfibre can also act as an entrance slit of 100 μm.

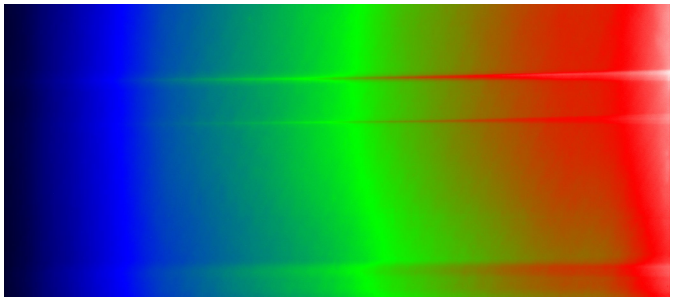

Figure 5.7: Reflections / straylight caused by entrance slit.

Straylight filter

As the sunlight has a large contribution in the visible and Near InfraRed (NIR) part of the spectrum, it is advisable to use a cut-off filter to reduce visible (larger wavlength) and NIR intensities for measurements in the UV or the visible wavelength region near the UV. As this instrumental straylight is of great concern for the DOAS analysis, it is important to reduce it as much as possible [23]. The straylight filter was installed at the spectrometer inside the fibre mounting at the telescope's side. The used filter is a ultraviolett filter HU03 and its transmission curve is plotted in Figure 5.8. The filter has a high transmission of 90 % for the UV wavelength region and a very low transmission for wavelengths from 500 nm to $\sim$ 700 nm. The important wavelength region for visible absorption spectroscopy for NO_2 from 425 nm to 490 nm has a sufficient transmission.

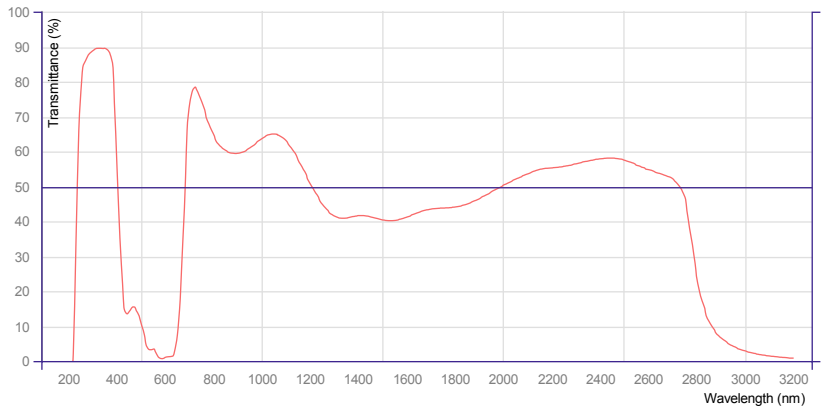

Figure 5.8: Ultraviolett filter for straylight reduction [14].

X-Y adjustable fibre adapter

The X-Y adjustable fibre adapter is used to bring the fibre in the optimal position. First the fibres' end needs to be in the the focal point of the concave mirror. This can be done by hand by moving the fibre inside the X-Y-adjustable fibre adapter. The adjustment procedure is described in Section 6.2.

Furthermore the adapter allows two more degrees of freedom parallel to the entrance in horizontal and vertical direction. This allows to position the fibre directly in front of the entrance.

5.3.2. Temperature controller

In Figure 5.4 it can be seen that the spectrometer is packed into a thermal insulation made out of extruder foam [4]. Inside the thermal insulation box heating foils are attached to the spectrometer: two heating foils on top and two on the bottom, consisting of two separate units. These are controlled by a temperature controller, which is located inside the rack under the spectrometer. One unit controls the temperature at the front of the spectrometer (CCD-side) by turning on the heating foils on top and on the bottom near the CCD. The other unit operates in the same way for the other two heating foils. Two different temperatures were set as desired value. A lower value for the front where the heat is dissipated due to the CCD. The temperature has to be set to a larger value than room temperature as a sufficient gradient is needed for stabilizing the spectrometer, without risking damage by overheating. As a safety measure two thermal cut-out devices were put into the circuit which halt the circuit if a temperature over 60°C is reached.

By using two temperature controllers it should be possible to ensure temperature stability over the whole spectrometer. This is very important, because changes in temperature of the spectrometer cause spectral shifts. Experiences of several DOAS instruments showed that even slight temperature changes cause misalignments of recorded spectra relative to the chosen reference spectrum. This leads to errors in the DOAS analysis (RMS (root mean square) increase).

5.3.3. Charge-Coupled Device (CCD)

Specification of used CCD

The CCD used for this imaging DOAS-instrument is an Andor Newton DU940P-BU. Its characteristics are listed in Table 5.4. It is a full frame back-side-illuminated CCD chip. It is UV enhanced and optimized for 350 nm, similar to the also UV optimized grating inside the spectrometer [2]. With 2048x512 pixels it is bigger than the usual CCD chips used for MAX-DOAS instruments, to have more pixels for the large field of view in the y-axis. The linearity is said to be better than 99% which is very important for the DOAS-analysis, and is therefore verified in chapter 7.1.

CCD model	**Andor Newton DU940P-BU**
Active pixels	2048 x 512
Pixel size [μm]	13.5 x 13.5
Image area [mm]	27.6 x 6.9
Register well depth [electrons]	High Sensitivity mode: 150,000 High Capacity mode: 600,000
Active area pixel well depth [electrons]	100,000
Read noise for 3 Mhz: Typical(Maximum) [electrons]	High Sensitivity mode: 11(15) High Capacity mode: 40 (56)
Sensitivity [electrons /count]	High Sensitivity mode: 1, 2, 4 High Capacity mode: 4, 8, 16
Linearity	Better than 99%
Digitization [Bit]	16
Minimum temperature air-cooled [°C]	-80
Peak Quantum efficiency	$\sim$ 94% at $\sim$ 410 nm

Table 5.4: CCD Specifications [2].

In the following paragraphs first the general functionality of a CCD is described followed by some important characteristics, in addition random errors and noise will be explained.

Functionality of a CCD

The structure of a CCD for capturing images depends on the type of CCD. For the used full frame CCD, no transmission region is needed, so that the CCD only has a photoactive region and a register for readout.

The photoactive region consists of photosensitive semi conductors in a 2 dimensional array. They are metal-oxide-semiconductor (MOS) junctions on a doped silicon substrate (mostly p-doped) and work on basis of the inner photoelectric effect. Incident photons with sufficient energy (> band gap) potentially generate charge carriers by exciting one (or more) electrons from the valence band into the conduction band.

The recombination of the generated electron-hole pair is avoided by an electric field applied (polysilicon electrodes). With the potential the electrodes generates by applying a voltage, the induced electrons concentrate there. They can then be easily shifted from one MOS to the next during the readout process by clocking the electrodes voltage [7].

The array and its readout procedure is shown in Figure 5.9. There are different procedures for readout and only the used one is presented.

When the readout starts, the charge of each row is shifted one step to the top. The upper most pixel row is thereby shifted into the horizontal register. In the horizontal register each pixel is then shifted horizontally and subsequently in an output node. The output node reads the collected charge, which is proportional to the incident light during the exposure time. Finally the recorded charge is digitized and further processed. After each pixel of the first row is read out, the rows are shifted once again vertically and the procedure starts again. This is repeated until all rows are finished.

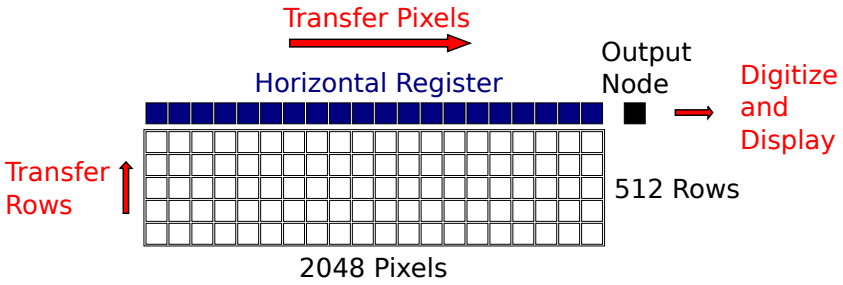

Figure 5.9: Readout of the used CCD.

Full frame CCD

The readout of a CCD takes time, and it needs to be ensured that during the readout no photons are reaching the CCD creating further photo-electrons. This is crucial, as these photoelectrons are induced on the shifted rows and therefore not on the right row. As every row/ every binned region represent a different viewing direction in case of the

imaging instrument, this tampers the result. It is therefore only a problem for imaging instruments, but not for the MAX-DOAS instruments.

There are several set-ups of CCD, which need different approaches to achieve this. The Andor Newton DU940P-BU is a Full-Frame-CCD (FF-CCD), which has the advantage of using the full chip for imaging. For this option the whole CCD chip has to be darkened during the readout. This is done mechanically by placing a shutter at the entrance of the spectrometer. However the mechanical shutter has some disadvantages. As the lifetime of a shutter is stated as 'better than 100.000 cycles' and the shortest used exposuretime is only 0.025 s long, the shutter will fail eventually. However it is possible to compensate the effect of light hitting the CCD during the readout with a so called 'smear correction', so that the shutter is not necessary. This is presented in Section 7.3.

Back-side-illuminated CCD

There are two types of CCDs: either it is a front-side-illuminated or a back-side-illuminated CCD. At a front-side-illuminated CCD chip the incident radiation is coming onto the chip side, where the semi conductors structure (e.g. the electrodes) are located. Even though these are optically transparent, weaker radiation like UV-light can already be absorbed before entering the depletion region and therefore decrease the quantum efficiency. The back-side-illuminated CCD avoids this by rearranging the set-up of the chip and illuminating from the other side, see Figure 5.10. Incident radiation comes directly onto the substrate without passing the electrodes. To be UV enhanced and for 350 nm optimized, the CCD needs to be a back-illuminated CCD [12].

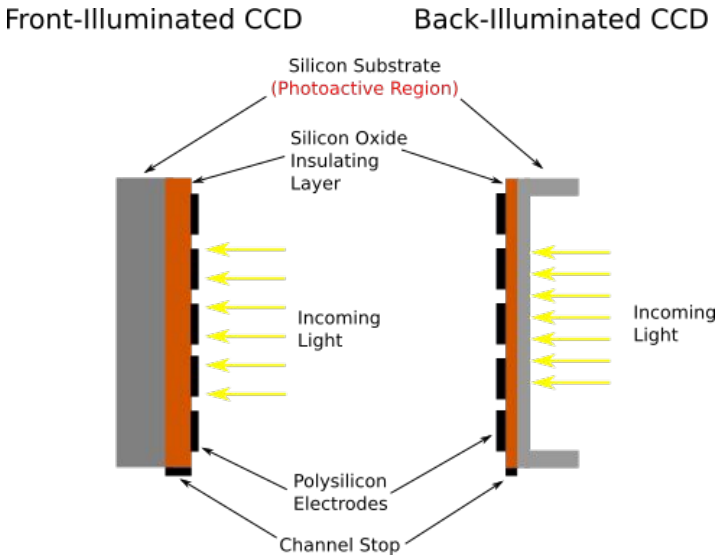

Figure 5.10: Difference between front- and back-illuminated CCD chips.

Random errors and noise

There are several contributions to the overall noise and errors:

- Quantum efficiency
  Probability that an incident photon creates an electron
- Shot noise
  Fluctuations of the number of photons counted
- Dark current
  Signal without any incident radiation
- Charge Transfer Efficiency
  Efficiency loss by shifting the charge
- Readout noise
  Noise produced of the output node
- Blooming
  Errors produced because of overexposure

The quantum efficiency depends on the wavelength of the incident radiation. The used CCD type has a quantum efficiency of over 90% in the used spectral window.

The shot noise occurs due to radiation being quantized and having random statistical fluctuations. Even for an unvarying source the measurements will not have constant photon counts. To minimize the impact of the shot noise a good signal intensity (signal to noise ratio SNR) should be achieved.

The dark signal is temperature-dependent and results from spontaneous generation of free electrons due to heat (thermal excitation). Through inelastic collisions charge carriers can be excited and are recorded as dark current. This is individual for each pixel as there can be pixels more sensitive to heat. A possibility to reduce the dark current is to cool the detector.

Measurements without illumination allow to characterise the standard noise of every measurement consisting of dark current and the read out noise. Then the dark signal can be divided in two parts: a constant offset (the read out noise and an electronic offset) and the thermally induced charge carriers (dark current), which are dependent on the exposuretime. The characterisation is done in Section 7.2.

When a single pixel is saturated due to overexposure, blooming occurs. The blooming effect is when there is more charge generated than the single pixel can store. The charge

will flow to the neighbouring pixels. As this disturbs the measurement greatly it is important to use exposuretimes small enough to avoid this effect. There is a possibility to install an 'anti-blooming gate' into CCDs to avoid blooming by discharging excess charge before the limit is reached. But because this effects the linearity between incident light and charge, it is not an option for DOAS instruments [12][7][23].

5.3.4. Uninterruptable Power Supply (UPS)

The uninterruptable power supply ensures power to all important parts of the instrument when there is a power breakdown or need to move the rack without stopping the measurements. The UPS consist of a 1000VA strong rechargeable battery, which should supply the instrument for around 30 mins. Due to its large weight (20.5 kg) it is located at the bottom of the rack.

6. Adjustment of the imaging DOAS instrument

The adjustment of the imaging DOAS instrument is time consuming, but of great importance as it defines the quality of the results. To achieve the optimal result three steps are necessary:

- Adjustment of CCD mounted on the spectrometer
  Defines spatial and spectral resolution
  Depends on flange used: spectroscopy flange, intermediate flange or imaging flange
- Adjustment of quarzfibre to spectrometer
  Optimizes spectral resolution
- Adjustment of quarzfibre to objective
  Defines field of view

Each of these adjustment procedures is explained in detail in the following sections. Also reasons for using the intermediate flange and things to regard for future adjustments, which can be necessary due to shifts during transport or a complete disassembling of the instrument, are given.

6.1. Adjustment of CCD

For the used CCD, three possibilities to mount the CCD to the spectrometer are available: spectroscopy flange, intermediate flange or an imaging flange.

The spectroscopy flange optimizes the spectral resolution whereas the imaging flange optimises the imaging qualities. The intermediate flange is a compromise.

As the spectral resolution already changes a lot between the spectroscopy and the intermediate flange, the imaging flange turned out to be not recommended as the resulting spectral resolution is not good enough for a DOAS analysis.

Spectral resolution of intermediate and spectroscopy flange
Zenith sky measurements were taken to compare the spectral resolution of both flanges. The measured spectra are shown in Figure 6.1. The spectrum of the intermediate flange is shifted a bit to the right, but the x-axis is pixels (not wavelength). The spectral resolution is much better for the spectroscopy flange. The structure of the spectrum is much more pronounced predominantly at the edge of the CCD and a lot more small absorption effects can be seen. The spectrum of the intermediate flange is much smoother.

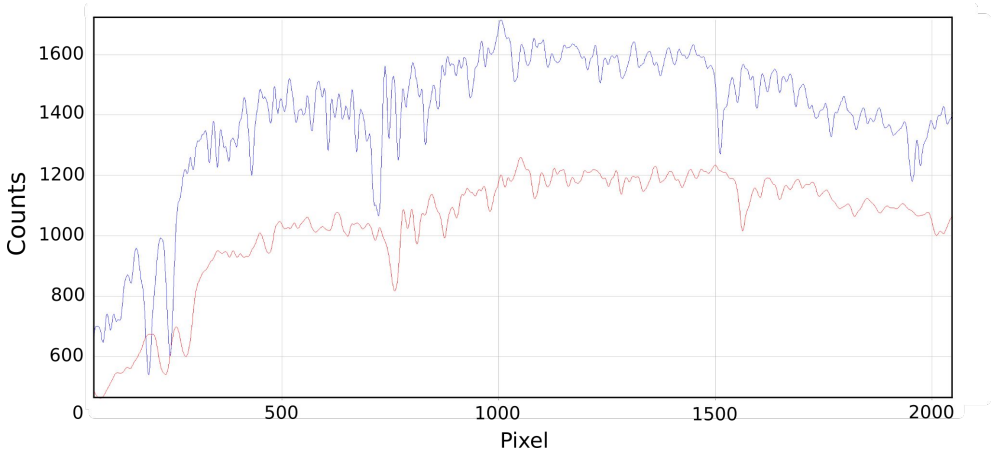

Figure 6.1: Comparison of spectral resolution: spectroscopy (blue) and intermediate (red) flange.

This can be quantified measuring a Hg-Cd calibration lamp spectrum. The spectrum consists of single lines which makes it easy to quantify the spectral resolution of the system at different positions. In theory the spectral peaks would be spectral lines but due e.g. natural broadening and dispersion of the spectrometer the lines appear as gaussians. The peaks can therefore be easily fitted with gaussian curves and then the resulting Full Width Half Maximum (FWHM) of the Gaussian curve is a well comparable value. The resulting FWHM for both flanges and five peaks of the Hg-Cd spectrum (left to right on the CCD) are listed in Table 6.1.

	Intermediate flange		Spectroscopy flange	
	FWHM [pix]	FWHM [nm]	FWHM [pix]	FWHM [nm]
Peak 1	18.3 ± 2.4	1.3 ± 0.2	8.5 ± 0.2	0.60 ± 0.01
Peak 2	15.0 ± 0.9	1.1 ± 0.1	8.7 ± 0.2	0.61 ± 0.01
Peak 3	9.4 ± 0.2	0.66 ± 0.01	9.3 ± 0.3	0.65 ± 0.02
Peak 4	10.0 ± 0.3	0.70 ± 0.02	9.7 ± 0.4	0.68 ± 0.03
Peak 5	17.6 ± 1.3	1.2 ± 0.1	10.8 ± 0.7	0.76 ± 0.05
Mean	14.1 ± 4.2	1.0 ± 0.3	9.4 ± 0.9	0.66 ± 0.06

Table 6.1: FWHM for peaks of the Hg-Cd spectrum for both flanges.

The FWHM values confirm the observation above. The mean FWHM for the intermediate spectrum is 1.5 times bigger than for the spectroscopy flange. However a FWHM of $\sim$ 1 nm is sufficient for a DOAS analysis of NO_2.

As mentioned before, and supported by Table 6.1, the resolution gets worse from the center to the edges of the spectrum. The spectral resolution needs to be optimised to the spectral window used, meaning that the CCD should be aligned in a way, that the fit window of interest is in the center of the chip.

Spatial resolution of intermediate and spectroscopy flange

For the comparison of the spatial resolution a slit is installed horizontally in front of the light fibre, so that only one fibre is illuminated, i.e. one fibre only is mapped onto the CCD. The result for both flanges is shown in Figure 6.2.

Both flanges show broadening along the y-axis. The broadening changes over the CCD and again it is smallest in the middle of the CCD. However in general, the intermediate flange shows much better spatial resolution. The broadening is much more stable along the x-axis, as the mapped fibre broadens a lot more for the spectroscopy flange.

To quantify the spatial resolution in the vertical axis, Gaussian curves were fitted at three different positions inside the fitting window. The resulting FWHM are listed in Figure 6.2. These values confirm the observation. In general the mapped fibre is broader for the spectroscopy flange with a mean value $\sim 35\%$ bigger. The broadening for the intermediate flange is stable with only $\pm$ 3 pixel variance.

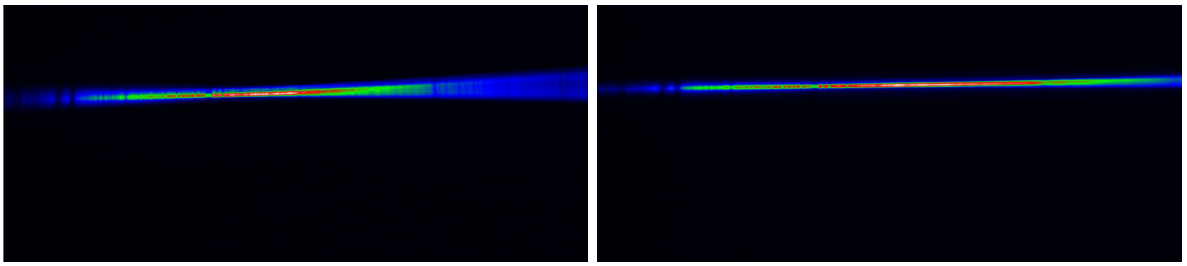

(a) One fibre illuminated - spectroscopy flange (b) One fibre illuminated - intermediate flange

Figure 6.2: Comparison of broadening of the imaging qualities.

Position on CCD	Intermediate flange FWHM [pix]	Spectroscopy flange FWHM [pix]
Left	17.6 $\pm$ 0.4	17.1 $\pm$ 0.4
Middle	12.5 $\pm$ 0.3	13.3 $\pm$ 0.4
Right	13.2 $\pm$ 0.3	28.0 $\pm$ 0.6
Mean	14.4 $\pm$ 2.7	19.5 $\pm$ 7.6

Table 6.2: FWHM for both flanges for 3 positions on the CCD.

The shown spectra and calculated FWHM are true for this example fibre. However all other analysed fibres result in the same conclusion: As expected, for imaging qualities the intermediate flange is better.

Conclusion of flange comparison

The intermediate flange was chosen for the set-up during the CINDI-2 campaign (and beyond).

Process of adjustment

For adjusting the CCD it is advisable to illuminate the system with sky light via the lightfibre as the single fibres are needed for determining the imaging qualities.

The mounting flange of the CCD is a tube, which fits into the spectrometer. To bring the CCD chip into the optimal position, it is recommended to do first a rough optimisation of the spectral resolution. After finding a reasonable spectral resolution, the imaging qualities can be optimised. The position of the CCD where the imaging optimum is reached is very narrow, so that adjustments needs to be minor movements until the optimum of spatial resolution is found. When the imaging properties are at the optimum, the spectral resolution should still be good and the final optimisation of it is done by the adjustment of the fibre to the spectrometer.

The flange gets fixed inside the spectrometer via a screw, that fastens a plastic ring around the tube of the flange. The screw needs to be tightened thoroughly as otherwise the adjustment can be disturbed when vibration occur (e.g. during transportation).

The CCD gets lifted when the screw is fastened. Therefore the fastening needs to be done iteratively: fastening the screw, correcting the position.

6.2. Adjustment of fibre to spectrometer

The fibre needs to be placed in the focal point of the mirrors of the spectrometer. In general this is easier than the adjustment of the CCD. Again, the instrument should be illuminated with scattered sun light. The quarzfibre's end is located inside the x-y adjustable fibre adapter. The fibre is inserted until the best spectral resolution is found. The general spatial resolution does not change a lot by moving the fibre, so by changing the position of the fibre a little bit the optimal spectral resolution can be brought to the chosen fitting window. Or, vice versa, the fit window can be brought to the center of the spectrum by changing the centerwavelength.

6.3. Adjustment of fibre to objective

At the telescope's side, the fibre needs to be attached to the objective. This procedure is complex and two people are needed to do it properly. This adjustment defines the field of view (FOV).

In contrast to final operation, the quarzfibre is illuminated from the spectrometer side. To avoid the need to bring a light source inside the spectrometer, it is advised to do it before the adjustment to the spectrometer in Section 6.2. Then the light fibre can be easily illuminated with scattered sun light. To ease the procedure it is best to darken the room.

The image distance of the objective needs to be set to infinity as the measured sunlight is approximately coming from infinity.

The quarzfibre's end needs to be in the focal point of the objective. The better the position of the fibre, the sharper the image at the entrance of the spectrometer is and therefore the better the field of view.

To adjust the fibre to the objective a theodolite is essential. A theodolite is a precision instrument for measuring angles both in horizontal and vertical planes. The instrument consists of a movable telescope, which can be moved precisely. The theodolite is mounted on a rail on a tripod, see Figure A.1 in the appendix. This provides small movements of the theodolite in vertical and horizontal plane.

For the procedure, the theodolite needs to be set-up in some distance from the objective on the same height and to be set to infinity as well as the objective.

With the rail and the tripod it is possible to adjust the telescope step by step to a position precisely in the field of view of the light fibres.

When this is successfully done, it is possible to bring the lightfibre in the focal point of the objective. When the single fibres can be seen sharp with the theodolite, then the optimal position is achieved. Because the optimal range is very narrow and fixing the fibre can lead to minor movements, it is advised to control it after fixing.

As this procedure is very time-consuming and needs special equipment it is not advisable to do it on campaigns. To ensure that this procedure does not need to be done regularly, a special device to mark the location of the quarzfibre inside the objective holder was built. Two small bars fixed on each side of the fibre, which ensures that the fibre is stopped at the right position when it is inserted into the objective holder.

7. Characterisation of the imaging DOAS instrument

For the characterisation of every DOAS-instrument several characteristics have to be verified/studied to ensure good operation. For the CCD, two necessary properties (linearity and dark signal) and one optional (smear correction) are important. The smear correction is only needed for imaging instruments using no shutter. For the spectrometer the instrument reponse functions (often called slit functions) is an important quantity. These estimate the real spectral resolution of the whole set-up and are needed for the retrieval.

7.1. Linearity

To use a CCD-Detector for DOAS-applications a good linearity of the detector is crucial. As the DOAS-analysis is based on optical depth, i. e. ratios of intensities, any non-linearity of the CCD will cause structures in the residuals.

Measurement set-up and scheme

To test the linearity of the CCD it was illuminated directly and uniformly by a stabilised white light source. Therefore the quarzfibre was removed and an entrance slit installed (to reduce the light). To ensure uniform illumination a teflon paper was fixed between lamp and entrance slit. Measurements were then taken over a great range of exposuretimes, starting at 0.1s and going up, until single pixels got into saturation around 70 s. In the beginning smaller steps were used to find any problems as non linearity for very small exposuretimes. For moderate exposuretimes, no problems were expected, so larger steps were applied until coming into the range where first saturation effects were expected. This resulted in a measurement scheme summarised in Table 7.1. To control that the lamp is stable in the nearly 3 hours of these measurements, five reference measurements were taken before and after every change of step size.

Exposuretime [s]	**Step size [s]**
0.1 - 1	0.1
1 - 10	1
10 - 60	10
60 - 70	1

Table 7.1: Measurement scheme for the analysis of CCD-linearity.

Measurements were repeated for the two detector modes (High Capacity/ Low Noise) and for every amplifier. Always the fastest readout of 3 MHz was selected.

The most important properties,which differ between the two modes are the register well depth and read noise (Table 5.4 in sec. 5.3.3).

- Register well depth:
  - Low Noise: 150,000 electrons
  - High Capacity: 600,000 electrons
- Readout Noise (3MHz):
  - Low Noise: typically 11 electrons
  - High Capacity: typically 40 electrons

Another difference are the possible amplifier settings:

- High Capacity:
  - 4 electrons/count
  - 8 electrons/count
  - 16 electrons/count
- Low Noise:
  - 1 electrons/count
  - 2 electrons/count
  - 4 electrons/count

The amplifier describes, how many electrons are collected to one count. This means, for an amplifier of 16 electrons per count, that smaller light sources are not measured. This is not the case for an amplifier of 1 electron per count. There every electron is measured, resulting in high sensitivity. However if a strong source is measured, the register well depth limit is reached early resulting in saturation.

Therefore the Low Noise mode is used for weaker light sources taking advantage of the high sensitivity. High capacity is the optimal choice for strong emitting sources, taking advantage of high storage possibilities.

Both modes however are limited by the ADC, which has a digitization of 16 bit. Therefore only count values up to 65,536 (2^{16}) can be digitized.

Reference measurements

In Figure 7.1 the stability of the lamp is shown for two options: The most stable condition and the most varying reference measurements. The most stable condition was during the measurements for Low Noise with amplifier $2e^-$ per count. The lamp showed only varying intensities up to 2% in a few pixel columns. Most pixels are better than 1%. During the measurements for Low Noise with amplifier $1e^-$ per count, the lamp showed quite some instability. Between the 5 reference measurements the intensity changes up to 4% from one measurement to another one.

This should be a sufficient stability of the lamp to analyse the linearity of all measurements.

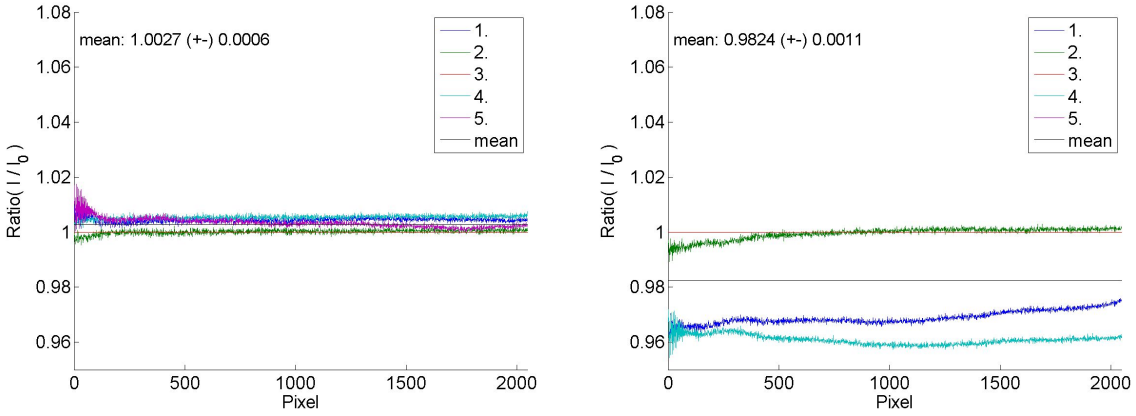

(a) Low Noise, $2e^-$ per count

(b) Low Noise, $1e^-$ per count

Figure 7.1: Reference measurements during linearity measurements.

Linearity measurements

For the linearity analysis the measured intensities (with dark spectra subtraction) were divided by a reference intensity of 1s exposuretime (and plotted against the respective exposuretime ratio in Figure 7.2). This analysis allows to easily analyse the linearity, as it is represented by the slope of a linear fit. As an additional measure the coefficient of determination of the linear fit R was calculated. This coefficient describes how well the data fits to the fitted linear model by having a value between zero and one.

Figure 7.2 shows the resulting linearity plots for all 6 possible combinations of modes and amplifiers. For the mode High Capacity all amplifiers show very good linearity properties. The slopes with 0.998, 1.001 and 1.007 show a very good linearity of nearly 100%. The correlation coefficients fortify the linearity with values better than 0.999969.

For the mode Low Noise this applies to two of the three possible amplifiers: $4e^-$ per count and 2 e^- per count. The slopes of 0.995 and 0.999 indicate also a very small non-linearity of max 0.5%. The correlation coefficients are better than 0.999996.

However the amplifier of $1e^-$ per count (Figure 7.2(f)) shows some non-linearity. The reason is the limit of digitization. With the high sensitivity, the limit of 2^{16} counts is already reached, as every induced electron is counted. This does not happen for the other options, as not every electron is counted. Therefore the limit for the single pixels is reached, before the digitization limits is a problem.

If the last measurements (reaching the digitization limit) are excluded, the linearity of the amplifier can be analysed again. The slope and offset improves, but has still a non-linearity of $\sim 1.3\%$. The correlation coefficient also improves to 0.999998.

Conclusion

The official statement for the CCD guarantees a linearity better than 99%. This is fulfilled for all amplifiers of the High Capacity mode and for 2 of 3 of the Low Noise mode. Only the last one ($1e^-$ per count) shows greater non-linearity.

In terms of linearity every option could be used, but due to the large field of view of the imaging DOAS, which implies a lot of light coming onto the detector, an amplifier of 1 electron per count is not of great use for our purposes.

As a first setting for testing and also for the first campaign the most linear mode was selected: Low Noise with an amplifier of 4 electrons per counts, as this is the mode with less noise and the amplifier allowing the most light detection for this mode.

For the selected settings, the linearity is examined for the mapped fibres on the CCD. The pixel binned to one fibre are determined in Section 8.3. In Figure 7.4 the slopes of the linear fittings for each binned pixel range are plotted. Fibre number 1 is at the top of the CCD chip.

The distribution of the linearity is not evenly spread over the chip. The best linearity is found on the edges of the CCD and in the middle of the CCD it is the worst. But the scatter with $\sim \pm 0.3\%$ is small and therefore negligible.

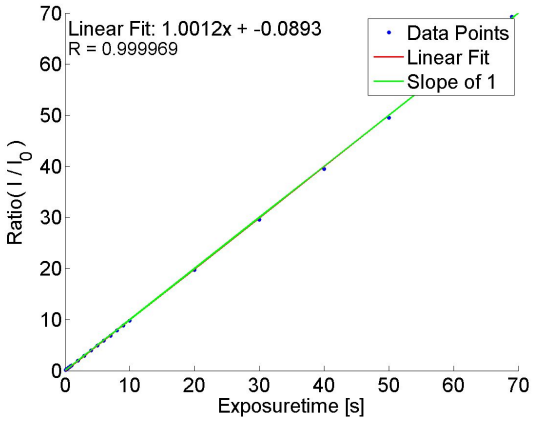

(a) High Capacity, 16e$^-$ per count

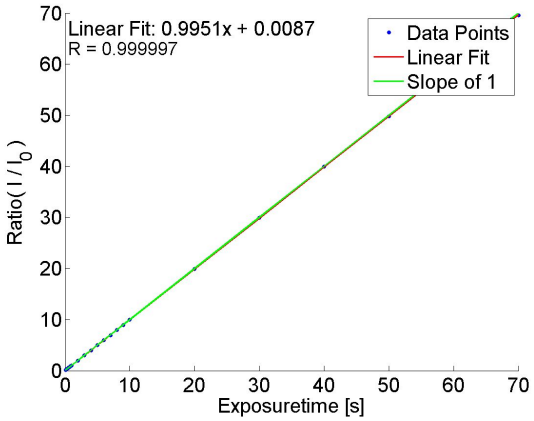

(b) Low Noise, 4e$^-$ per count

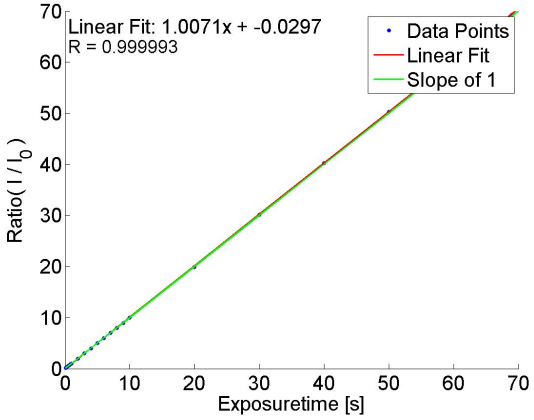

(c) High Capacity, 8e$^-$ per count

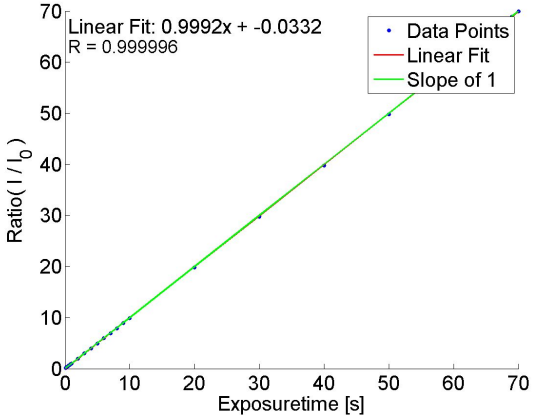

(d) Low Noise, 2e$^-$ per count

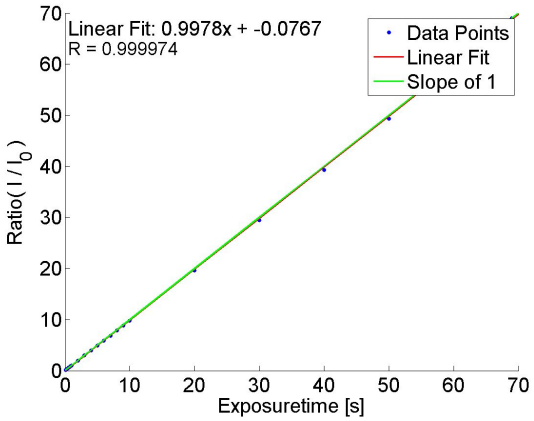

(e) High Capacity, 4e$^-$ per count

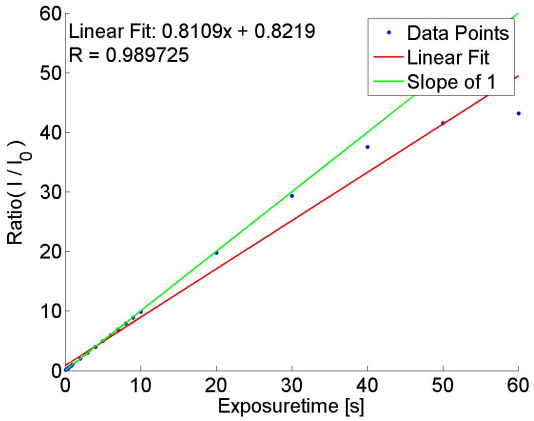

(f) Low Noise, 1e$^-$ per count

Figure 7.2: Linearity analysis for all possible options.

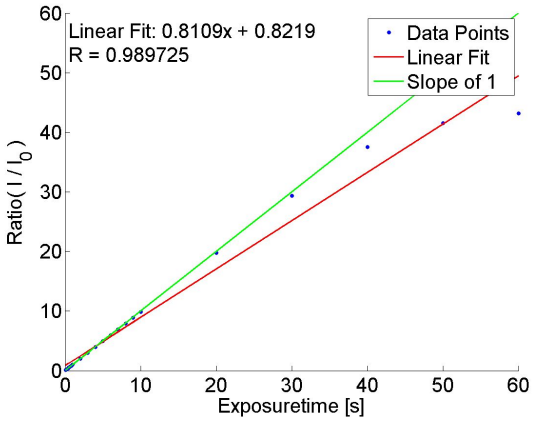

(a) Low Noise, 1e⁻ per count

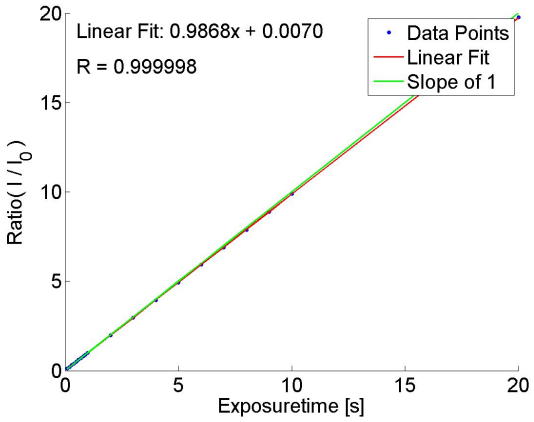

(b) Last measurements reaching digitization limit excluded from (a)

Figure 7.3: Further linearity analysis for Low Noise, 1e⁻ per count.

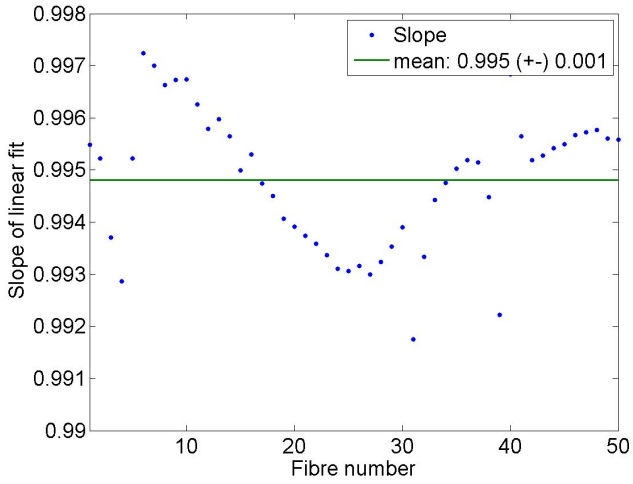

Figure 7.4: Linearty for each fibre for Low Noise, 4e⁻ per count.

7.2. Dark signal

The dark signal is the recorded signal of the CCD without illumination and consists of two components: a constant offset and thermally induced electrons (as mentioned in Section 5.3.3). The number of induced electrons depends on temperature and exposuretime. The offset should not be affected by either and stay at a constant value. For the characterisation the temperature and exposuretime dependence on the mean value of the chip and the standard deviation for each pixel is examined. The temperature dependence needs to be done once to select the optimal temperature setting of the CCD. The measurement of the dark signal for varying exposuretimes however needs to be done regularly for the chosen temperature, because the dark signal can change over time. For the current IUP-Bremen MAX-DOAS systems it is done every night.

Measurement set-up and routine

To measure the signal recorded without illumination, the shutter of the spectrometer was closed.

For a first analysis different settings for one fixed temperature (-35°) were compared (averaging over 25 measurements):

- The two modes
  Different process of readout leads to different amount of readout noise.
- Two amplifiers
  Different sensitivity leads to different amount of readout noise.
- One set-up repeated a few hours later
  Examination of change during a few hours.

Afterwards one mode and one amplifier was selected for the measurement routine. For temperature analysis, T was increased from -10°C to -60°C in 5°C steps. For each temperature measurements of 0.025 s to 12.8 s exposuretime were taken and averaged over 25 measurements.

Dark signal measurements

In Figure 7.5 the influence of different options on the mean dark signal is studied. The shape of each option is nearly the same. The mean and the standard deviation of the dark signal is almost constant for different exposuretimes.

- Low Noise Mode - High Capacity Mode
  Smaller values are measured for the mean value for the High Capacity mode.
  → This was not expected due to the CCD specifications.

  Values for standard deviation depend on the amplifier setting.
  → This was expected due to the different electron to count conversion.

- Amplifier: of 1 electron per count - Amplifier: 4 electron per count
  Higher mean signal and standard deviation are measured for the amplifier of 1 electron.
  → This was expected due to higher electron to count conversion.

- Repeated measurement
  The signal stays on the same level of counts, but the variation is different for each exposuretime.
  → Fluctuations were expected.
  Fluctuation are largest for this setting, because of the 1 electron to 1 count conversion

As a conclusion it does not really matter which option is selected to study the temperature dependence. However, it is important to do dark measurement for applied setting as it changes significantly for each option.

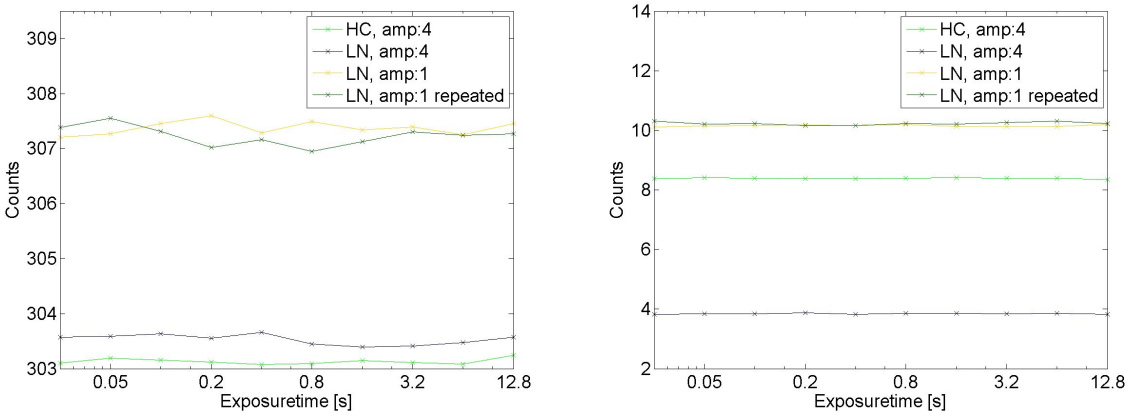

(a) Mean dark signal

(b) Standard deviation

Figure 7.5: Dark signal for different detector options (HC: High Capacity; LN: Low Noise).

For the temperature dependence analysis the settings: Low Noise and the amplifier 4e/count are used. The mean dark signal for all measured temperatures is plotted in Figure 7.6.

The scatter of the mean dark signal is little. It scatters between in the range of 302-305 counts. There is a small dependency on temperature visible. The 'level' of the mean dark signal changes with temperature. There is no clear correlation between temperature and counts, but a tendency to a higher count rate for the lowest and highest temperatures. The lowest count rate is achieved for medium high temperatures around -30°C. The shapes of the curves do not show any significant dependency on exposuretime.

For the standard deviation there is however a dependency on temperature. For higher temperatures the standard deviation is large and decreases with decreasing temperature. For lower temperatures, the gradient of counts gets smaller. The shape of the curves as function of exposuretime seems random, with a tendency to a straight line.

As the mean dark signal and standard deviation do not show any significant influence by the exposuretime the thermally induced electrons do not have a great impact on the dark signal. The constant offset contributes most of the dark signal and it is nearly stable with temperature.

Conclusion

It is important to do dark measurement for the applied setting as it changes significantly for each option.

Some dependency on temperature of the dark signal is visible. As the settings of -35°C is the typical temperature applied to CCD's for IUP-Bremen DOAS instruments and shows both in mean dark signal and standard deviation small counts, this temperature setting was chosen.

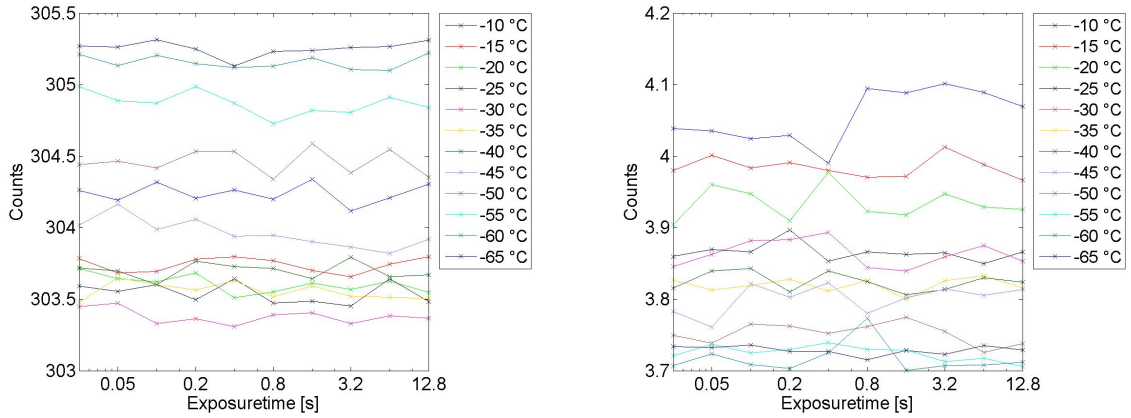

(a) Mean dark signal

(b) Standard deviation of the dark signal

Figure 7.6: Dark signal for different detector temperatures as function of exposuretime.

7.3. Smear correction

The smear correction is needed for imaging instruments using a full frame CCD without mechanical shutter. It corrects for the light collected during the read out process.

This can be done by estimating the duration of readout per pixel line. During the readout process, the first line is shifted immediately into the readout register. All other lines are shifted one line upwards. When the readout of the first line is done, the second line is shifted into the register and all lines are again shifted upwards.

During the readout of the first line, all other lines were illuminated for the duration of it. Being shifted upwards the second line got light which is normally directed onto the first line. As this is an imaging instrument and there is spatial information present on the CCD, this is a sequential problem. MAX-DOAS systems don't need a smear correction, as the whole CCD is measuring one elevation angle.

The problem of illumination during readout can be solved with the smear correction. It was implemented into the measurement software by A. Richter. With an estimated readout time of 0.00033 s per line, the 'falsely' collected light can be corrected:

- First row: no correction needed
- Second row: 0.00033 s worth of light collected by the first row subtracted
- Third row: 0.00033 s worth of light collected by the second row and 0.00033 s worth of light collected by the first row subtracted
- And so on...

7.4. Instrument response function

In Figure 7.7 the effect of the instrument to a monochromatic light source is illustrated. The broadening of the line spectra to an approx. Gauss-function is different for each instrument. The resulting Gaussian curve is called the instrument response function. The full width half maximum (FWHM) of the curve is regarded as the spectral resolution of the instrument. To be able to compare measured spectra, they need to have the same resolution. For the DOAS analysis the high resolution cross-sections of the trace gases measured in the laboratory need to be brought to the lower resolution of the DOAS instrument. This is done by convolving the high resolution spectra with the instrument response function. If the measured spectra do not fit to the reference cross-sections, it can't be compared/ fitted correctly in the DOAS analysis, which leads to big structures in the residual and wrong amount of trace gases in the light path. The characterisation of the instrument response function is therefore an important task. For the imaging DOAS instrument each viewing direction (each binned part on the CCD), has its own slit-function. Therefore the changes of the slit function over the vertical CCD position is accounted for, but the change of the slit function over the wavelength axis (x-axis) needs to be examined.

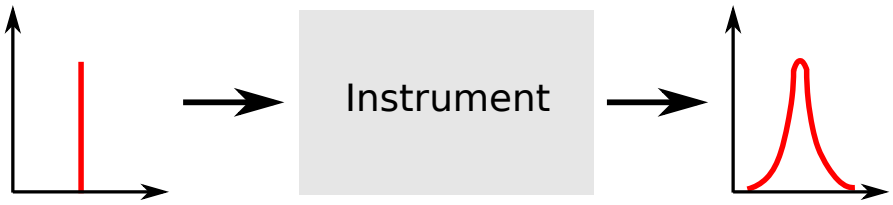

Figure 7.7: Effect of the instrument to a monochromatic source.

Measurement set-up and routine

The characterisation of the slit-function was done by illuminating the system with a Hg-Cd calibration lamp. It is possible to change the angle of the grating in the spectrometer. By adjusting the center wavelength, the grating rotates to bring the chosen center wavelength to the middle of the spectrum measured by the CCD. For the analysis the peak at 436 nm was used, which has a strong intensity as one of the main emission lines of the Hg spectrum. At a center wavelength of 550 nm the peak appeared on the left side of the spectrum. The whole spectrum of the lamp was then measured in 5 nm steps, until the peak disappeared at the right side at a center wavelength of 365 nm. With this procedure the peak is recorded 28 times. In the end the shape of the slit-function is known for the whole pixel range. The pixel range can then be converted to a wavelength axis according to the center wavelength used for operation.

Measurements of the instrument response function

For each center wavelength the whole spectrum of the Hg-Cd lamp was measured. Therefore the chosen 436 nm Hg peak needed to be picked out of all the measured peaks, see Figure 7.8 (436 Hg peak highlighted in red).

This way, the shape of the peak for 28 positions on the CCD was determined. They are plotted in Figure 7.9(a) and fitted with a Gaussian function. For this plot, the x-axis is already converted to wavelengths (in this case for a center wavelength of 465 nm). The shape of the monochromatic line changes along the CCD. In the middle of the chip, the intensity is largest and the line has a Gaussian shape with a small FWHM. Towards the edges, the peak gets broader and is no longer Gaussian.

From fitted Gaussian functions the FWHM is calculated and plotted in Figure 7.9(b). The error bars for the FWHM are the 95% confidence bounds of the Gaussian fit. Because of the misshaping of the peaks towards the edges the fit is worse and the errors are increasing.

Figure 7.9(b) shows clearly the large change of the FWHM over the spectral range of the CCD. Inside the fitting window from 425 to 490 nm the FWHM changes from 0.68 nm (middle) to 1.065 nm (edge) which is a 57% difference. This could lead to problems in the analysis as normally a constant FWHM is used for the convolution of trace gas cross-section as the FWHM usually changes in the range of only 0.01 nm. Consequently, not accounting for this effect would lead to structures in the DOAS fit residual.

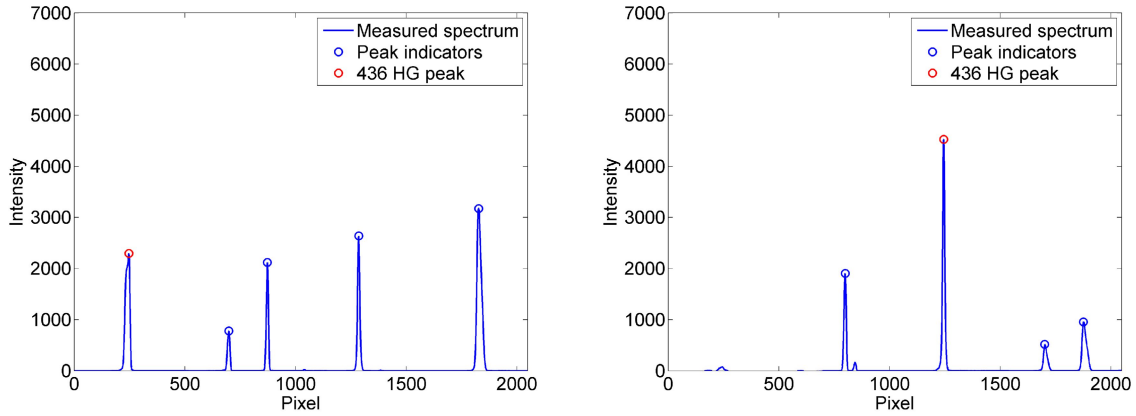

(a) Spectrum of a Hg-Cd line lamp for a center-wavelength of 490 nm.

(b) Spectrum of a Hg-Cd line lamp for a center-wavelength of 420 nm

Figure 7.8: Hg-Cd calibration lamp spectra for two different center wavelengths.

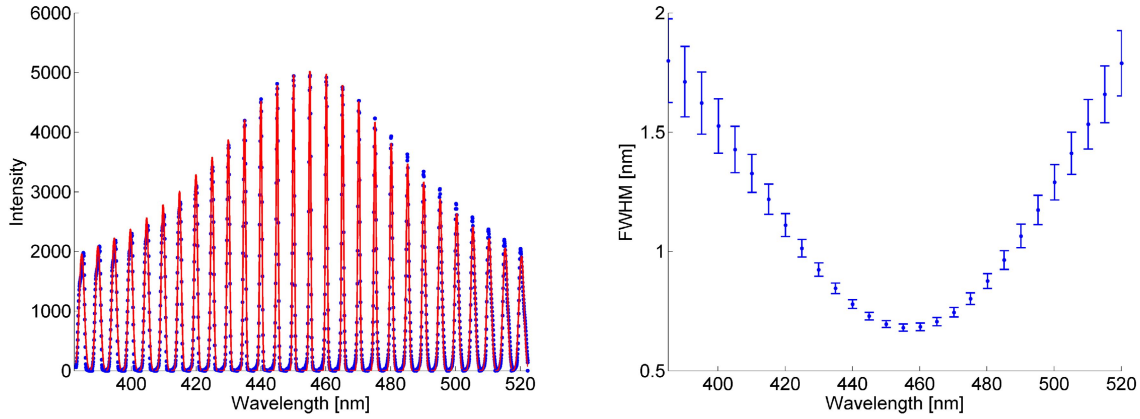

(a) Fitted Gaussian of the 436 nm Hg peak at different positions on the CCD chip (blue: measurement, red: fitted Gaussian)

(b) FWHM of fitted Gaussian in (a)

Figure 7.9: Analysis of 436 nm Hg peak and its FWHM over the spectral range.

8. The CINDI-2 campaign

The first application of the new imaging DOAS instrument IMPACT was the Cabauw Intercomparison campaign for Nitrogen Dioxide Measuring Instruments 2 (CINDI-2). The campaign took place in Cabauw, Netherlands in September 2016. An introduction of the campaign including the set-up is given in the next section. As last parts of the instrument arrived in August 2016 only, it was the first application of the instrument and not many tests other than adjustment were possible before. Therefore, a lot of improvements were done on site after installation of the instrument. Measurements with a xenon lamp for calibration lead to a lot of information of the field of view and dispersal in the spatial range. Both the improvements and the results of the xenon lamp measurements are presented in Sections 8.2 and 8.3.

A few days after the official start of the campaign the instrument was in its final state and routine operation started on the 15th of September 2016. Part of the measurements routine followed the official protocol of the campaign to compare to the other MAX-DOAS instruments and including IMPACT in the official intercomparison exercise. The rest of the time the imaging DOAS instrument used its ability to measure several elevation angles simultaneously to do complete hemispheric scans. The procedure and the official retrieval settings for the analysis of the measurement are described in Sections 8.4 and 8.5.

8.1. Introduction to the CINDI-2 campaign

The second Cabauw Intercomparison campaign for Nitrogen Dioxide Measuring Instruments (CINDI-2) was the successor of the first CINDI campaign which took place in Cabauw, Netherlands in June/July 2009. Like the first one it was mostly organised by The Royal Netherlands Meteorological Institute (KNMI). The patrons of the CINDI-2 campaign were the European Space Agency (ESA) and the International Network for Detection of Atmospheric Composition Change (NDACC). [22][29][15]. In CINDI-2, 29 different institutes were involved, whereby a lot of institutes contributed with more than one instrument.

Objectives

The major scienctific objectives of CINDI-2 are[15]:

1. "To assess the consistency of slant column measurements of several key target species (NO_2, O_3, O_4 and HCHO) of relevance for the validation of S5P and the

future ESA atmospheric Sentinels, through coordinated operation of a large number of DOAS and MAX-DOAS instruments from all over the world."

2. "To study the relationship between remote-sensing column and profile measurements of NO_2, HCHO and O_3 and reference in-situ concentration measurements of the same species."

3. "To investigate the horizontal representativeness of MAX-DOAS measuring systems in view of their use for the validation of satellite tropospheric measurements featuring ground pixel sizes in the range of 25-50 km^2."

8.1.1. Measurement site and instruments

Measurement site

The Remote Sensing Site (RSS) 'Cabauw Experimental Site for Atmospheric Research' (CESAR) is managed by KNMI and is often used for campaigns similar to CINDI e.g. High Definition Clouds and Precipitation for advancing Climate Predictions (HD(CP)^2). The advantage of the RSS is the meteorological tower providing a lot of additional meteorological data and the possibility to install instruments in altitudes up to 200m [29]. In Figure 8.1, the estimated NO_2 distribution in the Netherlands in 2001 is shown. Close to Cabauw only a few local sources of NO_2 (mostly agricultural environment) are found. However, within a radius of $<$ 40km the four largest cities of the Netherlands can be found, which are strong sources of anthropogenic NO_2. The NO_2 pollution in Cabauw is therefore strongly wind dependent. In addition, on a local scale, the measurements at RSS depend on sources nearby like the street from Utrecht to Rotterdam (directly next to the RSS). This leads to large variability of NO_2.

Participating instruments

Compared to the first CINDI campaign a lot more instruments participated: While only 22 DOAS-like instruments participated in 2009, in the second campaign 38 DOAS-like instruments were installed. Also more additional instruments like in-situ instruments or sondes were used. The instruments are listed in Table A.1 in the appendix.

The DOAS-like instruments can be grouped: Static MAX-DOAS (33x), mobile DOAS (3x), Long Path DOAS (1x) and Cavity-enhanced DOAS (1x). The static MAX-DOAS group itself can be divided in two/three parts: 1D, 2D and imaging instruments. IMPACT was the only imaging instrument as a second one from Finland was announced but participation then cancelled.

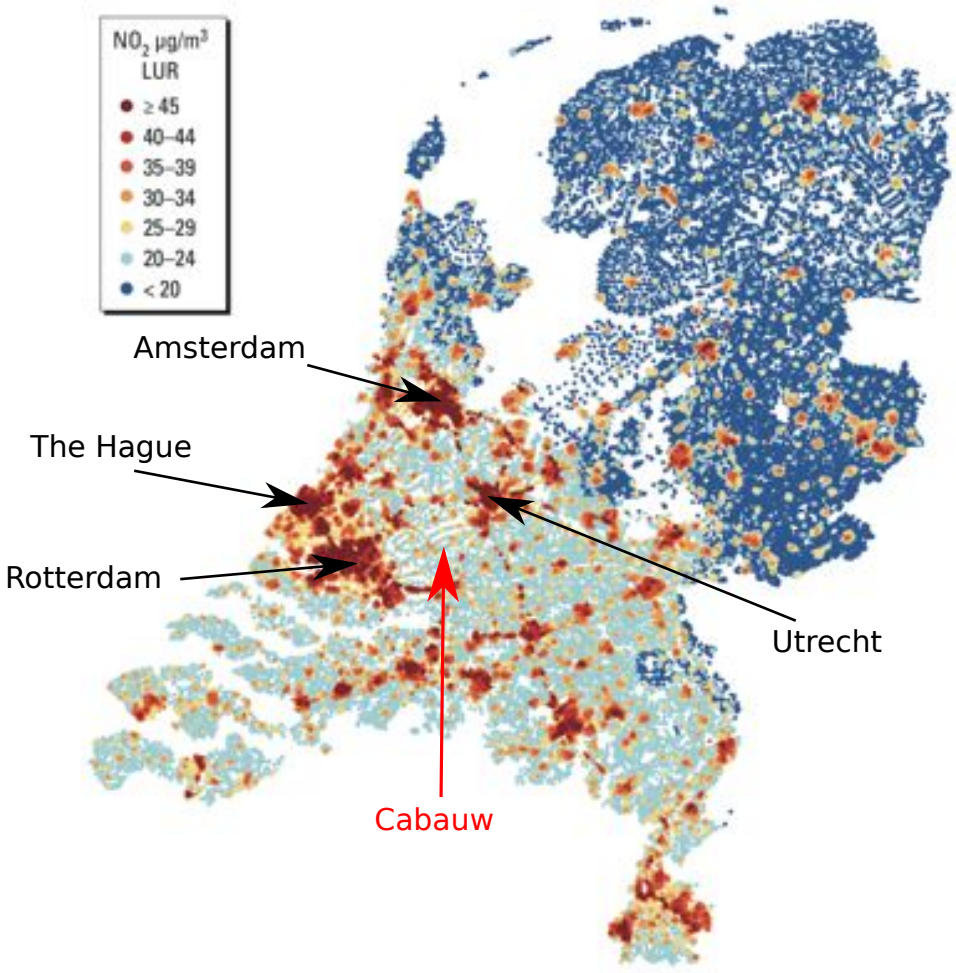

Figure 8.1: Distribution of the estimated mean NO_2 surface concentrations in the Netherlands for the year 2001, based on land use regression models [15].

The mobile DOAS systems were installed in cars or on a bike and did tours around the measurement site to investigate the variability inside a satellite pixel. The Long Path DOAS (LP-DOAS) was installed on a field 3.8 km away from the tower. On the tower the retroreflectors were installed at four different altitudes. At the same platforms were also most of the in-situ instruments and the Cavity Enhanced DOAS (CE-DOAS) installed. Next to the tower the NO_2 LIDAR was operated.

A few hundred meters from the meteorological tower, the static MAX-DOAS and the truck containing the Raman LIDAR CAELI were placed. In Figure 8.2 the position of all instrument groups at the measurement site are indicated.

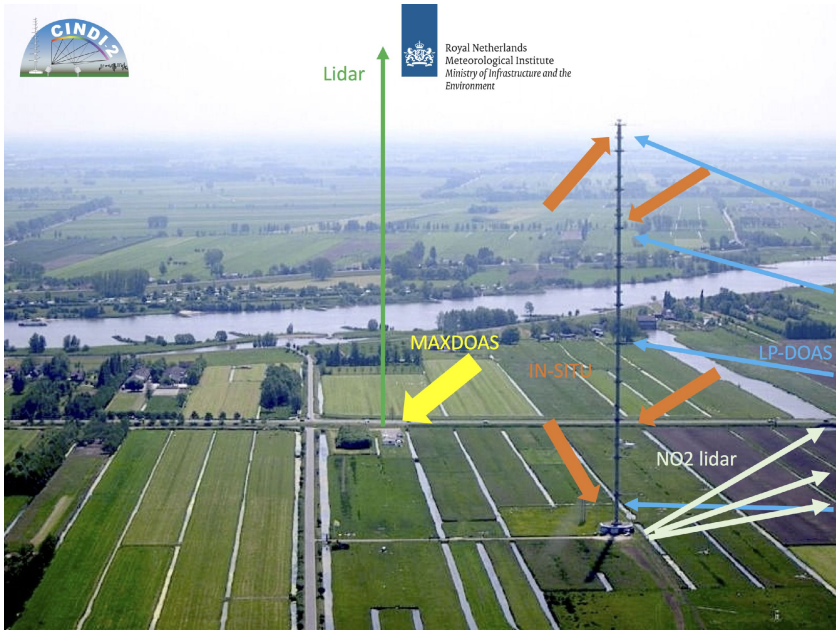

Figure 8.2: Location of the different types of instruments at the Ceasar Site [15].

To accommodate all instruments temporary containers were arranged. In Figure 8.3 a picture of the installed containers can be seen. The ground level consists of 12 containers in a row plus 3 units accommodating one meeting room. The upper level consist of 7 containers. On each side staircases enable access to the roof of the ground level units. On this roof the 1D MAX-DOAS instruments were located. As these measure only in one azimuth angle, they are fixed on the roof. The 2D MAX-DOAS instruments followed a strict measurement protocol, which included several azimuth angles. Therefore, they needed an undisturbed view, which was achieved by putting them onto the roof of the top level units. The measurement protocol is described in more detail in Section 8.4.

Figure 8.3: Set-up on roofs of containers: Ground level: 1D MAX-DOAS; Top level: 2D MAX-DOAS.

8.1.2. Setting up

Timeline

The official timeline is illustrated in Figure 8.4. End of August the site opened and the installation phase started followed by the warm-up phase. The semi-blind intercomparison started on the 12th of September. It took two weeks with 2 weeks for possible extension (e.g. bad weather conditions would disturb the semi-blind intercomparison). However, this was not the case as the overall weather situation was very good, which can be seen in Figure 8.5. A lot of days were extraordinary good with almost cloud-free conditions. The semi-blind intercomparison ended officially on the 28th of September.

The first part of the Bremen IUP crew (Enno Peters, André Seyler and myself) and Stefan Schreier from BOKU arrived late in the evening at the RSS on 5th of September. The next days the two IUP-Bremen and the BOKU instrument were set-up. With beginning of the semi-blind intercomparison the instruments were fully operational and the BOKU and IUP-MAX-DOAS instruments started measuring. However, as this was the first set-up of IMPACT a lot of challenges occurred on site. Necessary improvements were finished on September 14th and IMPACT participated in the semi-blind intercomparison from September 15th till the end. The improvements are described in the next section.

The Bremen instruments were dismantled on the 4th of October.

Set-up of instruments on containers

All three instruments were set-up on the roof of the top level containers. The pan-tilt head of IMPACT was mounted on a tripod as can be seen in Figure 8.6. It was fixed with tension belts to the ground.

Figure 8.4: Calender for the CINDI-2 campaign [16].

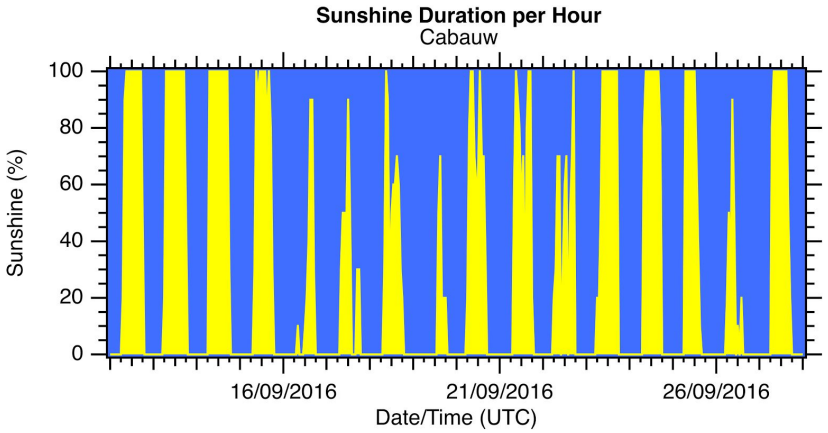

Figure 8.5: Sunshine duration for Cabauw during the campaign [20].

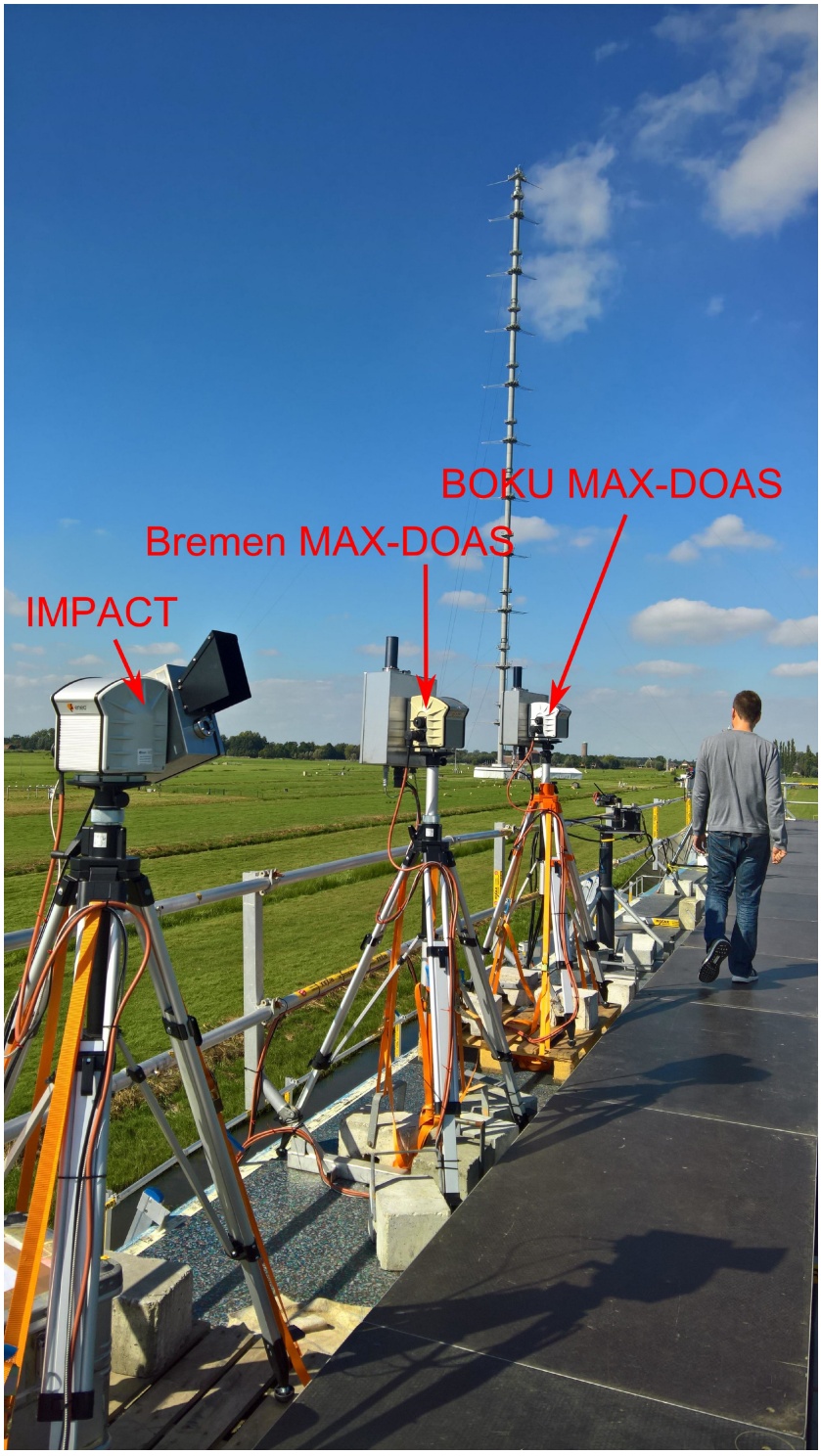

Figure 8.6: Set-up of the IUP-Bremen instruments on the roof of the containers.

8.2. Improvements on site

8.2.1. Installation of a filter

After first measurements it became clear that a filter is needed in front of IMPACT's objective to reduce the incoming radiation. Without the filter, several azimuth angles close to the sun were saturated. Two possible filters were available at the campaign. A 3 mm HEBO B39 and a 3 mm HEBO NF04 filter. The B39 is a blue color filter glass and the NF04 a neutral density filter glass. The transmission curves per 1mm thickness are shown in Figure 8.7. The B39 reduces the incoming radiation from higher wavelength than 700 nm which leads to less straylight from these wavelength region. Furthermore it decreases the radiation for the used wavelength region of 425-490 nm by up to $\sim$ 59% transmission for 3 mm thickness. This filter is installed at the spectrometer side anyways in order to reduce straylight problems.

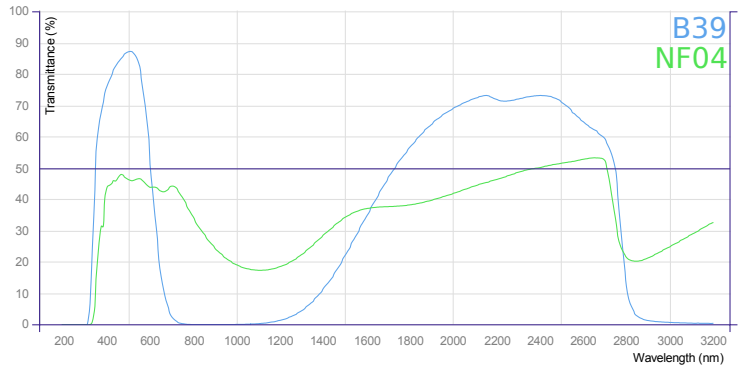

Figure 8.7: Transmission curves of different filters [14].

For the IMPACT instrument during CINDI-2 the stronger filter NF04 was used. This filter has only a transmission up to $\sim$11% at 3mm thickness. This results in a worse signal to noise ratio and larger exposuretimes of typically 1.6-6.4 s. However, it ensures nearly no saturation apart from the measurements directly to the sun. As the objective of the imaging instrument work was to take part in the intercomparison and the results had to be reliable without any saturation effects, the NF04 filter was chosen.

After the campaign a bug in the software correction of the smear correction was found. The saturation control was performed only after smear correction. Consequently, many saturated measurements were not classified as such. With the corrected version of AMAX_OMA it is believed, that a much weaker filter is enough to ensure good IMPACT measurements and much shorter exposuretime.

For further measurements it would be advised to do more tests to find the optimal filter with best compromise of signal to noise ratio and saturation.

8.2.2. Dark pixel exclusion

After a first data analysis, some big spikes could be seen in the residual. The position of the spikes could be traced to a column of the CCD, which had some dark pixels. In Figure 8.8(a) the dark pixels can be clearly seen. The length of the affected pixels depend on the exposuretime. At long exposuretimes only one pixel is dark. The shorter the exposuretime is, the greater is the amount of pixels affected by this dark pixel due to the readout. The shown spectrum is recorded at a very short exposuretime. Furthermore it affects the next column, which can be seen in Figure 8.8(b), which is a zoom-in of the concerned spot.

By excluding both affected columns in the data analysis it was possible to eliminate the spikes in the residual.

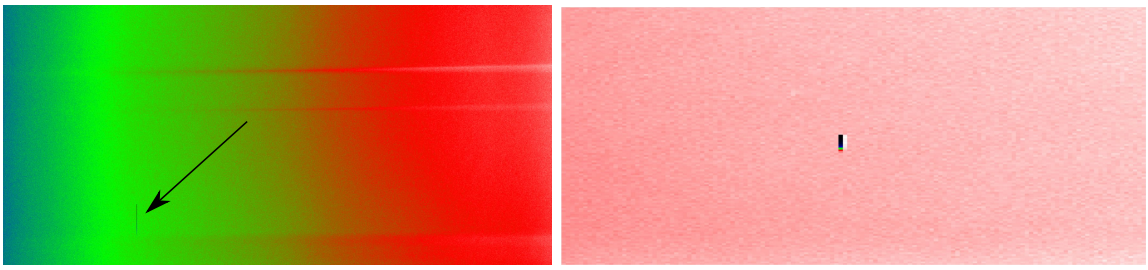

(a) Whole CCD: Dark pixel influences the rest of column

(b) Zoom onto defect: Next column also infected

Figure 8.8: Pixel defect: Dark pixels on the CCD chip.

8.2.3. Mix of single fibres

During the data analysis some inconsistency was detected.

At first a malfunction of the pan tilt head was suspected. It seemed, that some angles were not properly adjusted. However, by redoing some measurements, the problem remained and the pan tilt head worked properly.

A horizon scan helped to identify the source of the problem: By moving slowly the pan tilt head, so that one fibre after another is illuminated above the dark horizon, it could be clearly seen that two pairs of fibres were exchanged. In Figure 8.9(a) and (b) 2 images of the horizon scan can be seen. In both images it can be seen, that one fibre is skipped and instead the next one is illuminated.

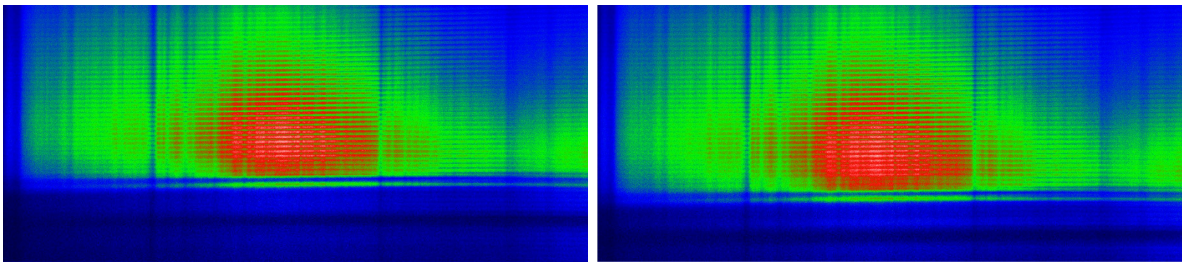

(a) Wrongly sorted fibre pair 1 (b) Wrongly sorted fibre pair 2

Figure 8.9: Horizon scan to investigate the inconsistency in measurements.

To conclude, the manufacturer made a mistake in properly sorting the single NCC fibres inside the fibre bundle.

This problem was discovered only after the intercomparison started and could of course not be solved. The wrongly sorted fibres are in the lower half of the CCD corresponding to the lower elevation angles, which are of importance.

With a calibration measurement done during the campaign in Cabauw it was possible to determine the characteristics of the spatial image and the field of view. This enables a software re-sorting of the exchanges fibres. After the campaign the fibre war repaired by the manufacturer.

8.3. Characteristics of spatial image and field of view

After sunset a xenon lamp was set up at a parking place at ∼1 km distance. By pointing at the lamp and measuring its light all instruments were aligned. This ensures that every instrument measures the same elevation and azimuth angles. For the imaging instrument this measurement provided the possibility to determine the exact elevation angles and the field of view for each fibre. Furthermore it allowed to determine the best binning range, which are the pixel lines of the CCD, which are binned to one viewing direction/ one single fibre.

Calibration measurement procedure

The azimuth angle was calibrated first. The telescope was moved in azimuthal direction until the highest intensity was found. The adjusted azimuth angle of the telescope was then corrected to the angle the lamp was placed.

Afterwards the elevation angle was calibrated. Therefore the telescope was moved upwards, until the lamp disappeared as being out of the field of view. Then an automatic

routine was started, in which measurements were taken in 0.2° steps moving the telescope downwards. This experimental set-up is illustrated in Figure 8.10(a). In Figure 8.10(b) the movement of the image of the calibration lamp over the fibre is demonstrated. As the xenon lamp can be seen as a small point source and its image is smaller than the single fibres, one fibre was illuminated for ca. 3-4 steps, then the next fibre was illuminated.

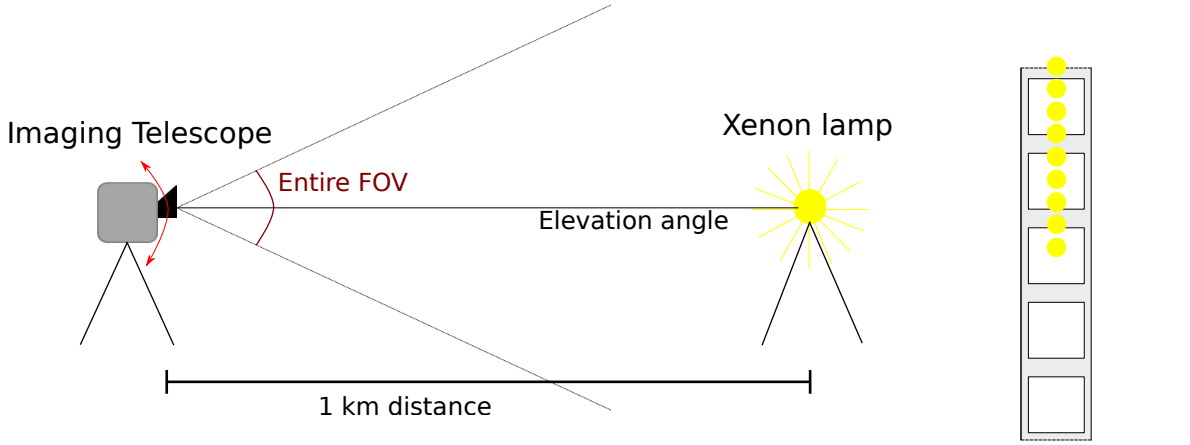

(a) Experimental set up for the calibration measurement

(b) Image of the lamp moving across the fibres

Figure 8.10: Calibration measurement.

8.3.1. Binning range

The measurement routine resulted in 250 measurements in which the lamp illuminated a single fibre. These raw measurements were processed to cross-sections of the 512 pixelrows by: subtraction of dark signal, division by the exposure time and averaging of all pixel columns of the fitting window.

These cross-sections show the shape of a Gaussian curve. Always 3-4 measurements (each 0.2°) show the same fibre. The Gaussian curves of all 51 fibres mapped onto the CCD are plotted in Figure 8.11(a). The fibres were illuminated one after another, so a little time has passed between each measurement. As the lamp was not stabilised, a little variation in intensity is therefore expected. One fibre however seems to have a significant lower intensity. This fibre has probably a smaller diameter compared to the other resulting in less light transmitted.

Furthermore, a significant overlapping of the fibres can be seen. Figure 8.11(b) is a zoom-in to single fibres. The neighbouring fibres have a lot of influence and even the next ones further away seem to interfere to some extent. This could cause problems, as

the differences in NO_2 in the lower elevation angles are large. Therefore it was decided to test more than one binning range to find the best solution. The first two choices were binning over a range of 3 and 19 pixels (3 pixels to minimize the overlapping effect and 19 pixels for taking nearly the whole fibre into account).

To complete the testing binning ranges a compromise was searched for. The maximum of the Gaussian shaped curves of the cross-sections represent approximately the center of the single fibres. The distance between maxima of neighbouring fibres vary between 9 and 10 pixels. As a result 9 pixels binning range was selected as a compromise.

In the end three binning ranges were selected: 3,9 and 19 pixels. The binning ranges are set around the center of the fibres (maxima of the Gaussian curves).

The three binning ranges are fixed over the whole CCD chip. However the width of the single fibres is not, which can be quantified by calculation the FWHM, see Figure 8.11(e). The smallest mapped fibres are located in the center of the CCD and get wider to the edge. Therefore a varying binning range could be tested. The varying binning range was selected by assigning every single pixel row to the fibre it contributes most. The selection was done by plotting the intensity of each CCD line, see Figure 8.11(d). The resulting curves shows several broad peaks for all the fibres it contributes to. The CCD line is assigned to the fibre with the highest peak.

However this procedure leads to binning ranges being nearly the same as the fixed 9 pixel binning ranges with differences of max. 1 pixel. Therefore it was dismissed with the expectation that the 9 pixel binning range would be the optimal choice. Nevertheless all three beforehand discussed binning ranges were tested.

Conclusion

For the tests of the binning ranges, measurement data from the campaign in the main direction was analysed and compared with the SC NO_2 of the Bremen MAX-DOAS.

In the end, the 9 pixel binning range was clearly the best choice.

- It had the most gradient between each fibre resulting in a large splitting of the single viewing directions.
- The signal to noise ratio was sufficient.
- Compared to the values of the MAX-DOAS it showed the best agreement.

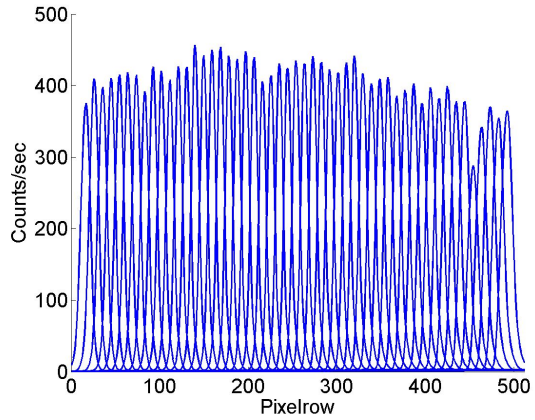

(a) Vertical intensity of the wholly mapped fibres

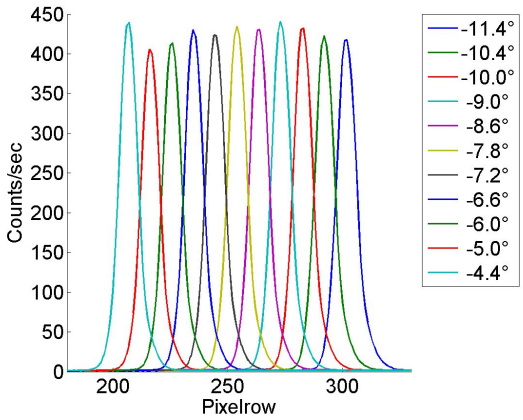

(b) Overlap of vertical intensity of the fibres

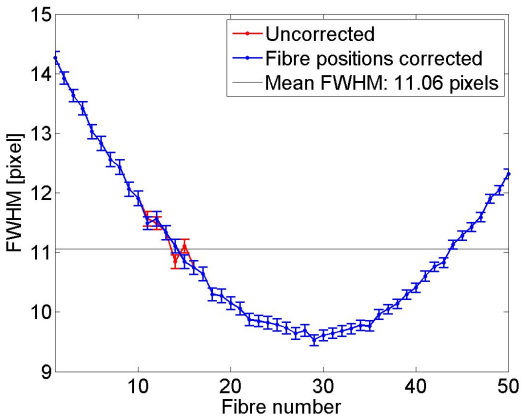

(c) FWHM of the fibres over the whole CCD chip

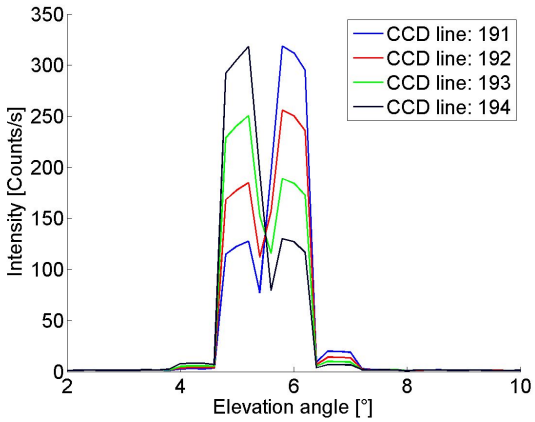

(d) Intensity distribution of CCD lines in dependence on elevation angle

Figure 8.11: Analysis of the calibration lamp measurement.

8.3.2. Elevation angles

After the binning ranges are set, corrected elevation angles are assigned to the fibres/ binning ranges. The first step was to calculate elevation angles for each CCD-line, which then can be averaged to one angle per fibre according to the binning range. Each CCD line has a specific intensity distribution over all elevation angles (see Figure 8.11(d)). By weighting the elevation angles with the measured intensity and dividing it by the overall intensity the weighted elevation per CCD line i is:

$$\text{Weighted Elevation}_i = \frac{\sum_i \text{Intensity}_i \cdot \text{Elevation}_i}{\sum_i \text{Intensity}_i}$$

To get an elevation angle for each fibre (binned CCD region), the weighted elevation angles are averaged for the designed binning ranges. This is illustrated in Figure 8.12. The blue line describes the weighted elevation and the white spaces indicate binning ranges for each fibre. The black stripes are unused columns.

Figure 8.13(a) is Figure 8.12 zoomed in on the wrongly sorted fibres. The wrongly sorted fibres change the pattern of the normal curve of the elevation angle. As the single fibres are influenced by their neighbours, the normal sorted fibres are influenced by the viewing directions directly below and above. For the exchanged fibres however the neighbouring fibres are not the viewing directions directly below and above, leading to influences from other elevation angles, see Figure 8.13(b). Plotted are the intensity distribution of all CCD lines which are binned to one of the exchanged fibres. The influence for the fibre comes not only from the neighbouring elevation but also from the elevation 1.5° away. The procedure of intensity weighted elevation angles accounts for this. By weighting with the intensity the CCD lines are assigned to a bigger elevation. This leads to the abnormal shape of the curve of the weighted elevation and nearly equal elevations for the exchanged fibres. After a first data analysis the assigned elevation angles could be proofed by the fact, that the NO_2 values are nearly the same for these viewing directions.

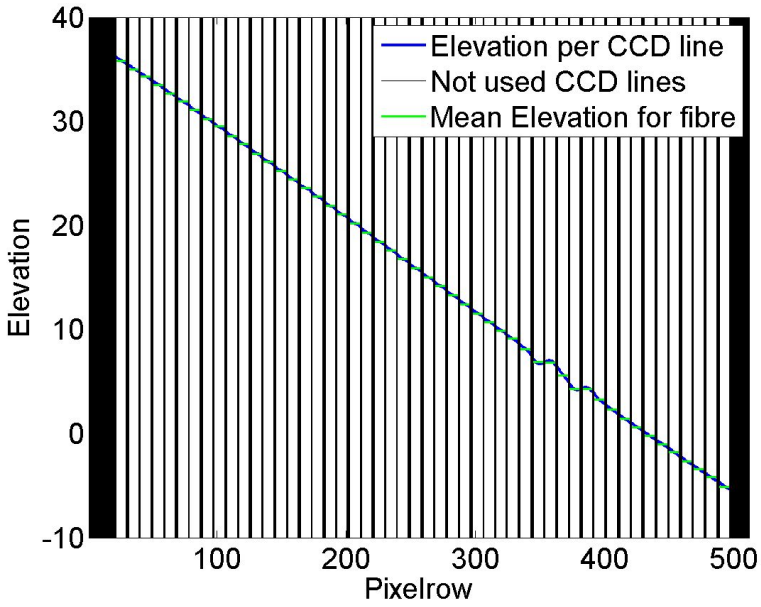

Figure 8.12: Intensity weighted elevation angles and their average inside the binning range.

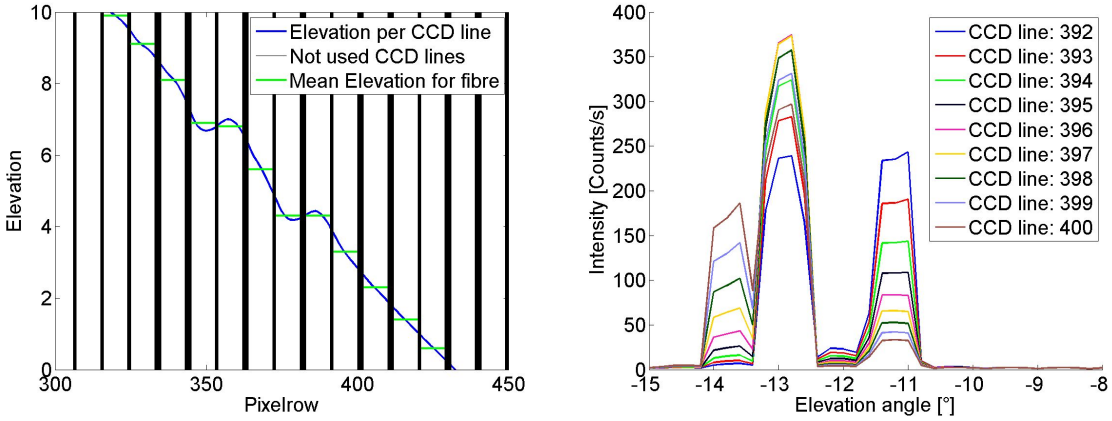

(a) Zoom-in on the wrongly sorted fibres.

(b) Intensity distribution for binned area of one fibre.

Figure 8.13: Averaging the weighted elevation angles for the binning ranges.

8.3.3. Conclusion

In summary Figure 8.14 is achieved, plotting the averaged intensity inside the fitting window (pixel columns 500-1500) as a function of pixel row and elevation. It describes very nicely the pointing characteristics of the imaging instrument.

The single fibres mapped onto the CCD can be clearly seen. The wrongly sorted fibres are obvious in this image. The black stripes are again the pixels not used for the analysis and the spaces between are the binning ranges for each viewing direction. The first and last rows of the CCD are not used as only fully mapped fibres are of interest. Furthermore the spatial resolution near the edges gets worse, so that in total 50 fibres were selected.

Because the distance between the fibres stays constant but the FWHM varies, the overlap of the fibres is varying. Near the edges the overlap is larger and the neighbouring fibres are influencing more. This can be seen by the intensity coming from other fibres into the binning range. Some part of the crosstalk between the fibres is due to the spectrometer aberration.

However, the darker regions for elevation angles in between the fibres show, that the adjustment of the fibre to the objective is well done and the image is well focused onto the fibre's end. This leads to a good field of view. As one fibre was illuminated for around 4 movements of the pan tilt head, one fibre catches light of several elevation angles. As the step size was 0.2° the field of view is $\sim 0.8°$, but effectively increased due to overlaps to a larger field of view than e.g. the Bremen MAX-DOAS (FOV: $\sim 1°$).

8.4. Measurement protocol

The official measurement protocol comprised 7 different azimuth directions and up to 10 elevation angles. The azimuth angles are illustrated in Figure 8.15 on a Google earth map. The main direction is 287°, in which the city The Hague is located. This is the direction all 1D instruments are pointing to. Other directions are used by the 2D instruments.

As the protocol is very tight for the 2D instruments and includes a lot more measurements, it was decided to act as a 1D instrument and follow parts of their protocol. This allows the imaging instrument to participate in the intercomparison, to compare the results with all instruments, but also to do full hemispheric scans to exploit the advantages of the imaging instrument. The position on top of the container allows complete scans with (almost) undisturbed view in all directions.

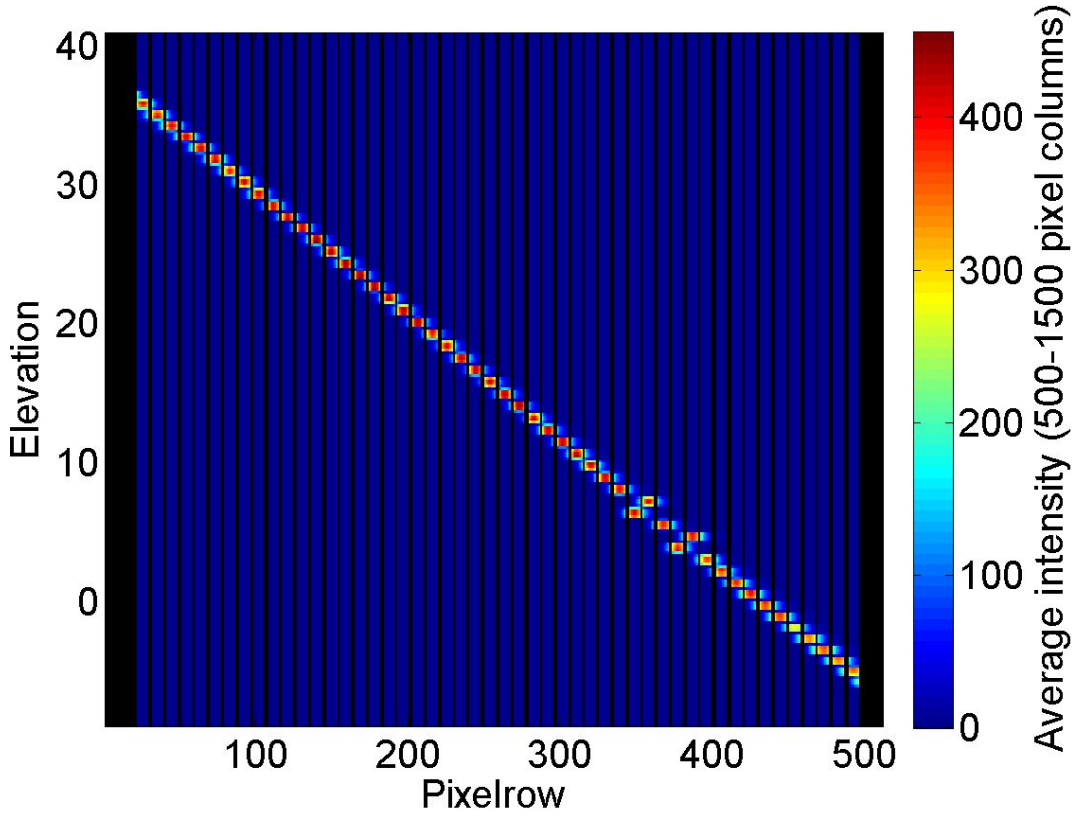

Figure 8.14: Averaged intensity of the calibration lamp as function of pixelrow and elevation angle.

In the following, an overview about the operation of the instrument is given:

- Followed official intercomparison protocol [16]
  - Starting at 06:00:00 UTC in the morning, ending 16:00:00 UTC
  - Done every hour in the first 15 minutes
  - Azimuth angle: 287°
  - Elevation angles: 1, 2, 3, 4, 5, 6, 8, 15, 30, 90°
    (Could not be adjusted exactly by IMPACT due to imaging-elevation characteristics)
- Hemispheric scans
  - In between the sequences of the official protocol
  - Azimuth angles: Starting at -175° in 10° steps to +175°
  - Elevation angles from -5.1° to 35.8° simultaneously

8.5. Retrieval settings

The imaging instrument's wavelength region covers only the species NO_2 and O_4. For the other instruments there were several other species, e.g. formaldehyde (HCHO). Table 8.1 lists the official DOAS settings for NO_2 and O_4. For the intercomparison these settings were used for the measurements according to protocol.

For the hemispheric scans the settings were also kept except for the reference. Here synchronised reference spectra were used: zenith measurement closest in time. This was done to compensate for instrumental changes or higher background NO_2 to get more reasonable results.

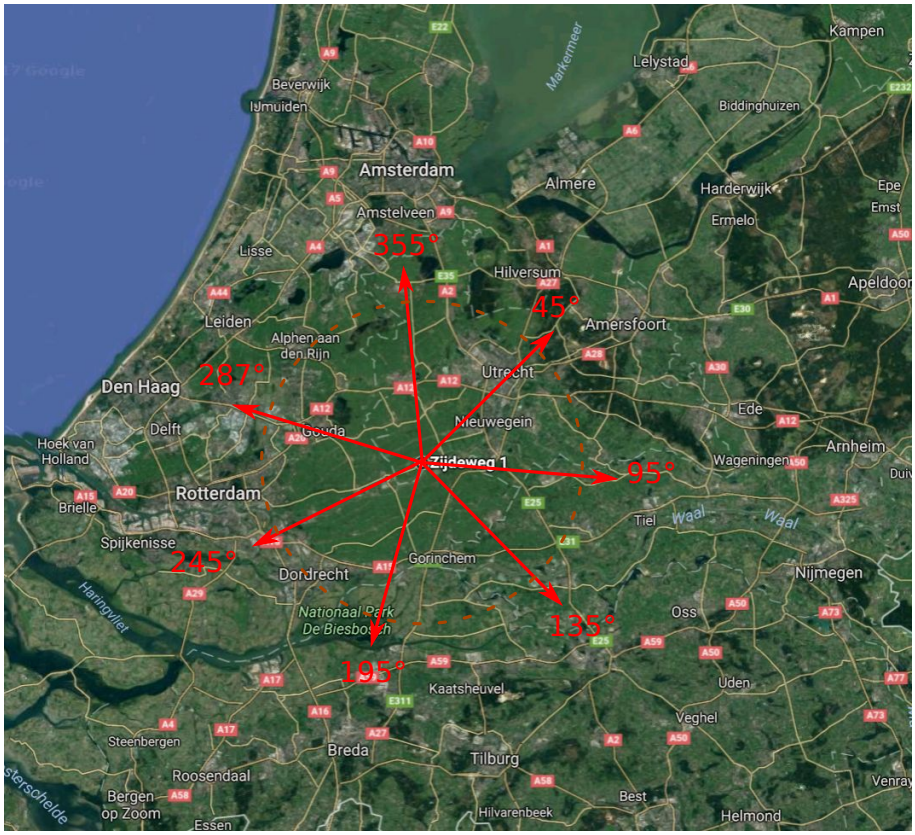

Figure 8.15: Azimuth angles of the measurement protocol mapped onto a satellite image.

Wavelength range	425-490 nm
Fraunhofer reference spectra	Noon zenith spectra averaged between 11:30 and 11:40 UT
Cross-sections:	
NO_2 (298K)	Vandaele et al. (1998) with I_0 correction (SCD of 10^{17} molecules/cm^2)
NO_2(220K)	Pre-orthogonalized Vandaele et al. (1998) with I_0 correction (SCD of 10^{17} molecules/cm^2)
O_3(223K)	Serdyuchenko et al. (2014) with I_0 correction (SCD of 10^{17} molecules/cm^2)
O_4(293K)	Thalman and Volkamer (2013)
H_2O	HITEMP (Rothman et al., 2010)
Ring	RING_QDOAS_SAO2010
Polynomial degree	Order 5 (6 coefficients)
Intensity off-set	Constant

Table 8.1: DOAS settings for NO_2 and O_4 [16].

9. Discussion of results

In the following sections the results of the measurements during the CINDI-2 campaign are discussed. First, the measurements included in the official intercomparison are compared to the Bremen MAX-DOAS measurements which is a well developed instrument. It did several good intercomparisons (i. e. during the first CINDI campaign it was selected as one of the reference instruments).

In the second part, the hemispheric scans are analysed. After a short statistical analysis, the hemispheric scans will be compared to wind data.

9.1. Comparison with the Bremen MAX-DOAS instrument

For the official intercomparison all instruments were pointing to the main azimuth direction of 287° (from North). For the elevation angles, the non-imaging instruments needed to scan the angles separately, while IMPACT measured all of them simultaneously. The scan ended with the zenith sky measurement, for which IMPACT also needed to move.

This leads to Figure 9.1. It shows two example sequences on the 19th of September 2016 at noon (a) and in the evening (b). The small dots are simultaneously taken measurements of IMPACT, while the large dots are the measurements for each elevation angle of the Bremen MAX-DOAS.

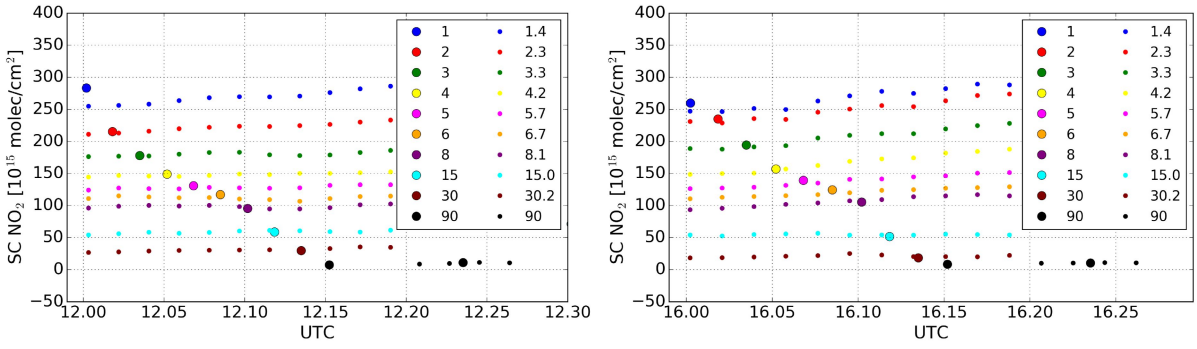

(a) 19.09.2016, noon

(b) 19.09.2016, evening

Figure 9.1: Comparison SC NO_2 of the Bremen MAX-DOAS (big dots) and IMPACT (small dots).

IMPACT's elevation angles can not be adjusted exactly to the needed angles due to the imaging-elevation characteristics. Therefore the elevation angles do not correspond exactly, which explains the majority of differences in measured the NO_2 slant column. However, the overall comparison is excellent. All measurements of IMPACT are close

the results of the MAX-DOAS. Most pronounced is the disagreement in 1° which is because the imaging instrument points actually in 1.4°. As the gradient of NO_2 is largest close to the ground, the lower elevations are the most sensitive to misalignment. Therefore the measured NO_2 slant columns in 1.4° are roughly the mean of 1° and 2° of the MAX-DOAS.

Differences can also be caused by the larger field of view. This can influence the elevation angle of 1° the most, as it is possible that ground effects interfere.

A deeper analysis for each elevation angle and each day is done in the next section with regression plots in more detail.

Figure 9.1 demonstrates the advantage of an imaging instrument. While the MAX-DOAS needs to scan each elevation angles individually, IMPACT observes all elevation angles simultaneously for the whole time of the MAX-DOAS scanning sequence. This leads to a much better temporal resolution and the possibility to detect variations of the NO_2. The increasing NO_2 during the sequence is nicely visible in the IMPACT data, while it is not in the MAX-DOAS data. This will lead to uncertainties in profiles retrieved by from MAX-DOAS data.

In Figure 9.2 the NO_2 SCs are plotted for the whole day (19.09.2016) for four different elevation angles.

The NO_2 SCs for the 1.4° of IMPACT have a mean value of the 1° and 2° of the MAX-DOAS for nearly the whole day. Except for two data points of the MAX-DOAS around 14 UTC, which are clearly lower then the rest of the points. This could be caused by something or someone blocking the view of the Bremen MAX-DOAS instrument.

The comparison of the other three elevation angles look very good for all sequences. As the imaging instrument has several data points for one datapoint of the MAX-DOAS and the variance of the NO_2 is clearly visible in Figure 9.1, only the IMPACT measurements closest in time are compared in the next section.

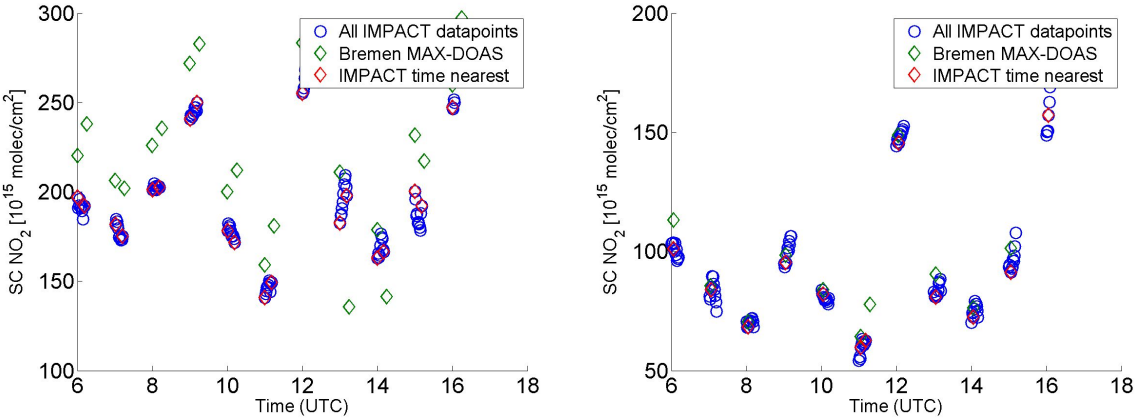

(a) Elevation 1°

(b) Elevation 4°

(c) Elevation 15°

(d) Elevation 90°

Figure 9.2: Comparison NO_2 slant columns of the Bremen MAX-DOAS and IMPACT.

9.1.1. Regression plots for the 19.09.2016

Figure 9.3 shows regression plots for all elevation angles for the 19th of September 2016. Plotted are the closest NO_2 SCs of IMPACT vs. the MAX-DOAS NO_2 SCs. The calculated errors of the linear fit result from the 95% confident bounds.

Consistently to the misalignment of the 1° elevation (1.4°) the offset of the linear fit is the largest and the correlation coefficient is the worst, which was therefore to be expected. This regression plot shows of a lot of scattering and the expected underestimation of IMPACT. This will be the case for all days, but nevertheless the plots are still done and the correlation coefficient and slope still calculated but the misalignment must be considered.

There are two more elevation angles showing a lot of scattering (3° and 5°). The 3° and 5° elevation are in the range of the exchanged fibres, which could cause the large scattering. The overlap of the neighbouring fibres can disturb single measurements more or less due to varying conditions (e.g. strong gradient in the distribution of NO_2). For the 4° elevation the effect of the exchanged fibre pairs above and below seem to cancel each other out to some extent, as the 4° elevation shows very good results with less scattering.

All other elevations show really good comparisons with correlation coefficients of 0.981 to 0.998 and slopes in the range of 0.97-1.09.

The slopes of the majority of elevation angles are larger than 1 and the offset positive, meaning that IMPACT is underestimating the NO_2 SCs. This correlates to the fact, that all elevation angles of IMPACT are up to 0.7° larger than the compared elevations of the MAX-DOAS. With lower NO_2 SCs for higher elevations, this was to be expected, especially for the lower elevation angles, as there the gradient for NO_2 is higher.

The offset of the fit however is not as good as the slope or correlation coefficient. The mean of the offset is $5.3 \cdot 10^{15}$ molec/cm^2. The offset of the 4° elevation is $-8.4 \cdot 10^{15}$ molec/cm^2. This is quite large compared to usual offsets from the Bremen MAX-DOAS instrument of up to $0.2 \cdot 10^{15}$ molec/cm^2. This is the preliminary result of the first intercomparisons from the CINDI-2 campaign done by the referee K. Kreher.

This will be investigated in the following sections.

Figure 9.3: Comparison NO_2 slant columns of the Bremen MAX-DOAS and IMPACT for all elevation angles for the 19th of September 2016.

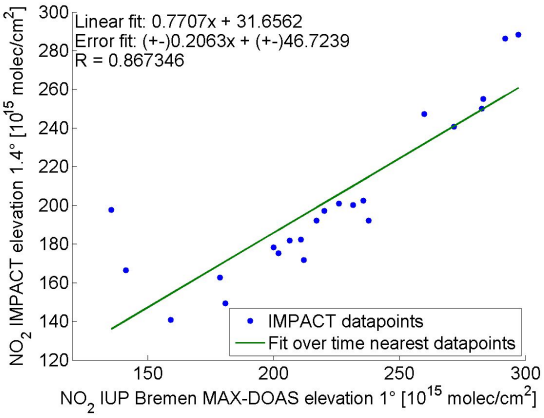

(a) Elevation 1°

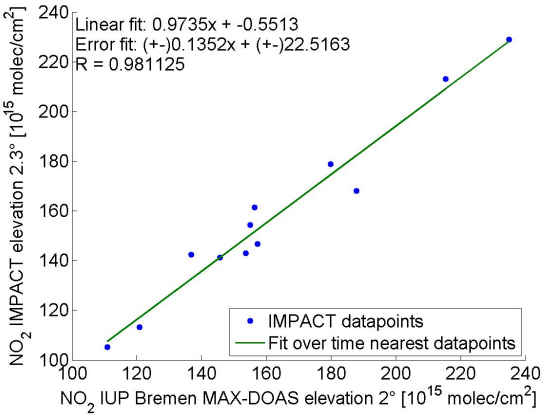

(b) Elevation 2°

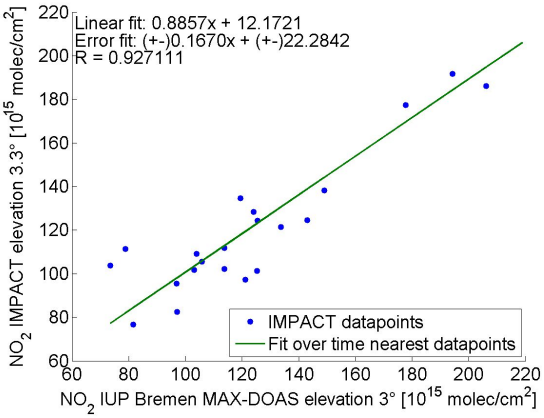

(c) Elevation 3°

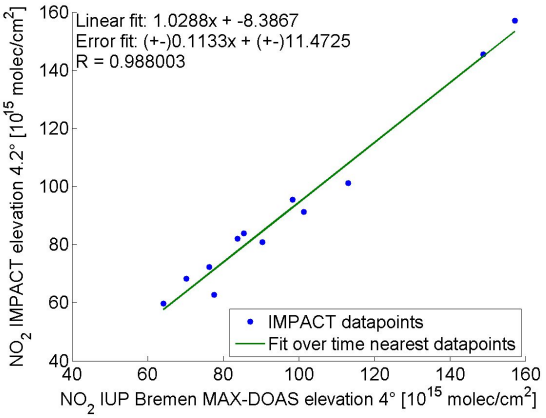

(d) Elevation 4°

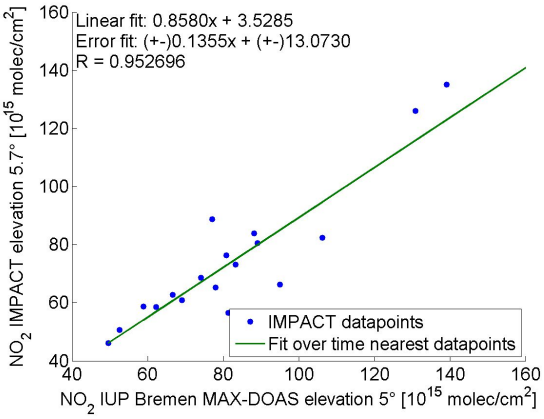

(e) Elevation 5°

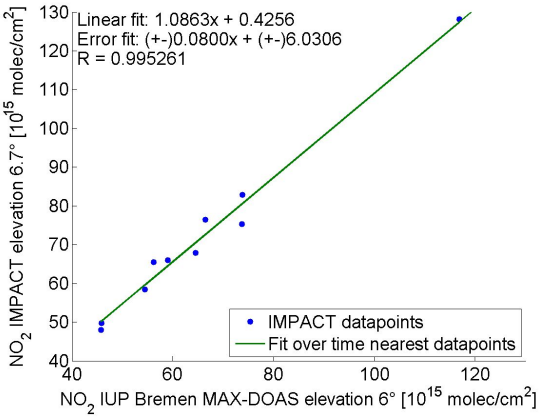

(f) Elevation 6°

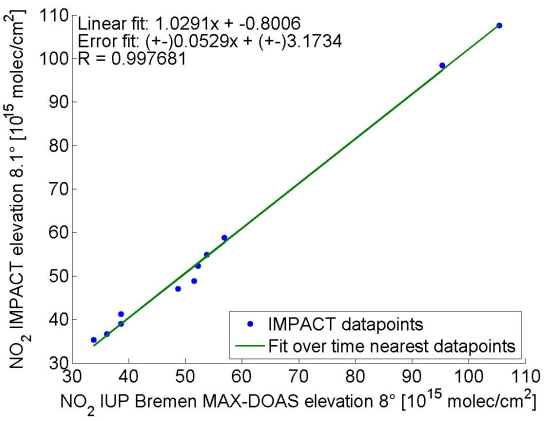

(g) Elevation 8°

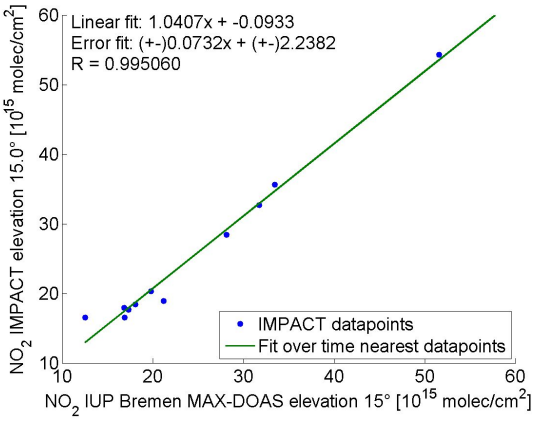

(h) Elevation 15°

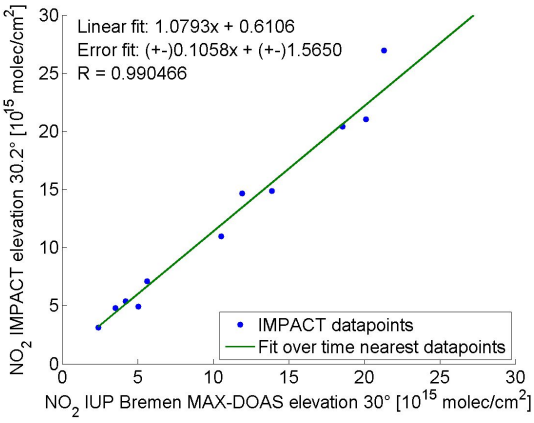

(i) Elevation 30°

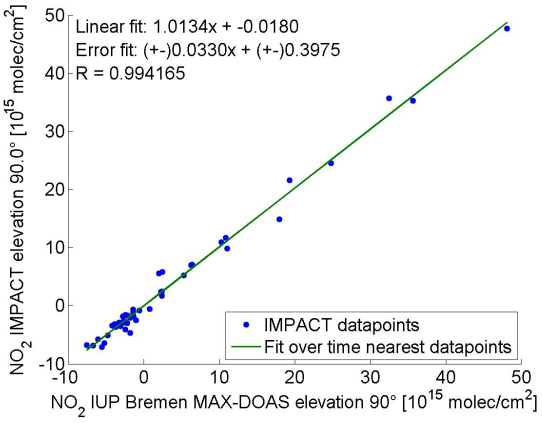

(j) Elevation 90°

9.1.2. Regression results for the whole campaign

The regression plots of the last section are repeated for all days of the campaign. The slope, offset, correlation coefficients and RMS for all elevation angles in dependence of the campaign days in September 2016 are plotted in Figure 9.4. The plotted errors (for slope and offset) result from the linear fit and its 95% confident bounds. The corresponding values (slope, offset and correlation coefficient) for the plots are also listed in the three tables A.2, A.3 and A.4 in the appendix.

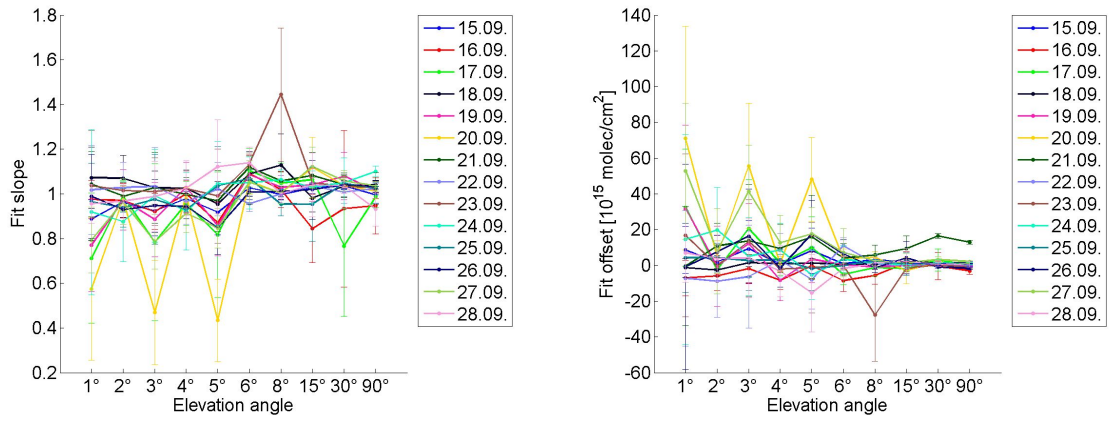

(k) Slope

(l) Offset

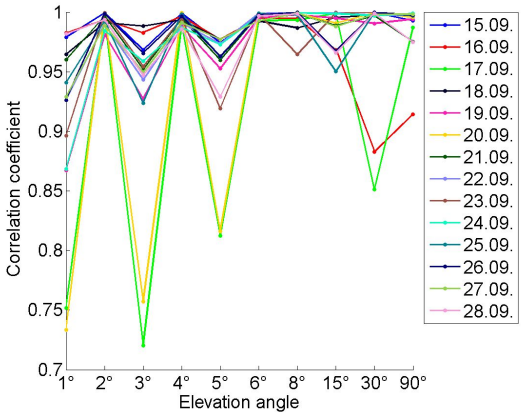

(m) Correlation Coefficient

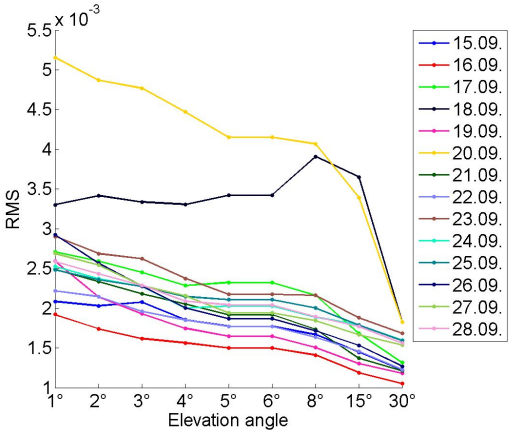

(n) RMS

Figure 9.4: Correlation coefficient, slope, offset and mean RMS for the whole campaign.

The results achieved in the previous chapter for the 19th September are similar to these from the other days.

Correlation Coefficient

As expected the correlation coefficients are worst for 1°, 3° and 5°. The reasons are the misalignment and the wrongly sorted fibres. Excluding the 1° elevation, some days showed also good correlation coefficients for the 3° and 5° elevation. For example the 15th and 26th show correlation coefficients of around 0.966. With regard to the slight misalignment (3.3° and 5.7°) and the wrongly sorted fibres, this is a very good comparison.

The other elevations, which are undisturbed by the wrongly sorted fibres have correlation coefficients up to nearly 1 for several elevations on several days. On the 15th of September the mean over all elevations (1.4° included) show a correlation coefficient of 0.991.

Also there were days with a slightly worse correlation, for example the 17th of September. On this day the weather was quite cloudy, which could explain the differences, as clouds and scatter effects influence the instruments differently due to the larger field of view of IMPACT.

Slope and Offset

The slope and offset shows some scatter over the whole campaign, with slopes between 0.8 and 1.1 for the majority of elevation angles and days. Only a few exceptions are not as good with slopes around 0.6 and 1.2. The mean value for all days and elevation show a slope of 0.99, meaning that the scattering around 1 nearly cancels out.

The offset is quite large and scatters with values between $-10 \cdot 10^{15}$ molec/cm^2 and $+20 \cdot 10^{15}$ molec/cm^2.

The errors (95% confidence bounds) are plotted and show a quite large extent. The reason is, that only a small number of measurements are compared per day, leading to a bad statistic.

To achieve better statistics, the regression plots are repeated for every elevation angle individually, but with all campaign days included in one plot. This will be discussed in the next section.

RMS

The RMS shows an expected behaviour. It is largest for small elevation angles and decreases for increasing elevation. The reasons for higher RMS in the lower elevation angles are the larger slant columns of all tropospheric gases (e.g H_2O etc), so that errors

as cross-section dependency on temperature (which is neglected in the DOAS-method, see sec. 4.1) have more impact, resulting in larger RMS.

The days 18th and 20th of September show significantly larger RMS. For all other days the RMS ranges between 1 and $3{\cdot}10^{-3}$. This is one order of magnitude larger than usual Bremen MAX-DOAS results. However, this was to be expected, as the signal to noise ratio is worse for IMPACT due to the used filter strongly reducing the incoming light and the smaller amount of pixels binned. The 90° elevation (zenith) is not included in the plot, as the RMS needs to be calculated differently for this elevation. For the zenith sky measurements the whole CCD is used and all viewing directions are binned. Therefore the RMS is differently compared to non-zenith viewing directions, where only small regions of the CCD are binned.

Intermediate conclusion

In summary the comparison looks excellent with only a few correlation coefficients < 0.9. However, there were days with better agreement and days with worse agreement. There was some scattering of slope and offset during the campaign. The resulting errors are large, because of the small number of compared measurements. Further investigation is done in the next section. The RMS is as large as expected.

9.1.3. Regression results per elevation angles for all days combined

The following subplots in Figure 9.5 combine all campaign days into one regression plot per elevation angle. The improvements are significant. The fit errors for the slope decrease from $\sim 10\%$ to $\sim 1.5\%$ for all elevation angles, including 1.4° , 3.3° and 5.7°. Also the scattering decreases clearly. The data points all agree very well on the fit line. Exceptions are a few points at 30° and 90°. These correspond to a day, at which there is a constant overestimation by IMPACT.

Figure 9.5: Comparison of NO_2 slant columns of the Bremen MAX-DOAS and IMPACT for all elevation angles including all days.

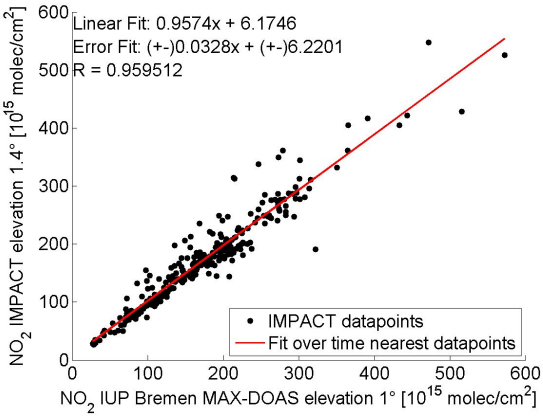

(a) Elevation 1°

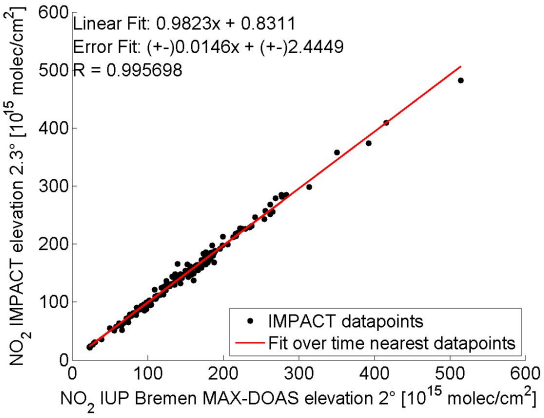

(b) Elevation 2°

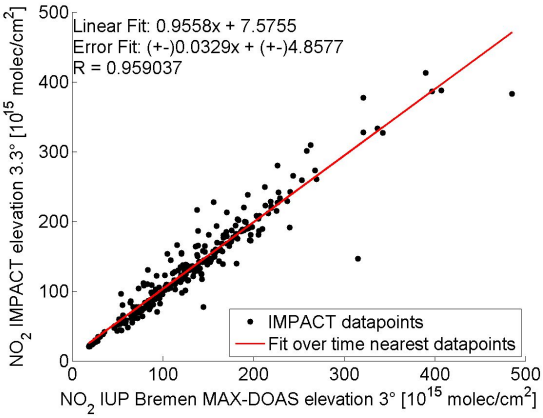

(c) Elevation 3°

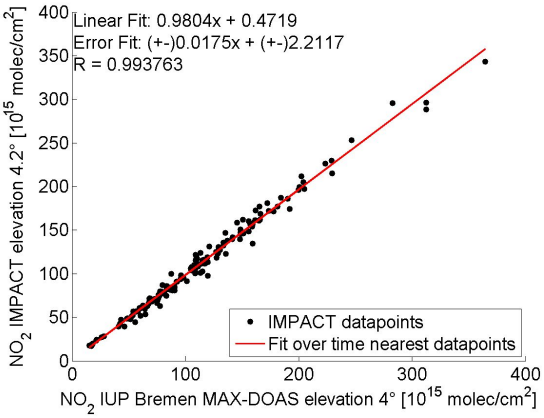

(d) Elevation 4°

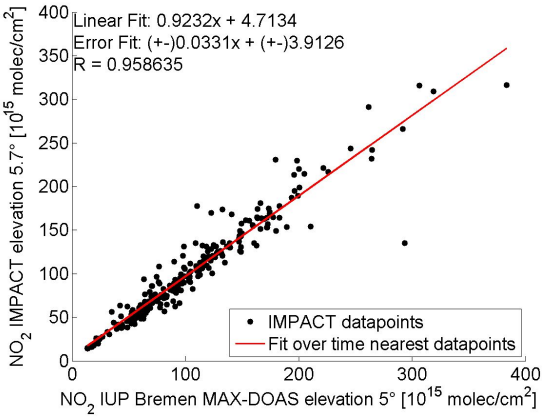

(e) Elevation 5°

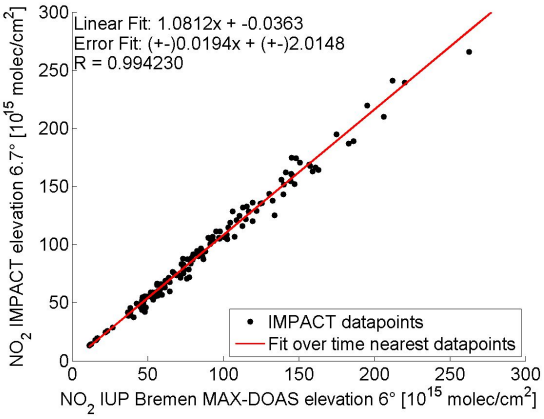

(f) Elevation 6°

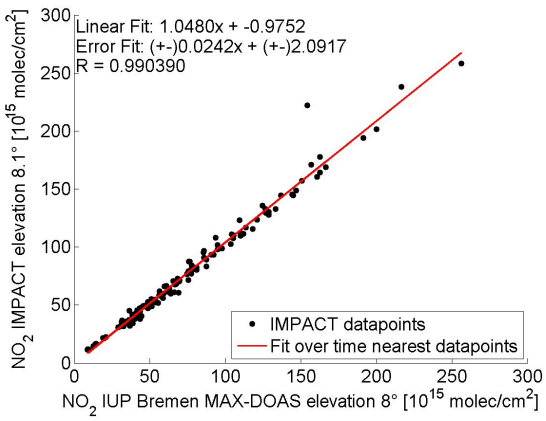

(g) Elevation 8°

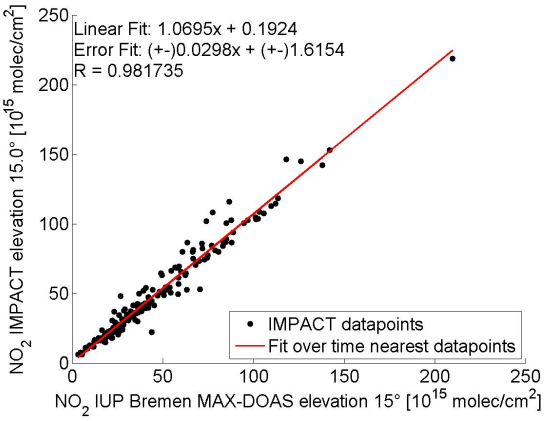

(h) Elevation 15°

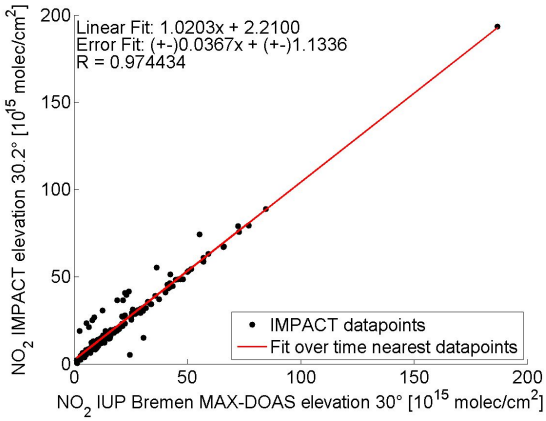

(i) Elevation 30°

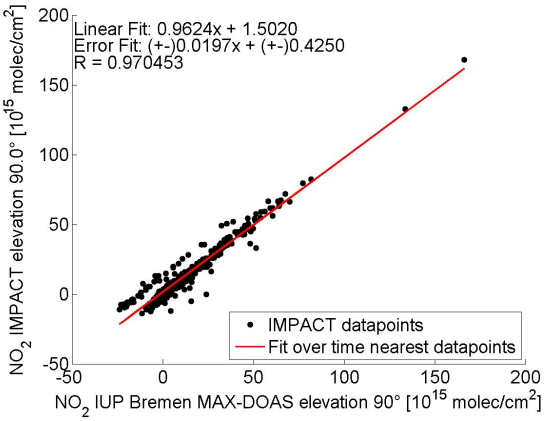

(j) Elevation 90°

The slopes and the offsets are plotted as a function of elevation angle (for a better overview) in Figure 9.6 and the values are listed in Table A.5 in the appendix. The optimal result with a slope of 1 and an offset of 0 is indicated by black lines. Compared to the plot in Figure 9.4, where every single day had its own plot, the range of scattering and the errors of the fit reduced a lot. The slopes are in range of 0.9-1.1 and the mean of the slopes over all elevation angles is 1. In terms of slope the comparison of the MAX-DOAS and IMPACT is therefore excellent. Some variations were to be expected, due to a larger field of view, pointing and worse signal to noise ratio.

The offset reduced by one order of magnitude. For the elevation angles 1.4° , 3.3° and 5.7° the offset is improved to under $10{\cdot}10^{15}$ molec/cm^2. As these elevations are impacted by misalignment (1.4°) and the exchanged fibres (3.3° and 5.7°) this is a very good result.

All other elevations show offsets better than -1 to $1{\cdot}10^{15}$ molec/cm^2 . The improvement of the offset by fitting all campaign days is therefore significant. The most probable explanation is the low signal to noise ratio. The small binning range and the strong filter lead to a low SNR. This results in noise, which effects strongly the single days comparison. Therefore the bad statistic due to the limited set of datapoints when evaluating single days is improved. Even if the offset is still one order of magnitude larger than for other MAX-DOAS comparisons, for a comparison to an imaging instrument this result is very good.

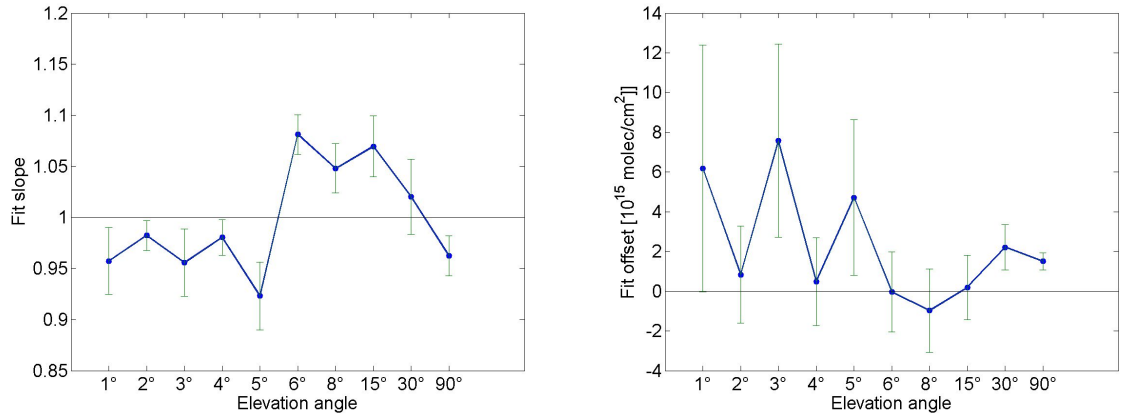

(k) Slope (l) Offset

Figure 9.6: Slope and offset for the whole whole campaign days combined for each elevation.

Conclusion

In conclusion, the comparison of the MAX-DOAS instrument and IMPACT is excellent, but the signal to noise ratio could be improved by using an optimal filter, aiming at more incoming light.

Additionally the light fibre needs to be corrected, as the exchanged fibres influence the measurements a lot and lead to unnecessary scattering. Therefore, the comparison of lower elevation angles is effected and need to be regarded with caution.

9.2. Analysis of hemispheric scans

The hemispheric scans were performed between the sequences of the intercomparison protocol. The azimuthal scans with a stepsize of 10° have a total duration of around 13 minutes plus the duration of the zenith sky reference measurement. This results in a time difference of roughly 15 minutes between two complete scans.

A statistical analysis investigating the variability of NO_2 for the campaign is presented in the following. Afterwards, the variability of NO_2 on a daily and a minute/hourly scale is investigated in more detail for the 19th of September, as this day showed large variability in the lowest elevation angles. This will be investigated in more detail with respect to wind direction measurements.

9.2.1. Statistical analysis

As a first step the daily mean SC NO_2 azimuthal scan was calculated from all measured scans on that day. From this results a daily mean scan, from which a minimum, maximum and mean value of NO_2 (horizon excluded) per day was calculated. These values are listed in Table 9.1 and plotted in Figure 9.7.

The days were quite different in NO_2 amount. On the weekend, especially the Sundays, the values are clearly lower. This is expected as traffic is much less during the weekend.

On Mondays, the amount of NO_2 is one of the highest. This is probably due to weekend commuter and starting the working days. The rest of the weekdays, the NO_2 is highly variable with minima and maxima variation of up to 100% from day to day. One some days with nearly equal mean values, the maximum values can vary quite a lot (e.g. 19th to 20th).

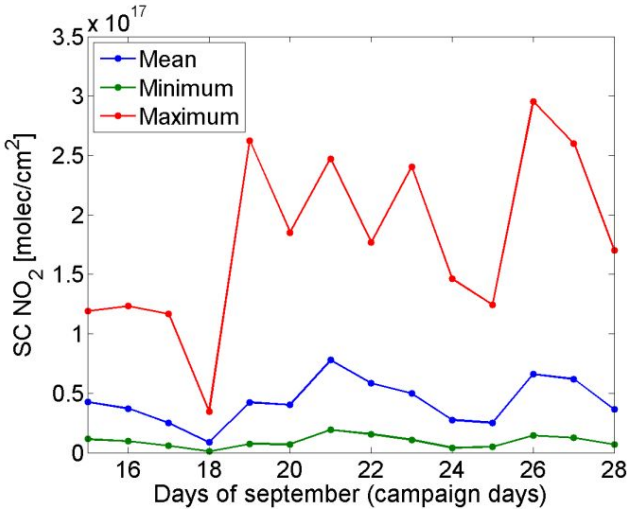

Figure 9.7: Mean, minima and maxima of mean SC NO_2 per day.

Day	Weekday	mean	min	max
15	Thu	4.3	1.5	11.9
16	Fri	3.7	1.2	12.3
17	Sat	2.5	0.8	11.7
18	Sun	0.9	0.3	3.4
19	Mon	4.2	0.9	26.3
20	Tues	4.0	1.4	18.5
21	Wed	7.8	2.4	24.7
22	Thu	5.8	1.8	17.7
23	Fri	5.0	1.4	24.0
24	Sat	2.8	0.9	14.6
25	Sun	2.5	1.0	12.4
26	Mon	6.6	2.0	29.5
27	Tues	6.2	1.7	26.0
28	Wed	3.6	1.1	17.0

Table 9.1: Mean, minima and maxima of mean SC NO_2 per day in unit of 10^{16} molec/cm^2.

9.2.2. Obstacles in the field of view (FOV)

For the hemispheric scan, some obstacles were inside the field of view. This can be seen in Figure 9.8. The upper picture shows a panorama image, made with a digital camera. In the lower plot, all campaign days (14 days in total) are averaged to one hemispheric scan. The hemispheric scan is plotted in dependence of azimuth and elevation angle. This results in a very smooth distribution of NO_2. Three obstacles are obvious:

- -115°: The single tree in that direction is exactly in the field of view.
- -15° to -25°: The other telescopes on the container are sometimes in the field of view (especially when they point perpendicular to the imaging instruments viewing direction).
- 85° to 135°: High trees obstruct the lower elevations.

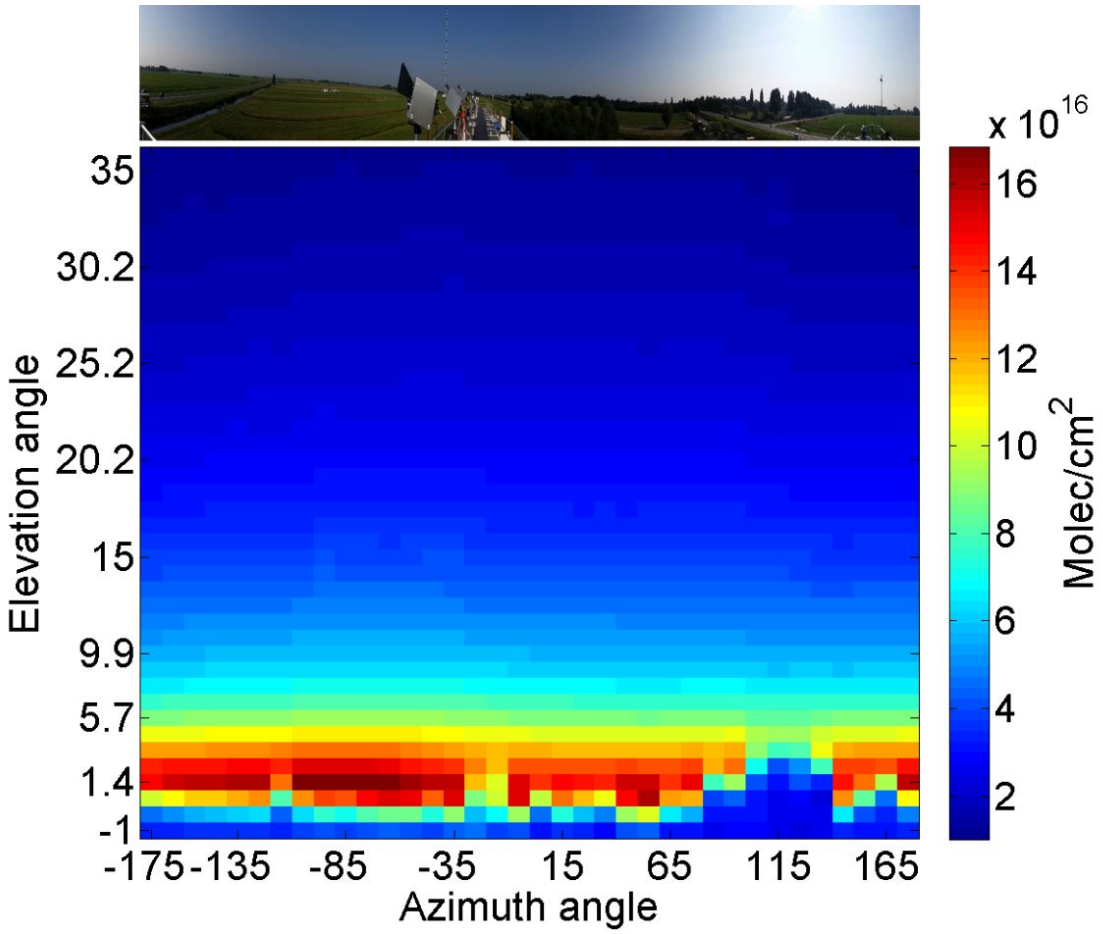

Figure 9.8: Panorama picture and campaign mean hemispheric scan.

9.2.3. Variability of NO_2 in the hemispheric scans

Day-to-day variability

The day-to-day variability of NO_2 was investigated in more detail using the days from the 18th to the 21st of September, as these days show quite different mean and maximum values for NO_2 (Table 9.1). Figure 9.9 shows the daily mean hemispheric scans for these days. The color bar scale for the NO_2 is the same for all four days.

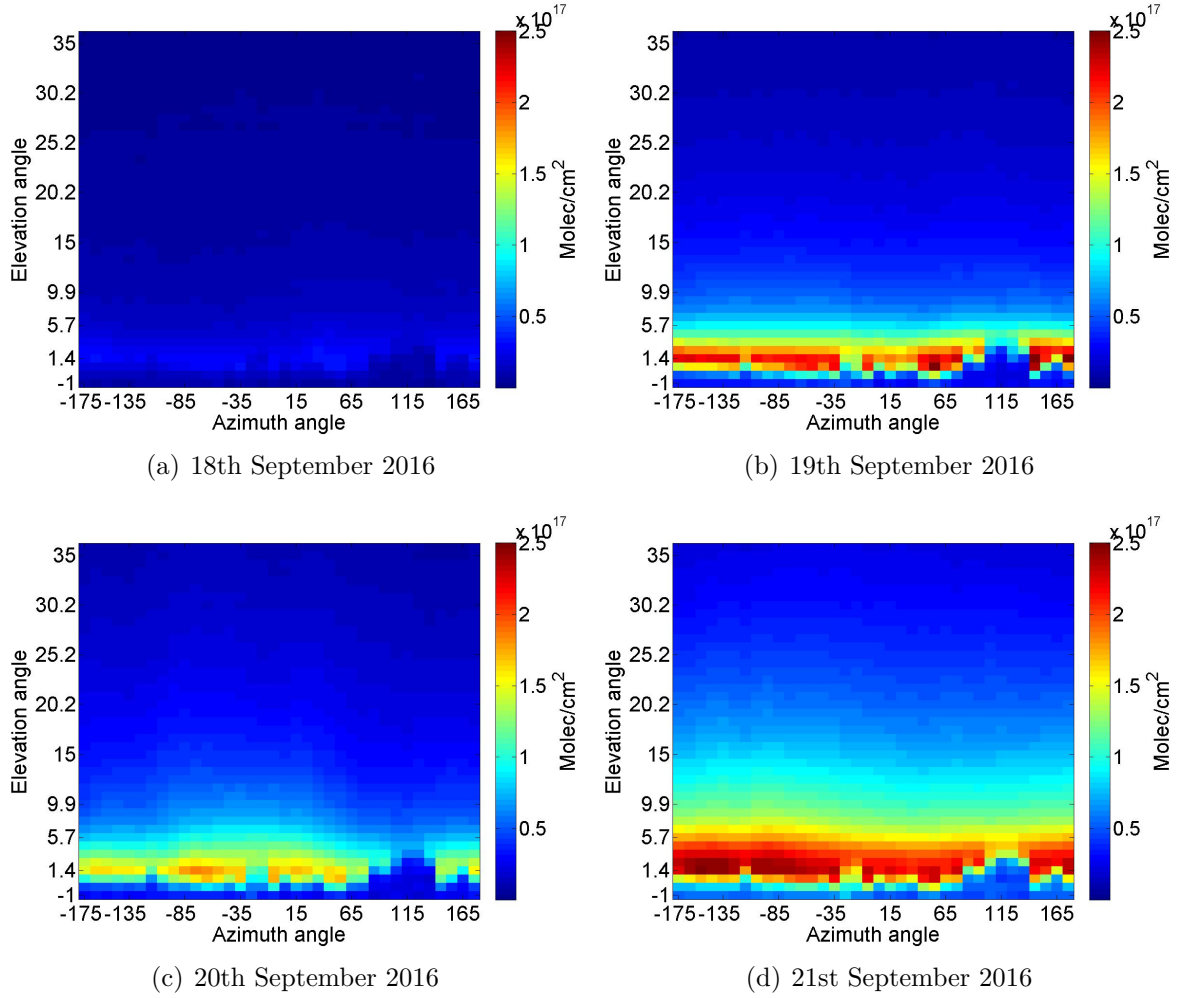

(a) 18th September 2016

(b) 19th September 2016

(c) 20th September 2016

(d) 21st September 2016

Figure 9.9: Mean of SC NO_2 for 4 days during the campaign.

The 18th of September is a Sunday with a lot less NO_2. On the 21st of September, the amount of NO_2 is one of the largest during the campaign (up to $2.5 \cdot 10^{17}$ molec/cm^2).

The distribution of NO_2 changes significantly from day to day. While the NO_2 gets less for the lower to the higher elevation angles it is dependent on its amount.
On the 21st the NO_2 is transported in higher elevation angles, whereas on the 19th,

it stays in the lower elevations. However the quantity is the slant column, which is depended on the light path, so that this needs to be proofed by a profile using the vertical columns.

One additional difference is the azimuthal distribution. While the 19th has a smooth distribution, the 20th has its maximum at -85° to 65° and the 21st shows large NO_2 at -175° to -75°.

For the same days, the Figure 9.10 shows the corresponding standard deviation. The standard deviation has the same shape as the mean. The strongest standard deviations correspond to highest NO_2 values, which is of no surprise. Larger standard deviations can also be seen in the range of -15° to -15°, which correspond to the MAX-DOAS instruments being sometimes in the field of view.

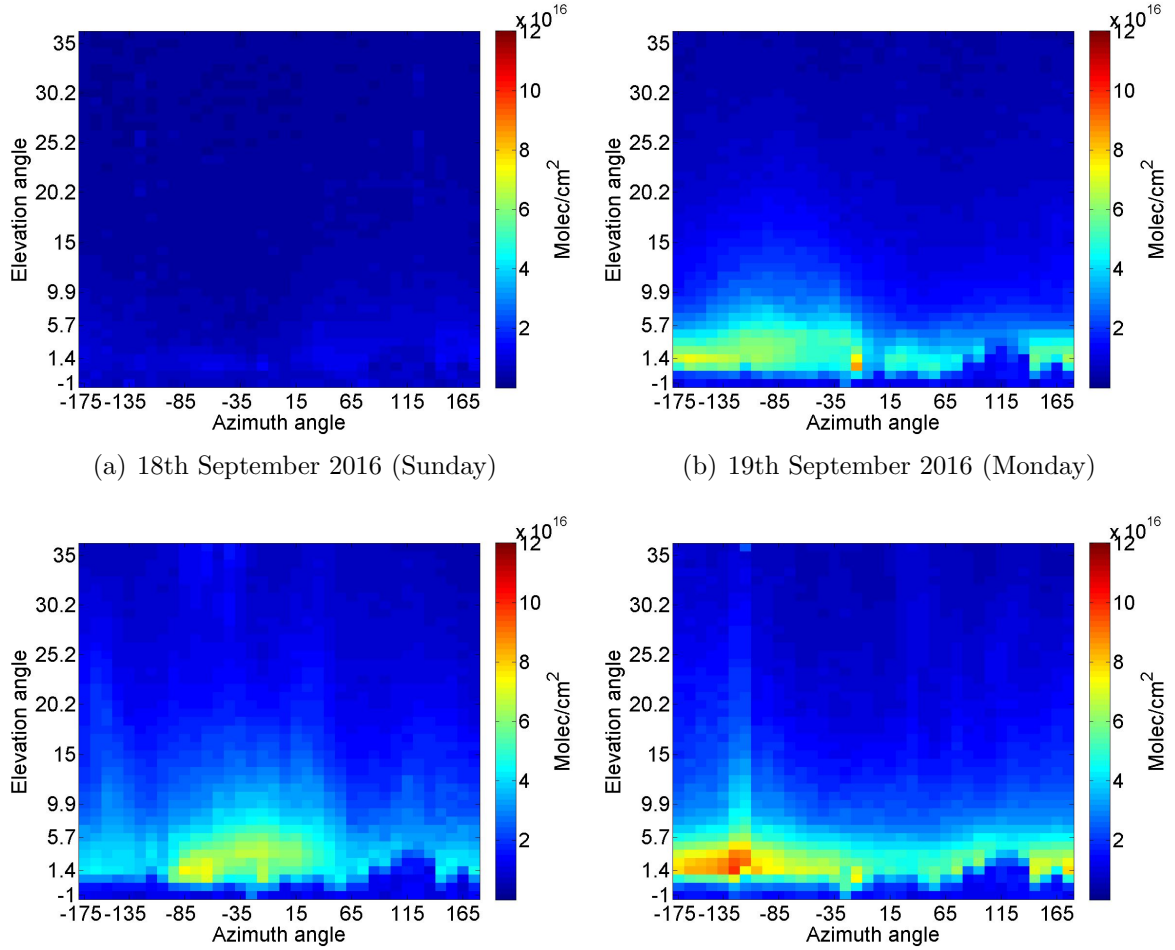

(a) 18th September 2016 (Sunday)

(b) 19th September 2016 (Monday)

(c) 20th September 2016 (Tuesday)

(d) 21st September 2016 (Wednesday)

Figure 9.10: Std of SC NO_2 for 4 days during the campaign.

Minute/hourly variance

The advantage of the imaging instrument is the high temporal resolution. Therefore Figure 9.11 shows single scans measured on the 19th of September (all subplots have the same color bar scale). The time difference between (a) and (b) is roughly 15 minutes. These are consecutive scans. (b) to (c) however have a difference of roughly 1 hour, and (c) to (d) around 30 minutes.

The variability of NO_2 is huge. At 12:38 UTC strong NO_2 values were measured around -175° most likely caused by traffic on a close by road. Not even one hour later there is much less NO_2, probably due to OH-reduction. It decreased from $4{\cdot}10^{17}$ molec/cm^2 to $1.3{\cdot}10^{17}$ molec/cm^2. Also in the azimuthal direction a fast variability is observed. At 13:22 UTC the maximum is around -35° to -85°, which seems to travel to 65° at 13:50 UTC. Wind measurements were performed during the campaign and provided from the Cabauw Experimental Site for Atmospheric Research Observatory (CESAR). On the 19th of September, a mean wind direction of 11° was measured, which corresponds to the travel of the NO_2 from south to north.

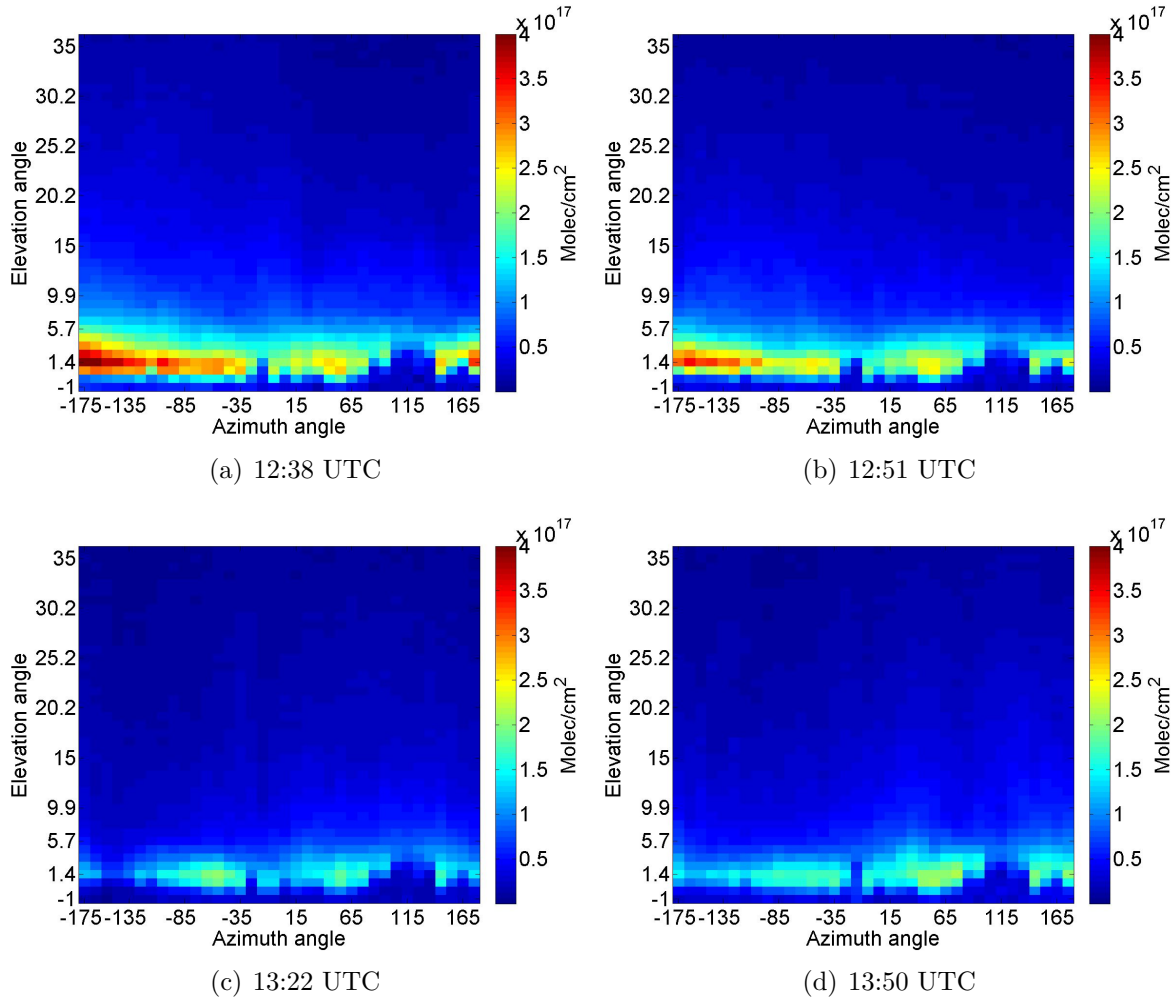

(a) 12:38 UTC

(b) 12:51 UTC

(c) 13:22 UTC

(d) 13:50 UTC

Figure 9.11: Single hemispheric scans of NO_2 measured on the 19th of September.

9.2.4. Analysis of the variability of NO_2 in the lower elevation angles

The observed large variability in time and space suggests a deeper investigation. Therefore, an analysis of one of the lower elevation angles is done. By concentrating on the 2.3° elevation, it is possible to plot the NO_2 distribution (in this elevation angle) in dependence of azimuth angle and time (Figure 9.12). In Figure 9.12 also 2 of the obstacles are visible: the MAX-DOAS instruments (-15° to -25°) and the high trees (85° to 135°). The single tree is below the 2.3° elevation angle. Also some single measurement pixels (e.g. on 23rd) show very low NO_2. For these cases something was most likely blocking the view, e.g. working scientists, passing people.

While some days do not show interesting plumes but large scattered distribution of NO_2 (17th, 22nd, 24th), there are some very interesting events visible on other days. In general, there are two types of events: temporal events and spatial events.

On the 19th of September for example two temporal events occur: the first from 9:30 to 10:30 UTC and the second from 11:45 to 12:30 UTC. While the spatial extent is very large it only covers a time frame of one hour. So, two large NO_2 plumes travelled over the measurement site. On the 21st there are even shorter events from 11 to 14 UTC which are only visible for one or two consecutive scans.

The spatial events occur i.e. on the 23rd and 25th and have only a small spatial extent of significantly larger NO_2. On the 25th in the evening, the large NO_2 amount is only measurable in two azimuth angles (-105° and -95°). A 1D DOAS instrument measuring in a fixed azimuth direction of e.g. $\sim 180°$ (difference of only 75°) would have completely missed the event.

Figure 9.12: NO_2 measured in elevation of 2.3° as function on azimuth angle and time for all campaign days (15-28/a-n).

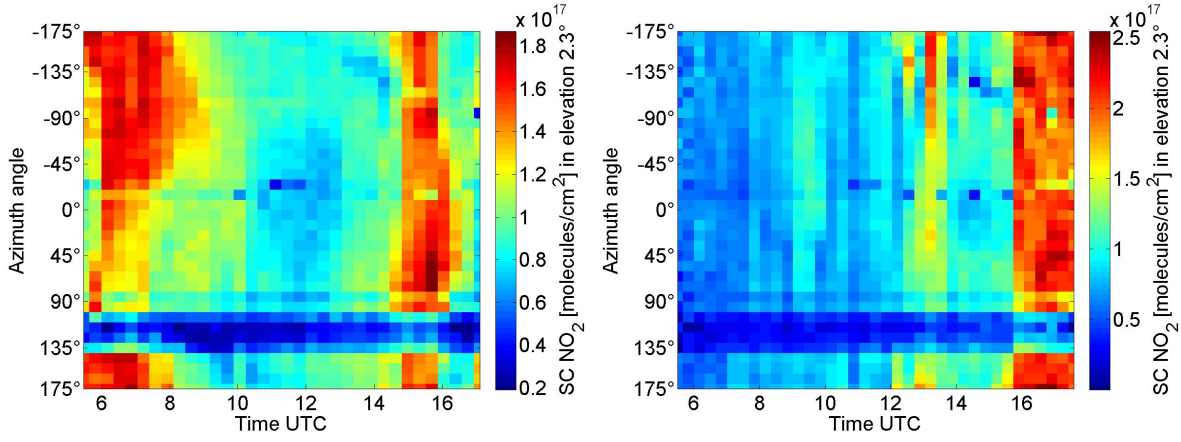

(a) 15th of September (Thursday)

(b) 16th of September (Friday)

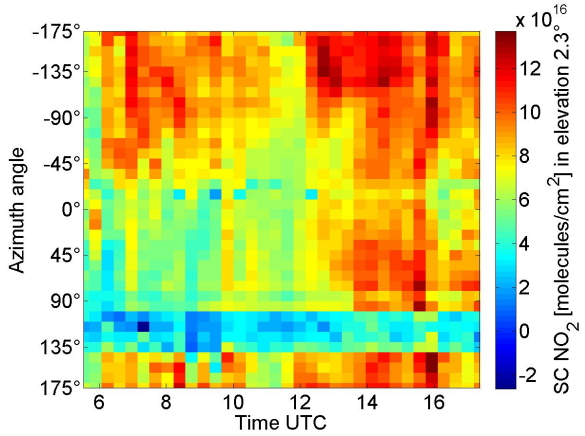

(c) 17th of September (Saturday)

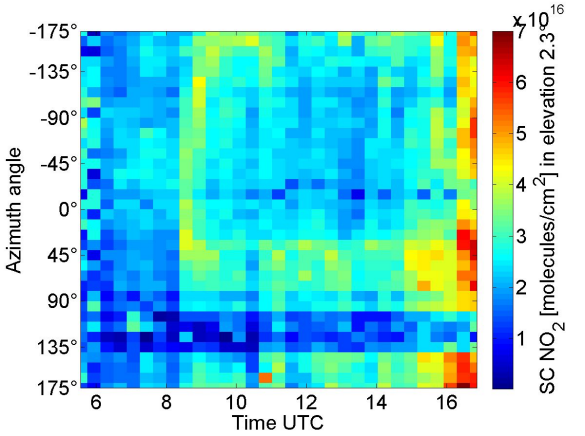

(d) 18th of September (Sunday)

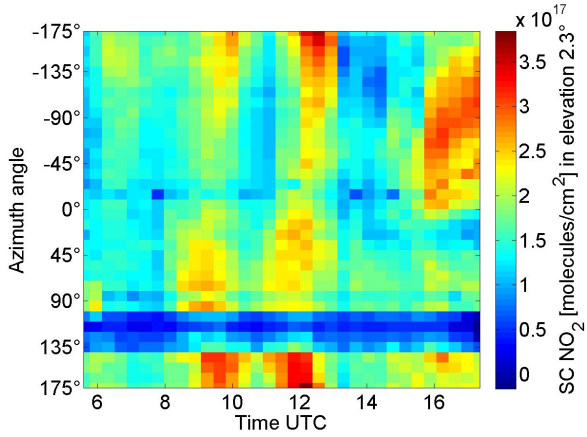

(e) 19th of September (Monday)

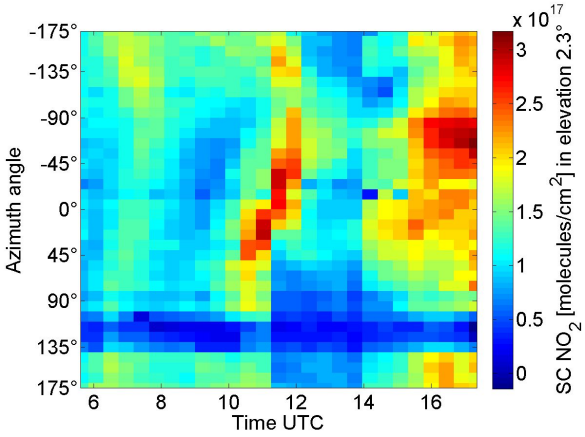

(f) 20th of September (Tuesday)

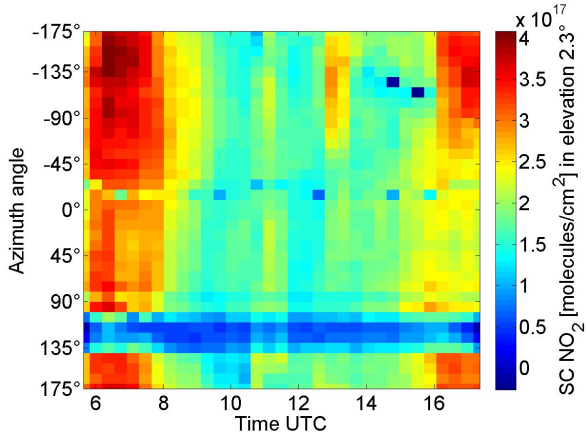

(g) 21st of September (Wednesday)

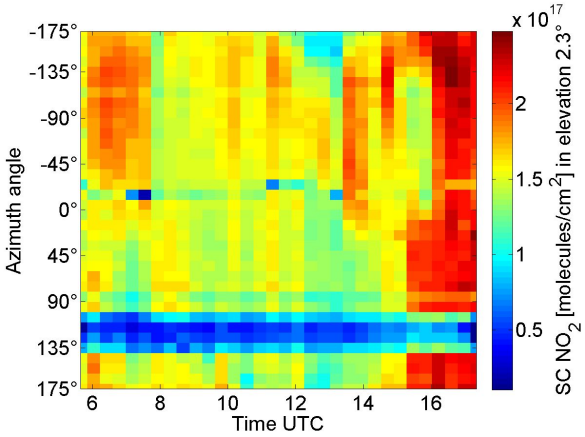

(h) 22nd of September (Thursday)

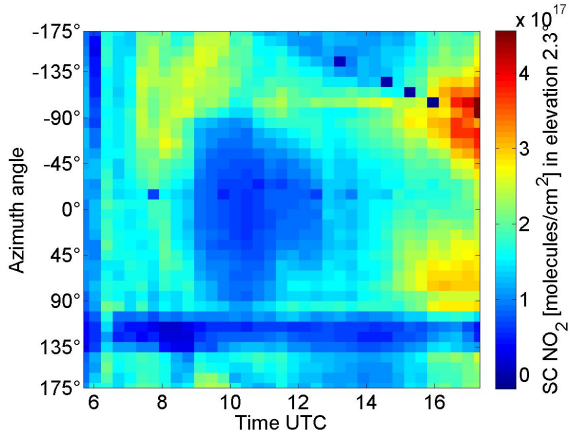

(i) 23rd of September(Friday)

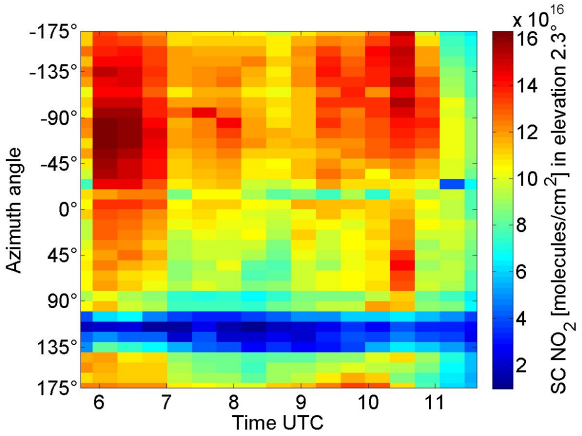

(j) 24th of September (Saturday)

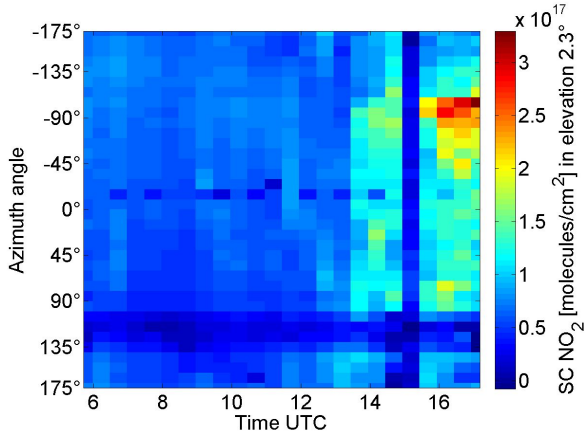

(k) 25th of September (Sunday)

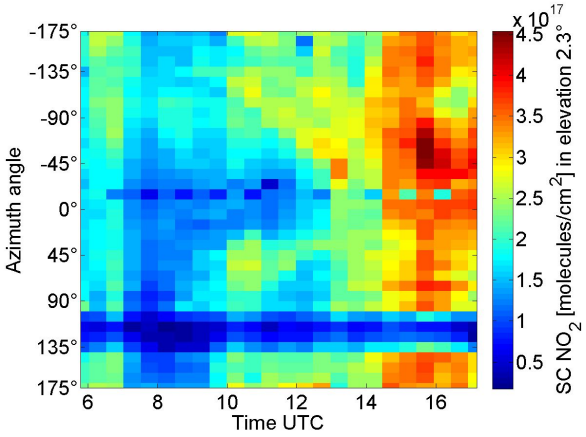

(l) 26th of September (Monday)

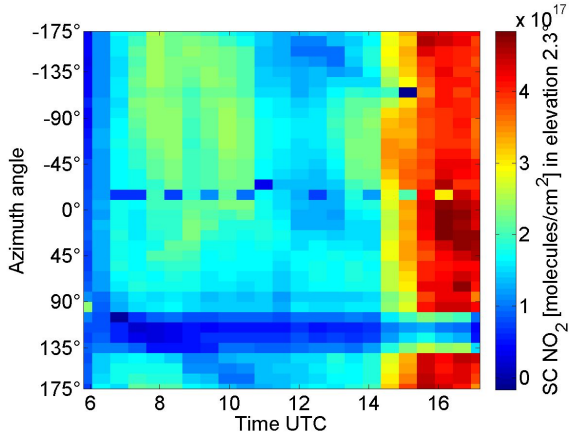

(m) 27th of September (Tuesday)

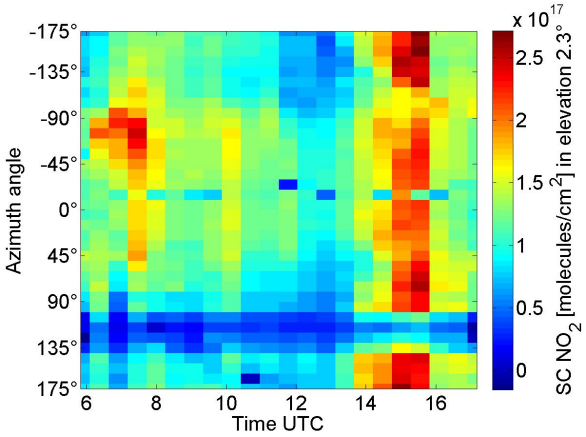

(n) 28th of September (Wednesday)

9.2.5. Comparison with wind measurements

One very interesting day was the 20th of September (Fig 9.12 (f)). On this day one very local event in time and space occurs. A NO_2 plume was measured only from 10:15 UTC to 12 UTC in only 45° to -90° azimuth angle. This example plume can be investigated by comparison to wind measurements. On the 20th of September there was a low mean wind speed and a mean wind direction from 54°. The wind direction is illustrated on a circle (see Figure 9.13(a)). When the wind is blowing from 54° it would blow plumes from 54° to -126°, which is seen in the measurements. The plume got into the field of view around 54° shortly after 10 UTC. It was then transported by wind on the western side of the instrument until it left the field of view at -90°.

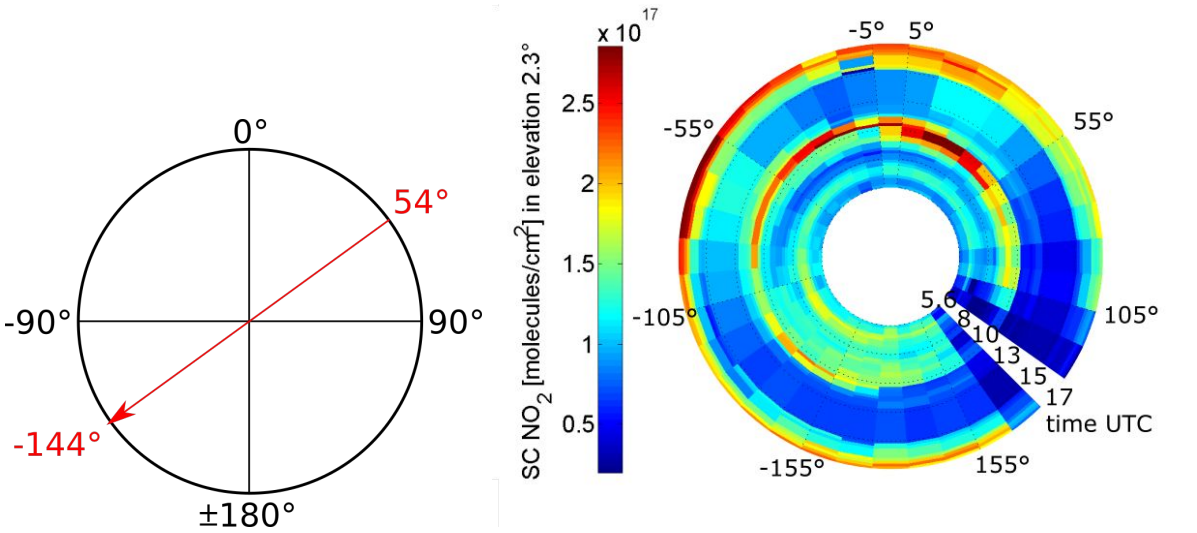

(o) Illustration of the wind direction (p) NO_2 variability in 2.3° elevation on the 20th September

Figure 9.13: Correlation of wind direction and NO_2 plume on the 20th September.

10. Summary, conclusions and outlook

Within this thesis a new imaging DOAS instrument called IMPACT was set-up and took part in its first campaign.

The imaging instrument IMPACT consist of three main parts: the receiving optics, connective optics and the spectrometer-detector-system. The receiving optics consists of a waterproofed telescope which includes an objective and a camera for scene documentation. The connective optics is a sorted quarzfibre, which transports the light collected by the objective to the spectrometer-detector-system. The system consists of an imaging spectrometer (Andor Shamrock SR303i-A) and a charge-coupled device (CCD, Andor Newton DU940P-BU). The combination of a sorted quarzfibre with an imaging spectrometer enables the system to preserve spatial information. Therefore the CCD measures several spectra simultaneously, which correspond to different viewing directions.

To get an optimal spatial and spectral resolution, the instrument needs to be adjusted. This was done in three steps. First, the CCD alignment to the spectrometer was adjusted. This determines primarily the spatial resolution. There were two possible ways to mount the CCD and the intermediate flange was chosen. It was the best choice as it provided a good compromise of spatial and spectral resolution.

The next step was the adjustment of the fibre to the spectrometer. The fibre needs to be placed in the optimal position bringing the desired wavelength region (DOAS fitting window) in the region of best spectral resolution at the CCD.

As a last step the adjustment of the fibre to the objective was done, which in the end defines the field of view. The end of the fibre is brought into the focal plane of the objective. This procedure is quite complex as special equipment (Theodolite) and two people are needed to do it properly.

After the adjustments the instrument was characterised, whereby four characteristics were investigated. The linearity of the CCD is crucial for the DOAS-method. The linearity proofed to be better than 99% (manufacturer's guarantee). Only the high sensitivity mode with the lowest amplifier of 1 electron per count showed some non-linearity of around 1.3%. Finally, the high sensitivity mode with an amplifier of 4 electrons per count was chosen for operation.

The second important characteristic is the dark signal of the CCD. It showed to be nearly independent on exposure time. Only some dependence on temperature could be seen and therefore a CCD temperature setting of -35°C was chosen.

The applied smear correction is an optional feature and only important for imaging instruments, which need to be darkened during readout. It corrects for light which is measured in the wrong viewing direction during the read-out without using a mechanical shutter.

The instrument response function was investigated as well. As the imaging instrument measures several spectra across the vertical axis (one per viewing direction), each is assigned to an own instrument response function. The changes of the function for the wavelength (horizontal) axis are however not yet considered. An analysis showed changes of 53%.

The first application was the CINDI-2 campaign. It took place in Cabauw, the Netherlands. In total 38 DOAS-like instruments participated. As there was only little time between first set-up of the instrument and start of the campaign, a lot of improvements were done on site. A filter was installed into the light path to prevent saturation. Some dark pixels of the CCD were excluded in the retrieval to reduce the residuals. A mix of two fibre pairs of the sorted quarzfibre was detected. Therefore the fibres needed to be exchanged, which was done by the manufacturer after the campaign. During CINDI-2, a software resorting of different regions on the CCD was performed correcting for the exchanged fibres.

In the beginning of the campaign a calibration measurement was done, which led to a lot of information about the characteristics of the spatial imaging and field of view of the instrument. With this measurement it was possible to calibrate elevation angles and pixel rows on the CCD.

After the improvements, the instrument took part in the official intercomparison of the CINDI-2 campaign. Therefore part of the measurement scheme was followed to compare to the other MAX-DOAS instruments. The remaining time was spend to do full hemispheric scans with a step size of 10° in azimuthal direction and a total vertical field of view from -5.1° to 35.8°. The duration of a scan including a zenith sky reference was 15 minutes.

The data analysis of the measurements of NO_2 during the CINDI-2 campaign consists of two parts: 1) Comparison to the Bremen MAX-DOAS instrument and 2) analysis of the hemispheric scans.

The comparison of the NO_2 slant columns to the Bremen MAX-DOAS instrument is in general excellent. However an interference of the mixed fibre pairs of the quarzfibre was visible. Unfortunately the pairs were in the lower elevation angles. Therefore the lower elevation angles showed large scattering and a worse agreement than the higher elevation angles. Especially the lowest elevation angle of 1.4° differed, which could be traced back to misalignment (1° compared to 1.4°) and possible ground interference due to a larger field of view of IMPACT. The higher elevation angles however showed a good comparison with slopes around 1. For all elevation angles the offset was quite high with values larger than the usual offsets for MAX-DOAS comparisons. An analysis of all measured campaign days combined, showed a large reduction of scattering and offset.

The last part focused on the hemispheric scans investigating the variability of NO_2. The NO_2 concentration varied a lot from day to day as well as from scan to scan (15 minutes time difference).

A more detailed analysis of the lower elevation angles was done, which highlighted the strong variability not only in time but also in space. One single day was further analysed, showing an example of a plume transported by wind over the measurement site.

As an outlook, a few things are recommended to be improved. The most important is the correction of the wrongly sorted fibre by the manufacturer (which has been already done). The second task is the improvement of the signal to noise ratio. During CINDI-2, a strong filter was applied in front of the instrument as saturation effects (blooming) of the CCD appeared to be a problem. However, a bug in the software smear correction was found to lead to unmarked saturated measurements. As the bug is fixed, the filter could be removed (or a weaker filter is recommended) leading to more light collected, which will therefore improve the signal to noise ratio. For further data analysis the slant columns of NO_2 can be converted to vertical columns with simulated air mass factors. With the simultaneously measured elevation angles, this would lead to an interesting profile retrieval.

For the instrument IMPACT more campaign applications are foreseen, the next one already in summer 2017 (AQABA).

A. Appendix

Figure A.1: Theodolite.

Table A.1: Overview about participating institutes, instruments and their location [15].

Institute	Country	Instruments	Range [nm]	Location
Static MAXDOAS systems				
AIOFM	China	2D-MAXDOAS	290-380	Top Level Ceasar Site
AMOIAP	Russia	2-port DOAS (1D)	420-490	Ground Level Ceasar Site
AUTH	Greece	Phaenthon mini MAXDOAS (2D)	297-452	Ground Level Ceasar Site
BIRA-IASB	Belgium	2D MAXDOAS	300-390/405-540	Top Level Ceasar Site
BLS	Belarus	catadioptric telescope / MARS-B (1D)	409-492	Ground Level Ceasar Site
BOKU-Met	Austria	1-channel MAXDOAS (2D)	406-579	Top Level Ceasar Site
CAMS	China	mini-DOAS Hoffmann UV (1D)	292-447	Ground Level Ceasar Site
CAMS	China	mini-DOAS Hoffmann Vis (1D)	399-712	Ground Level Ceasar Site
CEReS	Japan	1 channel MAXDOAS (1D)	310-515	Ground Level Ceasar Site
CSIC	Spain	MAXDOAS (1D)	300-500	Ground Level Ceasar Site
CU-Boulder	USA	3D-MAXDOAS	327-470/432-678	Top Level Ceasar Site
CU-Boulder	USA	ZS und MAXDOAS (1D)	300-466/379-493	Top Level Ceasar Site
DLR & USTC	Germany & China	2D MAXDOAS EnviMeS (2D)	296-460/440-583	Top Level Ceasar Site
IISER	India	mini-MAXDOAS Hoffmann UV (1D)	316-466	Ground Level Ceasar Site
INTA	Spain	2D-MAXDOAS RASAS III	325-445 or 400-550	Top Level Ceasar Site
IUP-Bremen	Germany	2 channel MAXDOAS (2D)	305-390/406-579	Top Level Ceasar Site
IUP-Bremen	Germany	Imaging DOAS	393-536	Top Level Ceasar Site
IUP Bremen	Germany	Measurement Truck (used static) incl. 2 channel MAXDOAS	286-419/413-524	-
IUP-Heidelberg	Germany	2D MAXDOAS EnviMeS	296-460/440-583	Top Level Ceasar Site
IUP-Heidelberg	Germany	Compact MAXDOAS (1D)	295-430/430-565	Ground Level Ceasar Site
KNMI	The Netherlands	mini-DOAS Hoffmann UV (1D)	290-443	Ground Level Ceasar Site
KNMI	The Netherlands	mini-DOAS Hoffmann VIS (1D)	400-600	Ground Level Ceasar Site

KNMI	The Netherlands	Pandora (2D)	290-530	Top Level Ceasar Site
LATMOS	France	SAOZ (ZS-DOAS)	270-640	Ground Level Ceasar Site
LATMOS	France	mini-SAOZ (ZS-DOAS)	270-820	Ground Level Ceasar Site
LuftBlick	Austria	Pandora-2S (2D)	280-540/400-900	Top Level Ceasar Site
MPIC	Germany	TubeMAXDOAS (1D)	316-474	Ground Level Ceasar Site
NIWA	New Zealand	EnviMeS 1D MAXDOAS	305-457/410-550	Ground Level Ceasar Site
NIWA	New Zealand	Lauder Acton275 MAXDOAS (1D)	290-363/400-460	Ground Level Ceasar Site
NASA-Goddard	USA	Pandora-1S (2D)	280-540	Top Level Ceasar Site
NUST	Pakistan	Mini MAXDOAS (1D)	320-465	Ground Level Ceasar Site
U.Munich	Germany	2D MAXDOAS EnviMeS	305-460/430-650	Top Level Ceasar Site
U.Toronto	Canada	PEARL-GBS instrument (2D)	300-550	Top Level Ceasar Site
Mobile DOAS systems				
BIRA-IASB	Belgium	Aeromobil	270-500	-
MPIC	Germany	Car-MAXDOAS	299-454	-
Uni Galati	Romania	Car-DOAS	280-550	-
Long Path DOAS				
IUP-Heidelberg	Germany	LP-DOAS	290-370/390-470 /600-680	3.8 km away
Cavity-Enhanced DOAS				
IUP-Heidelberg	Germany	CE-DOAS	-	Tower
In-situ analysers				
BIRA-IASB	Belgium	CAPS	450	Tower
ECN & RIVM	The Netherlands	NO_2 analysers	-	Tower (20,60,120,200m altitude)
KNMI	The Netherlands	In-situ O_3 monitor	-	Tower (20,60,120,200m altitude)

KNMI	The Netherlands	NO_2 sonde	-	starts at Tower
KNMI	The Netherlands	O_3 sonde	-	starts in De Bilt
KNMI	The Netherlands	Nephelometer	-	Tower (60m altitude)
TNO	The Netherlands	MAAP	-	Tower (60m altitude)
KNMI	The Netherlands	SMPS	-	Tower (60m altitude)
3.83.7 Sun-photometer, all-sky imager and aerosol Lidar systems				
KNMI	The Netherlands	Sun photometer	-	Tower
KNMI	The Netherlands	All-sky imager	-	Tower
KNMI	The Netherlands	Raman LIDAR CEALI	-	Ceasar Site
KNMI	The Netherlands	Ceilometer	-	Tower
RIVM	The Netherlands	mobile NO_2 LIDAR	-	Tower

Elevation	1°	2°	3°	4°	5°	6°	8°	15°	30°	90°	mean
R mean	0.908	0.993	0.924	0.993	0.940	0.996	0.995	0.986	0.979	0.987	0.970
R 15.09.16	0.979	0.999	0.968	0.999	0.974	0.998	0.999	0.999	1.000	0.993	0.991
R 16.09.16	0.983	0.994	0.983	0.996	0.977	0.995	0.995	0.968	0.883	0.914	0.969
R 17.09.16	0.752	0.995	0.720	0.990	0.812	0.993	0.993	0.999	0.851	0.987	0.909
R 18.09.16	0.964	0.991	0.988	0.993	0.977	0.993	0.987	0.995	0.997	0.998	0.988
R 19.09.16	0.867	0.981	0.927	0.988	0.953	0.995	0.998	0.995	0.990	0.994	0.969
R 20.09.16	0.733	0.998	0.757	0.999	0.816	0.998	0.999	0.991	0.999	0.996	0.929
R 21.09.16	0.960	0.997	0.952	0.995	0.960	0.998	0.999	0.989	0.997	0.975	0.982
R 22.09.16	0.926	0.990	0.943	0.991	0.974	0.999	1.000	1.000	0.997	0.997	0.982
R 23.09.16	0.896	0.999	0.954	0.995	0.919	0.998	0.965	0.999	1.000	0.997	0.972
R 24.09.16	0.868	0.984	0.959	0.987	0.973	0.997	1.000	0.999	0.997	0.999	0.976
R 25.09.16	0.941	0.993	0.924	0.998	0.962	0.999	0.998	0.950	0.999	0.997	0.976
R 26.09.16	0.926	0.999	0.966	0.996	0.963	0.998	1.000	0.968	1.000	0.997	0.981
R 27.09.16	0.929	0.989	0.949	0.991	0.977	0.993	0.999	0.988	0.998	0.998	0.981
R 28.09.16	0.982	0.994	0.947	0.986	0.929	0.997	0.999	0.966	0.999	0.975	0.977

Table A.2: Correlation coefficient (R) per elevation angle and day.

Elevation	1°	2°	3°	4°	5°	6°	8°	15°	30°	90°	mean
m mean	0.91	0.98	0.91	0.98	0.91	1.07	1.05	1.03	1.01	1.01	0.99
m 15.09.16	0.89	0.96	0.92	0.98	0.92	1.03	1.00	1.03	1.04	1.00	0.98
m 16.09.16	0.98	0.97	0.92	1.00	0.87	1.09	1.02	0.84	0.93	0.95	0.96
m 17.09.16	0.71	0.99	0.78	0.96	0.82	1.10	1.05	1.06	0.77	0.99	0.92
m 18.09.16	1.07	1.07	1.03	1.02	0.95	1.09	1.13	0.98	1.03	1.04	1.04
m 19.09.16	0.77	0.97	0.89	1.03	0.86	1.09	1.03	1.04	1.08	1.01	0.98
m 20.09.16	0.57	0.97	0.47	1.00	0.43	1.06	1.00	1.12	1.04	1.01	0.87
m 21.09.16	1.04	0.99	1.03	1.00	0.97	1.12	1.06	1.08	1.04	1.03	1.04
m 22.09.16	1.02	1.03	1.03	0.96	1.02	0.96	1.00	1.03	1.01	1.02	1.01
m 23.09.16	1.04	1.01	1.01	1.02	0.99	1.13	1.44	1.05	1.03	1.03	1.08
m 24.09.16	0.92	0.88	0.99	0.92	1.05	1.05	1.06	1.03	1.05	1.10	1.00
m 25.09.16	0.96	0.94	0.98	0.93	1.04	1.07	0.95	0.95	1.05	1.02	0.99
m 26.09.16	0.99	0.93	0.95	0.95	0.85	1.01	1.01	1.02	1.04	1.03	0.98
m 27.09.16	0.79	0.96	0.79	0.91	0.85	1.05	1.00	1.12	1.06	1.04	0.96
m 28.09.16	0.96	0.97	0.99	1.03	1.12	1.14	1.00	1.04	1.04	0.93	1.02

Table A.3: Slope (m) per elevation angle and day.

Elevation	1°	2°	3°	4°	5°	6°	8°	15°	30°	90°	mean
off mean	15.9	2.9	13.4	1.2	6.4	1.6	-1.1	1.3	2.2	1.0	4.5
off 15.09.16	8.6	1.8	9.2	0.6	8.2	0.7	3.4	1.3	0.9	0.3	3.5
off 16.09.16	-7.1	-5.9	-1.8	-8.3	-0.2	-8.5	-5.7	1.4	-0.4	-3.0	-3.9
off 17.09.16	32.4	-2.5	20.5	1.2	9.9	-5.0	-1.3	-1.8	3.1	-0.3	5.6
off 18.09.16	-1.3	-2.6	1.6	0.8	1.2	0.8	0.3	2.6	1.2	1.3	0.6
off 19.09.16	31.7	-0.6	12.2	-8.4	3.5	0.4	-0.8	-0.1	0.6	0.0	3.9
off 20.09.16	71.1	4.9	55.7	0.7	48.3	3.6	4.4	-2.9	1.7	1.0	18.8
off 21.09.16	-0.4	10.9	13.7	9.6	16.0	4.1	5.8	9.4	16.5	12.9	9.8
off 22.09.16	-7.2	-8.9	-6.3	3.0	-7.9	11.0	1.0	-0.4	1.1	-0.4	-1.5
off 23.09.16	16.8	-0.1	13.4	-2.1	-1.3	0.1	-27.8	-1.6	0.6	-0.9	-0.3
off 24.09.16	14.5	19.9	5.1	8.5	-5.3	3.6	1.0	0.7	1.4	1.1	5.1
off 25.09.16	4.3	4.3	2.7	3.2	-1.8	0.0	2.4	0.9	1.3	1.2	1.8
off 26.09.16	-0.8	7.3	16.3	-1.5	17.5	6.5	-1.4	4.3	-0.8	-1.7	4.6
off 27.09.16	52.7	8.0	41.2	12.7	17.7	7.2	2.6	1.5	3.3	2.2	14.9
off 28.09.16	7.1	4.0	4.1	-3.3	-15.5	-1.6	1.1	2.4	0.7	0.6	-0.1

Table A.4: Offset (*off*) $\cdot 10^{15}$ molec/cm^2 per elevation angle and day.

Elevation	1°	2°	3°	4°	5°	6°
Correlation coefficient	0.9600	0.9960	0.9590	0.9940	0.9590	0.9940
slope	0.9600	0.9800	0.9600	0.9800	0.9200	1.0800
offset	6.2000	0.8000	7.6000	0.5000	4.7000	0

Elevation	8°	15°	30°	90°		mean
Correlation coefficient	0.9900	0.9820	0.9740	0.9700		0.978
slope	1.0500	1.0700	1.0200	0.9600		1
offset	-1.0000	0.2000	2.2000	1.5000		2.3

Table A.5: Correlation coefficient, slope and offset ($\cdot 10^{15}$ molec/cm^2) per elevation angle.

B. Bibliography

[1] Vandeale et al. *NO2 absorption cross-section (298 K)*. 1998.

[2] Andor. *Andor Newton CCD*. Tech. rep. 2016.

[3] Andor. *Shamrock 303i*. Tech. rep. 2016.

[4] Austrotherm. *Austrotherm XPS - Extruderschaum*. URL: http://www.austrotherm.de/produkte/austrotherm-xps/ (visited on 12/01/2016).

[5] Bergische Universität Wuppertal. *FP 16 – Massenspektrometrie*. URL: http://www.atlas.uni-wuppertal.de/FP/anleitungen/fpI-16/fpI-16.html (visited on 08/08/2014).

[6] Geoffrey S. Brasseur, Guy P. and Orlando, John J. and Tyndall. *Atmospheric Chemistry and Global Change*. 1999. ISBN: 0195105214.

[7] J. D. E. Breynon and D.R. Lamb. *Charge-coupled devices and their applications*. London, 1980, p. 275. ISBN: 0070845220.

[8] CeramOptec. *Fiber specification*. Tech. rep. 2015.

[9] Wolfgang Demtröder. *Laserspektroskopie 1: Grundlagen*. 6th ed. Berlin, 2011, p. 300. ISBN: 3662442191. DOI: 10.1007/978-3-642-21306-9. URL: https://books.google.com/books?id=TW{_}YoQEACAAJ{\&}pgis=1.

[10] ENEO. *Manual for ENEO VPT-501*. Tech. rep. 2016.

[11] Freie Hansestadt Bremen - Der Senat für Umwelt Bau und Verkehr. *Indikator Luftqualität -Teilindikator 2: NO2*. URL: http://www.bauumwelt.bremen.de/detail.php?gsid=bremen213.c.9994.de (visited on 04/12/2017).

[12] Dr. John R. Gilchrist. "Choosing a Scientific CCD Detector for Spectroscopy". In: *Photonics Spectra* March (2002). URL: http://www.photonics.com/Article.aspx?AID=12010.

[13] WHO Working Group. "Health aspects of air pollution with particulate matter, ozone and nitrogen dioxide". In: *World Health Organization* January (2003).

[14] HEBO Spezialglas. *Color Filter Glass HEBO-Series*. URL: http://www.hebo-glass.com/hebo{_}series (visited on 11/16/2016).

[15] F. Hendrick et al. "CINDI-2 Planning Document". 2016.

[16] F. Hendrick et al. "CINDI-2: Semi-blind Intercomparison Protocol". 2016.

[17] IUP DOAS workgroup. *Education*. URL: http://www.iup.uni-bremen.de/doas/education.htm (visited on 03/06/2017).

[18] B.A. Callander J.T. Houghton, L.G. Meira Filho, J. Bruce, Hoesung Lee, N. Harris E. Haites, and K. Maskell. *Climate change 1994: radiative forcing of climate change and an evaluation of the IPCC IS92 emission scenarios*. 1995.

[19] Jeremy M. Lerner. "Imaging spectrometer fundamentals for researchers in the biosciences—A tutorial". In: *Cytometry Part A* (2006). URL: http://doi.wiley.com/10.1002/cyto.a.20242.

[20] All campaign participants. *Campaign Schedule and Logbook*. URL: https://docs.google.com/document/d/19nI1-PegVH8p57M-x-pcJyP8rI0zotMjqewuNxkajUg/edit (visited on 01/23/2017).

[21] Enno Peters. "Improved MAX-DOAS measurements and retrievals focused on the marine boundary layer". PhD thesis. University of Bremen, 2013.

[22] A J M Piters et al. "The Cabauw Intercomparison campaign for Nitrogen Dioxide measuring Instruments (CINDI): design , execution , and early results". In: *Atmospheric Measurement Techniques* 5 (2012), pp. 457–485. DOI: 10.5194/amt-5-457-2012.

[23] Ulrich Platt and Jochen Stutz. *Differential absorption spectroscopy*. Vol. 285. Physics of Earth and Space Environments. Berlin, Heidelberg: Springer Berlin Heidelberg, 2008. ISBN: 978-3-540-21193-8. DOI: 10.1007/978-3-540-75776-4.

[24] Andreas Richter. "Absorptionsspektroskopische Messungen stratosphärischer Spurengase über Bremen". PhD thesis. University of Bremen, 1997.

[25] Andreas Richter et al. "Increase in tropospheric nitrogen dioxide over China observed from space." In: *Nature* 437.7055 (2005), pp. 129–32. ISSN: 1476-4687. DOI: 10.1038/nature04092. URL: http://www.ncbi.nlm.nih.gov/pubmed/16136141.

[26] W Roedel and T Wagner. *Physik unserer Umwelt: Die Atmosphäre*. 1992. ISBN: 9783642157288.

[27] Anja Schoenhardt and Enno Peters. *Verbal discussion*. Bremen, 2016.

[28] a. Schönhardt et al. "A wide field-of-view imaging DOAS instrument for continuous trace gas mapping from aircraft". In: *Atmospheric Measurement Techniques Discussions* 7.4 (2014), pp. 3591–3644. ISSN: 1867-8610. DOI: 10.5194/amtd-7-3591-2014. URL: http://www.atmos-meas-tech-discuss.net/7/3591/2014/.

[29] Scientific Steering Comittee. *Cesar Observatory*. URL: http://www.cesar-observatory.nl/ (visited on 01/20/2017).

[30] Senatsverwaltung für Umwelt Verkehr und Klimaschutz. *Luftreinhalteplan Berlin 2011-2017; Die wichtigsten Ergebnisse Situationsanalyse*. URL: http://www.stadtentwicklung.berlin.de/umwelt/luftqualitaet/de/luftreinhalteplan/situation.shtml (visited on 04/12/2017).

[31] The Imaging Source. *Objective M0814-MP2*. Tech. rep. URL: https://s1.dl.theimagingsource.com/api/2.0/packages/publications/optics/m0814mp2/a9ded3e82d/m0814mp2{_}1.1.en{_}US.pdf.

[32] H. Wayne, R.P.; Biggs, P.; Burrows, J.P.; Canosa-Mas, C. E.; Hjorth, J.; Le Bras, G.; Moortgat, G. K.; Perner, D.; Poulet, G.; Restelli, G.; Sidebottom. "The Nitrate Redical: Physics, Chemistry and the Atmosphere". In: *Atmospheric Environment Part A, General Topics* 25.1 (1991), pp. 1–203.

[33] Wikipedia. *Sunlight*. URL: https://en.wikipedia.org/wiki/Sunlight (visited on 04/12/2017).